Doctoral Thesis

Investigation of nano-scale surface modification of Ni-rich cathode materials for lithium ion batteries

Hyejung Kim

Department of Energy Engineering

(Battery Science and Technology)

Graduate School of UNIST

2016

Investigation of nano-scale surface modification of Ni-rich cathode materials for lithium ion batteries

Hyejung Kim

Department of Energy Engineering
(Battery Science and Technology)

Graduate School of UNIST

Investigation of nano-scale surface modification of Ni-rich cathode materials for lithium ion batteries

A thesis/dissertation
submitted to the Graduate School of UNIST
in partial fulfillment of the
requirements for the degree of
Doctor of Philosophy

Hyejung Kim

1. 13. 2016 of submission

Approved by

조 재 필

Advisor
Jaephil Cho

Investigation of nano-scale surface modification of Ni-rich cathode materials for lithium ion batteries

Hyejung Kim

This certifies that the thesis/dissertation of Hyejung Kim is approved.

1. 13. 2016 of submission

signature

Advisor: Jaephil Cho

signature

Yoon Seok Jung

signature

Youngsik Kim

signature

Nam-Soon Choi

signature

Kuytae Lee

Abstract

Efforts have been devoted to the development of thermal stability and energy density in lithium ion batteries which have widely been applied as power sources for portable electronic devices, and electrical vehicles (EVs). Ni-rich systems (x > 0.6 mole in $LiNi_xCo_yMn_{1-x-y}O_2$) have been considered as promising candidates as a cathode material for such applications, due to its high specific capacity and low cost. However, it has thermal instability and poor cycle life. Arising safety problem such as thermal instability will be inevitable by high Ni-contents for high capacity and power because of the occurrence of cell explosion with exothermic reactions in charged batteries at elevated temperature. Much research has been carried out to improve such structural and thermal stability of Ni-rich cathode materials via surface coating (Al_2O_3, $AlPO_4$, ZnO etc.) and core-shell structure. Traditionally, research in the field has been reported that the coating can prevent their direct contact with the electrolyte solution, suppress the phase transitions, improve the structural stability, and decrease the disorder of cation in the crystal lattice. The surface structure of the electrode materials will play a more and more important role in their electrochemical performance due to directly influence electrical and physical character. Investigation of structural transformation at the surface of layered cathode materials in high temperature environment, such as Ni-rich system $Li_xNi_{1-y-z}Co_yMn_zO_2$ (that is, NCM), $LiNi_{0.8}Co_{0.15}Al_{0.05}O_2$ (that is, NCA) materials, have been accomplished by XAS (X-ray absorption spectroscopy), EELS(electron energy loss spectroscopy), atomic-scale STEM (Scanning transmission electron microscopy), *in-situ* TR-XRD (time resolved X-ray diffraction), during cycling. However, the lack of a thorough understanding of before and after surface treatment (coating or doping) still remains as an unsolved assignment. Structural degradation of Ni-rich cathode materials ($LiNi_xM_{1-x}O_2$; M = Mn, Co, and Al; $x > 0.5$) during cycling at both high voltage (>4.3 V) and high temperature (>50 ℃) led to the continuous generation of microcracks in a secondary particle which consisted of aggregated micrometer-sized primary particles. These microcracks caused deterioration of the electrochemical properties by disconnecting the electrical pathway between the primary particles and creating thermal instability owing to oxygen evolution during phase transformation. To develop the safety and electrochemical properties, I suggested a new treatment concept and coating material.

Firstly, We report a new concept to overcome those problems of the Ni-rich cathode material via nanoscale surface treatment of the primary particles. The resultant primary particles' surfaces had a higher cobalt content and a cation-mixing phase ($Fm\bar{3}m$) with nanoscale thickness in the $LiNi_{0.6}Co_{0.2}Mn_{0.2}O_2$ cathode, leading to mitigation of the microcracks by suppressing the structural change from a layered to rock-salt phase. Furthermore, the higher oxidation state of Mn^{4+} at the

surface minimized the oxygen evolution at high temperatures. This approach resulted in improved structural and thermal stability in the severe cycling-test environment at 60 ℃ between 3.0 and 4.45 V and at elevated temperatures, showing a rate capability that was comparable to that of the pristine sample.

Secondly, introducing a glue-role thin nano-filler layer consisting of a middle-temperature spinel-like $LiCoO_2$ phase between the grains, leads to significantly improved grain's adhesion ability in the aggregated particle compared to pristine particle that exhibits severe pulverization of the grains under the pressure and cycling. One of the most striking performances is that the cathode treated with the glue-layer exhibits highly stable cycling performance at 60℃ without using any electrolyte additives. Surprisingly, this performance is quite comparable to that at room temperature (89%). This unprecedented performances can be attributed to the increased binding energy between grain boundaries with the glue-layer.

Contents

List of Figures

Figure 2.3.3. a) Schematic diagram of a core-shell structure. b) Schematic view for the synthetic method of the heterostructures. c) SEM images of the particles corresponding to Figure 2.3.3a.

Figure 2.3.4. a) Rate capability of the pristine ($LiNi_{0.7}Co_{0.15}Mn_{0.15}O_2$), reference ($LiNi_{0.5}Co_{0.2}Mn_{0.3}O_2$), and core-shell materials (HS-$LiNi_{0.54}Co_{0.12}Mn_{0.34}O_2$) at different c-rates between 3.0 and 4.5V in coin-type half-cell. b) Capacity retentions of the three samples (pristine, reference, and core-shell hetero-structure materials) at 0.5C charge and discharge rate. c) Voltage profiles of the three samples (pristine, reference, and core-shell hetero-structure materials) for the discharge process at 1st, 20th, and 40th cycles at 60 ^{o}C. d) DSC profiles of the pristine ($LiNi_{0.7}Co_{0.15}Mn_{0.15}O_2$), reference ($LiNi_{0.5}Co_{0.2}Mn_{0.3}O_2$), and core-shell materials (HS-$LiNi_{0.54}Co_{0.12}Mn_{0.34}O_2$) after charging up to 4.5 V.

Figure 3.1.1. (a) Schematic diagram of the surface treatment on the primary particles. (b) Cross-sectional SEM image of the synthesized ST-NCM cathode material. (c) STEM image of the primary particle in the region indicated by a red rectangle in (b). (d) EDXS profile of the ST-NCM surface corresponding to the yellow arrow in (c).

Figure 3.1.2. SEM images of the (a) NCM, (b) Al_2O_3-coated NCM, and (c) ST-NCM samples after surface modifications.

Figure 3.1.3. EDXS data of ST-NCM at the six different point to clarify the EDXS profile of Figure 1d.

Figure 3.1.4. HR-TEM images of the inner primary particles (grains) for the (a) NCM and (b) ST-NCM particles. EDX profiles from outer side to inner side on the surface of the primary particle for the (c) NCM and (d) ST-NCM particles.

Figure 3.1.5. HADDF-STEM image of (a) $LiNi_{0.6}Co_{0.2}Mn_{0.2}O_2$ (NCM) on the surface of a primary particle (grain). Magnified STEM image of the NCM in (b) Region 1 and (c) Region 2 in (a). HAADF STEM image of (d) surface-treated $LiNi_{0.6}Co_{0.2}Mn_{0.2}O_2$ (ST-NCM) on the surface of the primary particle (grain). Magnified STEM image of the ST-NCM in (e) Region 1 and (f) Region 2 in (d). The insets of STEM images show digitalized fast-Fourier-transformed (FFT) patterns. EELS spectra obtained on the surface of a primary particle in Regions 1 and 2 of (g) NCM and (h) ST-NCM.

Figure 3.1.6. XRD patterns with Rietveld refinement plot for the (a) NCM and (b) ST-NCM samples.

Figure 3.1.7. Structure of the NCM and ST-NCM samples for the primary particle. (a) General layered structure of NCM, (b) Mixed structure of ST-NCM with layered and CM layer. The oxidation state of transition metals indicated for each material.

Figure 3.1.8. (a) First charge–discharge profiles of the NCM and ST-NCM samples at 0.1 C rate between 3.0 and 4.45 V at 25 ℃. (b) Cycle performance of the NCM and ST-NCM samples between 3.0 and 4.45 V at 60 ℃ (charge rate: 0.5 C; discharge rate: 1 C, Q = discharge capacity). (c) Charge and discharge voltage profiles of the NCM and ST-NCM samples after the 10th, 20th, 50th, 100th, and 150th cycles at 60 ℃ (each cycle matched with black, red, blue, green, and pink color lines, respectively). (d) Differential curves of the NCM and ST-NCM samples corresponding to (c). (e) Rate capabilities of

NCM and ST-NCM evaluated between 3.0 and 4.45 V at 25 ℃. (Q = discharge capacity)

Figure 3.1.9. (a) Rate capability at RT 25ºC, (b) voltage profile at initial cycle between 3.0 – 4.45 V at 60ºC, (c) cycle performance between 3.0 – 4.45 V at 60ºC for the NCM, Al_2O_3-coated NCM, and ST-NCM samples.

Figure 3.1.10. Particle morphology and fine structure of primary particles after 150 cycles between 3.0 and 4.45 V at 60 ℃. Cross-sectional FIB-SEM images of the (a) NCM and (b) ST-NCM particles. HAADF-STEM images of (c) NCM and (d) ST-NCM particles. Magnified STEM images of (e) NCM and (f) ST-NCM particles in the regions indicated by the yellow frames in (c) and (d), respectively. High-magnification STEM images of (g) NCM and (h) ST-NCM particles in (e) and (f), respectively. The insets of (g) and (h) show the FFT patterns.

Figure 3.1.11. Cross-sectional FIB-SEM images of the NCM and ST-NCM particles before and after cycles at 60 ºC, cross-sectional SEM images of pristine particle of (a) NCM, (b) Al_2O_3-coated NCM and (c) ST-NCM, cross-sectional SEM images of (d) NCM, (e) Al_2O_3-coated NCM and (f) ST-NCM after 150 cycles between 3.0 and 4.45 V at 60 ºC.

Figure 3.1.12. STEM images of NCM sample for the each primary particles after 150cycles.

Figure 3.1.13. DSC profiles of NCM and ST-NCM after charging to 4.5 V.

Figure 3.1.14. Normalized TM K-edge XANES spectra of the (a) Mn K-edge, (b) Ni K-edge, and (c) Co K-edge of NCM and ST-NCM as functions of heating temperature.

Figure 3.1.5. HADDF-STEM image of (a) $LiNi_{0.6}Co_{0.2}Mn_{0.2}O_2$ (NCM) on the surface of a primary particle (grain). Magnified STEM image of the NCM in (b) Region 1 and (c) Region 2 in (a). HAADF STEM image of (d) surface-treated $LiNi_{0.6}Co_{0.2}Mn_{0.2}O_2$ (ST-NCM) on the surface of the primary particle (grain). Magnified STEM image of the ST-NCM in (e) Region 1 and (f) Region 2 in (d). The insets of STEM images show digitalized fast-Fourier-transformed (FFT) patterns. EELS spectra obtained on the surface of a primary particle in Regions 1 and 2 of (g) NCM and (h) ST-NCM.

Figure 3.2.1. Schematic diagram of glue-layer fabrication mechanism. The scheme shows a formation of glue layer (purple) in a NCA secondary particle (gray) during the coating processes. The cross-sectional SEM images of the pristine sample show a severe morphological degradation during the electrochemical distinct from that of G-layer sample. The key roles of the glue layer on the electrochemical performance of the materials will be discussed in detail.

Figure 3.2.2. SEM images for surface morphology of (a, c) Pristine and (b, d) G-layer samples, Cross-sectional images of (e) Pristine and (f) G-layer samples

Figure 3.2.3. Photographs and SEM images of pristine and G-layer powders after pellet density test. STEM images of grains of (**a**) Pristine and (**d**) G-layer samples. Fast fourier transform (FFT) image of inserted in (a) and (d), respectively. The HR-TEM images between grains (**b, c**) Pristine ((**c**) Expanded image of red rectangle in (b)) and (**e, f**) G-layer samples ((**f**) Expanded image of red rectangle in (e)).

The pellets were collected after pressing with the pressure of 25 MPa (=254.93 kgf cm^{-2}) for 30 sec. Top view SEM images; (**g**) Pristine sample (**h**) G-layer sample. The pellets of the powder were shown in the insert of (**g and h**), respectively.

Figure 3.2.4. STEM images and EDS mapping results of (a) pristine and (b) G-layer samples

Figure 3.2.5. STEM images for grain boundaries of (a, b) Pristine and (c, d) G-layer samples

Figure 3.2.6. Electrochemical evaluation at high temperature and STEM/EDXS images after 300 cycles of the samples. (**a**) Cycle performance of the pristine and G-layer samples between 3.0 and 4.3 V at 25, 60 ℃ (charge rate: 0.5 C; discharge rate: 1 C). The voltage profiles are available in supplementary figure 4. (**b**) Voltage versus cycle number in cycling at high temperature for pristine and G-layer samples. (**c**) Voltage profile of discharge for storage test at high temperature. The cells are stored at 60 ºC for 14 weeks after 4.3V charge (Q=Discharge capacity). STEM images of the cross-sectioned particle; (**d**) Pristine sample before and after cycle. (**e**) G-layer sample before and after cycle.

Figure 3.2.7. Voltage profiles of (a) Initial charge and discharge for the Pristine and G-layer sample, (b) Cycling at high temperature (60ºC) between 3.0-4.3V, and (c) Cycling at room temperature (25ºC) between 3.0-4.3V

Figure 3.2.8. Voltage profiles of (a) Initial charge and discharge for the $LiNi_{0.8}Co_{0.1}Mn_{0.1}O_2$ (NCM811) and G-layer NCM811 sample, (b) Cycle retention at high temperature (60ºC) between 3.0-4.3V for the NCM811 and G-layer NCM811 samples.

Figure 3.2.9. Cross-sectional SEM images of secondary particles of pristine and G-layer samples. The particle before cycle; (a) Pristine and (b) G-layer samples. The particle after cycle; (c, e, g) Pristine and (d, f, h) G-layer samples.

Figure 3.2.10. STEM-EDXS images between grain boundaries of (a) pristine and (b) G-layer samples after 300 cycle at 60 ºC.

Figure 3.2.11. Rate performance results and GS-EIS analysis data. (**a**) Rate capabilities of Pristine and G-layer evaluated between 3.0 and 4.3 V at 25 ℃. (**b**) Voltage profiles of the first cycles at each C rates during the rate performance test of (a). Galvanostatic-Electrochemical Impedance Spectroscopy (GS-EIS) in discharge at 1C rate; (**c**) Voltage profile of Pristine and G-layer samples. (**d**) Nyquist plots of Pristine and G-layer samples at different DOD of 10%, 20%, 40%, 50%, 80%, and 90% on the chronopotentiometric profiles are measured simultaneously in (c). The EIS spectra consist of high-frequency semi-circles, intermediate-frequency semi-circles, and low-frequency inclined lines. The resistances were characterized by the different frequency semi-circles and inclined lines: (i) solution resistance (R_s) and solid electrolyte interface (SEI) layer resistance (R_{SEI}) by high-frequency semi-circle, (ii) charge transfer resistance (R_{CT}) by intermediate-frequency semi-circle, (iii) Warburg impedance (Z_W)

by low-frequency sloped diffusion tail.

Figure 3.2.12. Results of molecular dynamics (MD) simulation. (a) Interfacial energy gradient depend on distance between NCA particles with radius of 25Å and 50Å with different terminations. (i.e. Li termination and Oxygen termination) (b) The average binding energy of unit area (J/m^2) between surfaces classified depending on the surface polarity. (i.e. polar surfaces : NCA(001), NCA(101), MT-LCO(113), and MT-LCO(111), nonpolar surfaces : NCA(104), NCA(110), MT-LCO(001), and MT-LCO(101). Blue bar indicates the binding energy between NCA and MT-LCO surfaces. Grey bar indicates the binding energy between NCA and NCA surfaces. (c) Schematic illustration of interfacial binding energies of void and glue-layer. (d) Left : Interface of O-terminated NCA(001) with O-terminated MT-LCO(113); Middle : NCA(104) with MT-LCO(001); Right : O-terminated NCA(001) with O-terminated NCA(001). Interfacial region is expressed with orange color and infiltrated Ni, Al, and Co atoms from NCA were expressed with cyan dashed-circle.

Figure 3.2.13. Scheme of interface modeling. (a) Near Coincidence Site Lattice (NCSL) theory. Two rectangular surface lattices (solid black lines and red dotted lines) are shown with lattice parameters (i.e. a1, b1, a2, and b2) and supercell size parameters (A1, B1, A2 and B2). (b) Representative interface model system composed of two surface slabs. (c) and (d) Top view and side view of each rectangular unit cell of NCA and MT-LCO surfaces, respectively. Dotted-lines represent termination type of each surface. Li, Ni, Co and O atom are bright purple, navy, blue, red color respectively. Al and Co dopants are not shown in NCA surface because Ni atoms are randomly replaced by dopants after building interface.

Figure 3.2.14. The binding energy of unit area (J/m2) of each (a) NCA/MT-LCO and (b) NCA/NCA interface. NCA surface slab was described with termination. (c) Non-polar NCA/MT-LCO. Red bar indicates combination of low planar density slabs, purple bar indicates combination of high planar density slab and low planar density slab, and blue bar indicates combination of high planar density slabs.

Figure 3.2.15. Final configuration of each NCA/MT-LCO interface formed with NCA(001) and NCA(104) with planar coincidence densities (i.e. Σ_N and Σ_M for NCA and MT-LCO) and binding energies (J/m^2). Li, Ni, Co, Al and O atom are bright purple, navy, blue, pink, and red color respectively.

Figure 3.2.16. Final configuration of each NCA/MT-LCO interface formed with NCA(101) and NCA(110) with planar coincidence densities (i.e. Σ_N and Σ_M for NCA and MT-LCO) and binding energies (J/m^2). Li, Ni, Co, Al and O atom are bright purple, navy, blue, pink, and red color respectively.

Figure 3.2.17. Final configuration of each NCA/NCA interface formed with NCA(001) and NCA(104) with planar coincidence densities (i.e. Σ_T and Σ_P for NCA on top and bottom) and binding energies (J/m^2). Li, Ni, Co, Al and O atom are bright purple, navy, blue, pink, and red color respectively.

Figure 3.2.18. Final configuration of each NCA/NCA interface formed with NCA(101) and NCA(110) with planar coincidence densities (i.e. Σ_T and Σ_P for NCA on top and bottom) and binding energies (J/m^2). Li, Ni, Co, Al and O atom are bright purple, navy, blue, pink, and red color respectively.

List of Tables

Ⅰ. Introduction

To reduce carbon emissions and the dependence on fossil fuel, the development of energy storage systems for renewable energy sources has been widely investigated. Figure 1 shows the schema of energy densities for various rechargeable batteries. Lithium-ion batteries (LIB) have been most commonly used in various electronics for energy storage. They are one of the most popular types of rechargeable batteries for portable electronics because of their a high energy density, a small memory effect, and only a slow loss of charge when not in use. The LIB is generally composed of a cathode, anode, separator, and electrolytes. The electrical energy is stored and used in the Li-ion batteries via energy conversion between electrochemical energy and chemical energy. Lithium ion batteries operate by lithium ion transportation and utilizes the oxidation and reduction reaction at the cathode and anode. In the charging process, the lithium ions move from cathode material to anode material with energy conversion from electrochemical energy to chemical energy, and the electrical energy is stored in the battery. The reverse process occurs during discharge. Since the amounts of lithium ion included in the cathode material decide the capacity of the battery, the cathode material is the most important part among the components of the LIB system, such as electrode material, separator, electrolytes and so on. Therefore, standard properties, such as capacity, energy density, power density and safety, depend on the cathode materials. Even the cost portion of the cathode is the largest in the cell.

The LIB was commercialized by SONY in 1991 with $LiCoO_2$ (known as LCO) as cathode materials. Now, lithium ion batteries have been applied to portable electronic devices such as note PCs, mobiles, and tablet PCs. Since 1997, Electric vehicles have been getting attentions worldwide due to the suppressing of emission of greenhouse gases and decreasing of prices of crude oils. The electric vehicles are classified by their power source such as Electric Vehicle (EV, run on a rechargeable electric battery), Hybrid Electric Vehicle (HEV, electric motor assists gasoline motor), and Plug-in Hybrid Electric Vehicle (PHEV, similar to hybrids but with rechargeable electric batteries). Currently, the LCO materials with a working voltage of 3.7V are used as commercial cathode materials which are obtained by simple methods, because of its good cycle retention with a stable layered structure of $R\bar{3}m$ for lithiation/delithiation. However, the LCO cathode material has some problems for larger scale batteries such as EV: ⅰ) the limited supply and high cost of Cobalt. ⅱ) the low reversible capacity of 150 mAh g^{-1}. These problems hinder the development of electric vehicles, and therefore alternate materials are required.

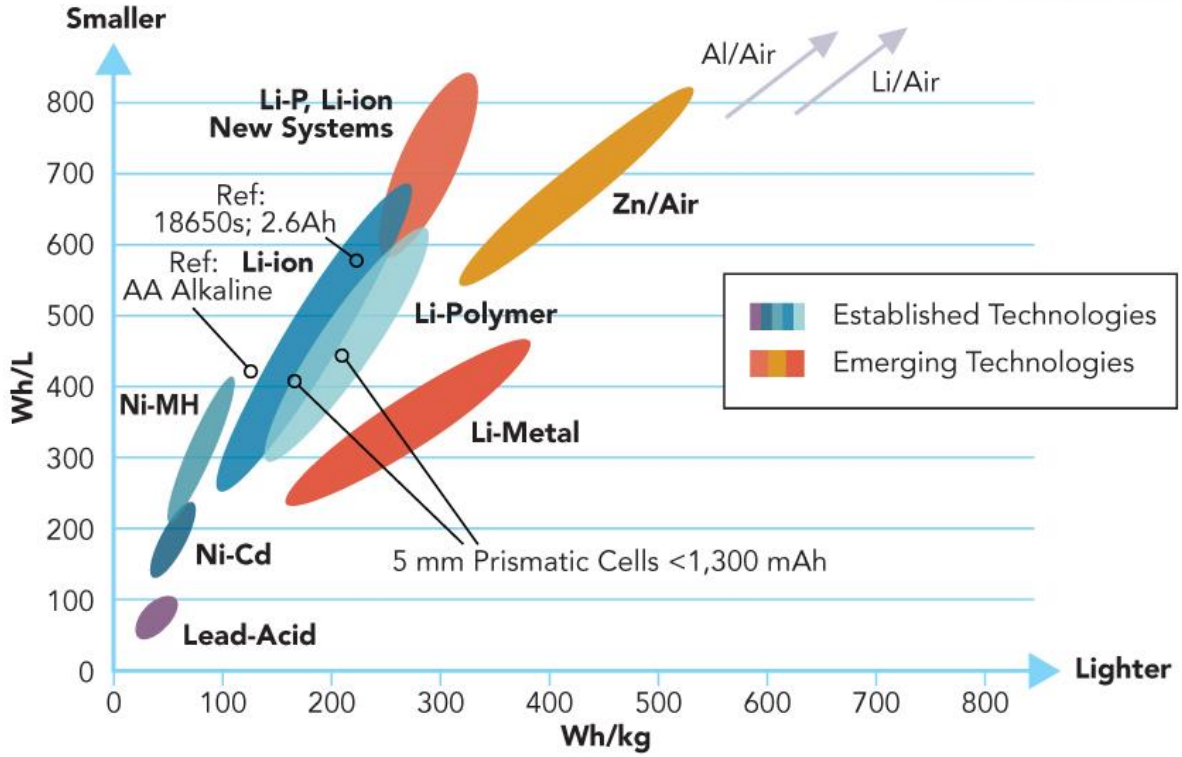

Figure 1. Comparison of energy densities in terms of volumetric and gravimetric for various rechargeable batteries. (Copyright of http://www.designnews.com/document)

Ⅱ. Theoretical & Literature Survey

2.1 Ni-rich layered cathode materials for lithium ion batteries

The layered structure of $LiMO_2$ (M=transition metals; Co, Ni, Mn, Fe, etc.) is an iso-structure with α-$NaFeO_2$ (space group of $R\bar{3}m$) and has a highly close-packed structure with oxygen ions in cubic arrangement. The lithium ions and transition metal occupy the octahedral sites of alternating layers and this structure is called an "O3-type" structure. Figure 2.1.1 shows the crystal structure of the three lithium-insertion compounds with different Li+ ions pathway dimension types.[3] Li ions transport through 2D diffusion pathway between MO_2 layers, and therefore the layered structure shows higher ionic conductivity compared to other structures such as the three-dimensional spinel structure (LiM_2O_4) and the one-dimensional olivine structure ($LiMPO_4$). $LiCoO_2$ is a typical layered structural cathode material with rhombohedral symmetry and has been adopted as a commercial cathode material until now. However, $LiCoO_2$ is no longer an appealing material for large-scale energy storage systems, due to its low reversible capacity and structural transition in spite of high theoretical capacity of 270 mAh g^{-1}.

The lithium nickel oxide ($LiNiO_2$) materials were attractive as cathode material with higher theoretical capacity and lower cost than $LiCoO_2$. it also has a broad oxidation/reduction reaction region with the Ni^{2+}/Ni^{4+} redox process, despite having a similar voltage window as $LiCoO_2$ cathode materials. However, synthesis of ideal $LiNiO_2$ composition is difficult to prepare by general solid-state methods. Usually, nonstoichiometric $Li_{1-x}Ni_{1+x}O_2$ ($0.6 < x < 1.0$) cathodes were obtained because the Ni^{2+} ion is more stable than Ni^{3+} ion. Furthermore, the similar ionic radius of Ni^{2+} (0.69 Å) with Li^+ ions (0.76 Å) lead to cationic disorder in the crystal lattice, as shown in Figure 2.1.3. To obtain stable layered structure of $LiNiO_2$ without cationic disorder, various elements are partially substituted to nickel sites such as $LiNi_{1-x}Mn_xO_2$, $LiNi_{1-x}Co_xO_2$, $LiNi_{1/3}Co_{1/3}Mn_{1/3}O_2$, $LiNi_xCo_yMn_{1-x-y}O_2$, and $LiNi_xCo_yAl_{1-x-y}O_2$. The electrochemical and physical properties of Ni-base cathode materials depend on the ratio of elements in the mixed compositions (Figure 2.1.4). The higher content of cobalt in Li-Ni-Co-Mn-O composition is responsible for higher structural stability, and Al shows similar properties. Increasing Mn content in the layered Li-Ni-Co-Mn-O composition leads to higher thermal stability.

Ohzuku et al.[4] reported the cobalt substitution in $LiNiO_2$ cathode material, and investigated the change of the lattice dimensions and electrochemical activity. The substitution of cobalt ions in $LiNiO_2$ gives rise to smaller unit cell dimensions of *a* and *c* in a hexagonal setting. In $LiNiO_2$, the Ni ions coexist to Ni^{2+} and Ni^{3+} ions with ionic size of 0.69 Å and 0.63 Å, respectively. When cobalt ion in an oxidation state of 3+ is substituted, the Ni^{3+} ions are dominant compared to Ni^{2+}. That is why the lattice dimensions are decreased. Diminishing the cation-disordering by cobalt

substitution secures the lithium pathway in a layered structure and improves the conductivity of the compounds.[5] In this regards, the electrochemical performances are improved by Co substitutions. In these $LiNi_{1-x}Co_xO_2$ compounds, the working voltage is increased with an increasing x ratio because the higher redox voltage of cobalt ion than that of nickel ion for $MO_2/LiMO_2$ in $LiMO_2$, and the middle composition with x = 0.5 is the optimum combination to accompany a high working voltage and stable cycle life.

Nickel and manganese based layered-cathode materials such as $LiNi_{0.5}Mn_{0.5}O_2$ and $LiNi_{0.33}Co_{0.33}Mn_{0.33}O_2$ have been studied because their electrochemical properties are comparable to $LiCoO_2$. However, when comparing the materials, $LiNi_{0.33}Co_{0.33}Mn_{0.33}O_2$ cathode material shows a higher thermal stability and rate capability with equal amounts of the transition metals of Ni, Co, and Mn.[6] The $LiNi_{0.33}Co_{0.33}Mn_{0.33}O_2$ shows a high reversible capacity of about 200 mAh g^{-1} (between 2.5 and 4.6V) and a good rate capability. In this respect, the $LiNi_{0.33}Co_{0.33}Mn_{0.33}O_2$ is considered to be one of the most promising alternative materials for $LiCoO_2$.

Those $LiNi_xCo_yTM_{1-x-y}O_2$ (TM = Mn or Al) cathode materials are usually synthesized by the solid-state reaction of a mixture of $M(OH)_2$ (M=Ni, Co, Mn) precursor and lithium hydroxide at a high temperature (600 − 1000 ℃). The $M(OH)_2$ (M=Ni, Co, Mn) precursor powders are obtained via a co-precipitation method to gain a uniform and homogeneous powder precursor of triple complex hydroxide.[7] The synthetic method can produce a uniform distribution of spherical powders with higher tap-density than non-spherical particles. The spherical particle is a secondary particle composed of an agglomeration of primary particles. The morphology and size of particles are controlled by several co-precipitation conditions such as pH, temperature, the amount of chelating agent, reaction time, etc. To obtain a higher reversible capacity, the Ni-content is increased in the $LiNi_xCo_yTM_{1-x-y}O_2$ (TM = Mn or Al, $x>0.6$, $y\geq0.1$). However, increasing the Ni content with a higher capacity in the composite is accompanied by poor thermal, structural and electrochemical stability. Therefore, some treatments for Ni-rich components are required for high energy density to accompany safety and electrochemical stability.

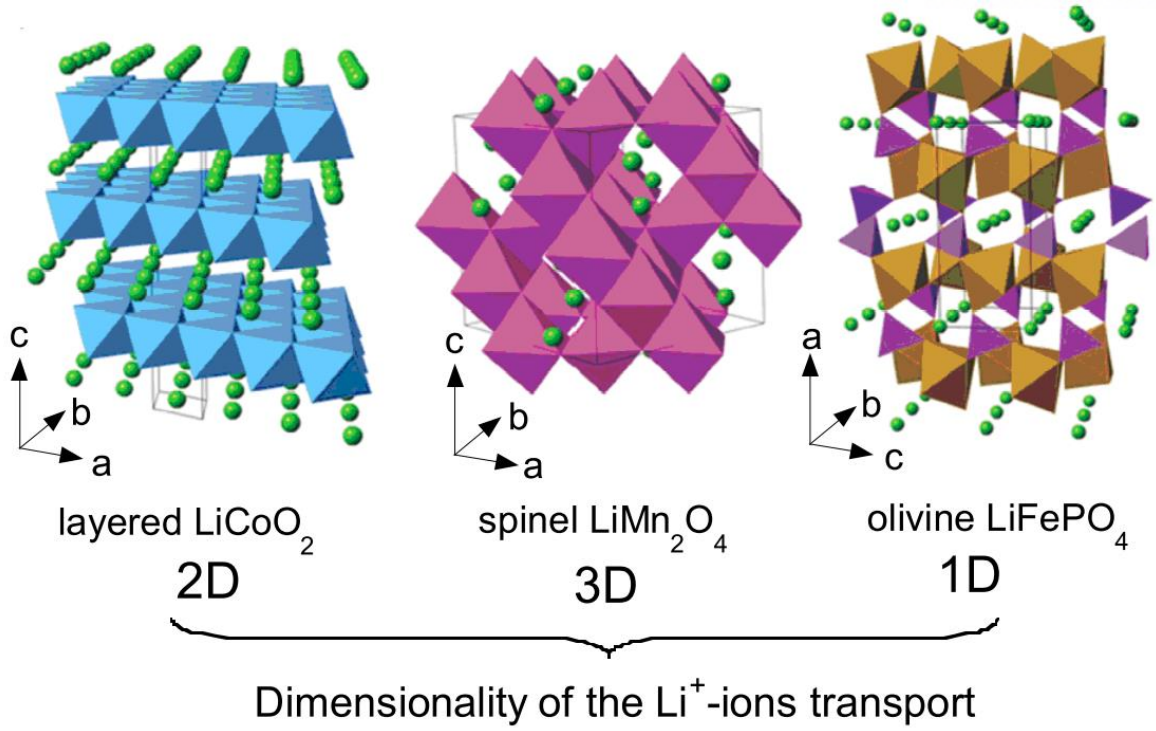

Figure 2.1.1. Crystal structure of the three lithium-insertion compounds in which the Li+ ions are mobile through the 2-D (layered), 3-D (spinel) and 1-D (olivine) frameworks.[3]

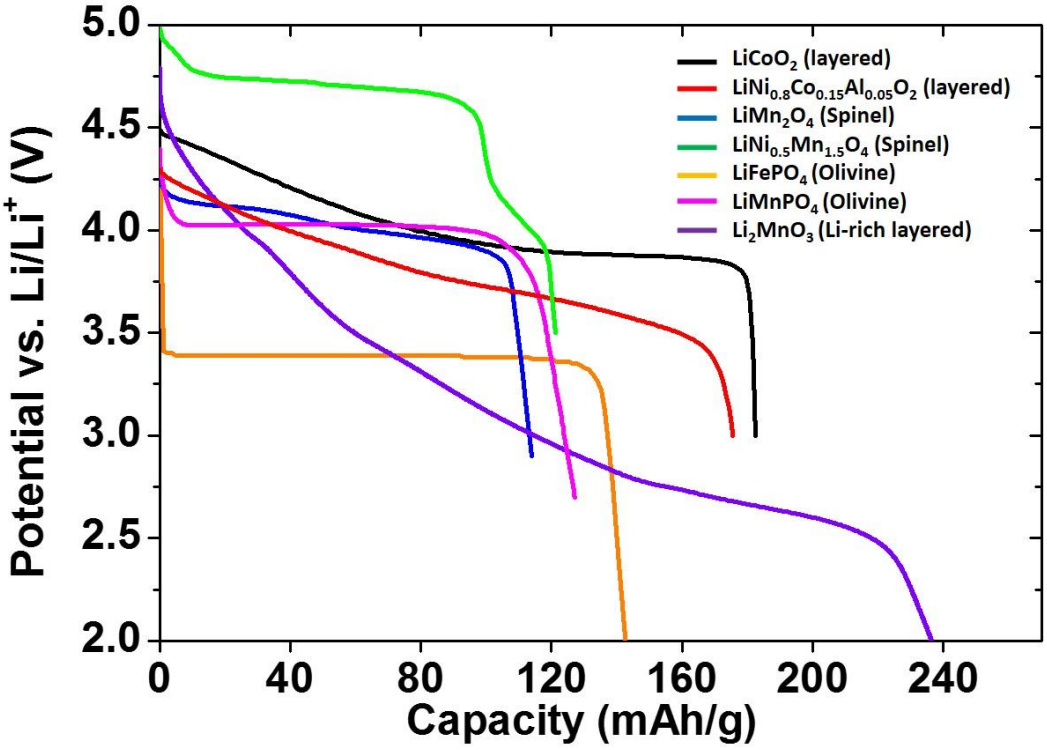

Figure 2.1.2. Voltage profile of cathode materials with layered, spinel, and olivine structure.

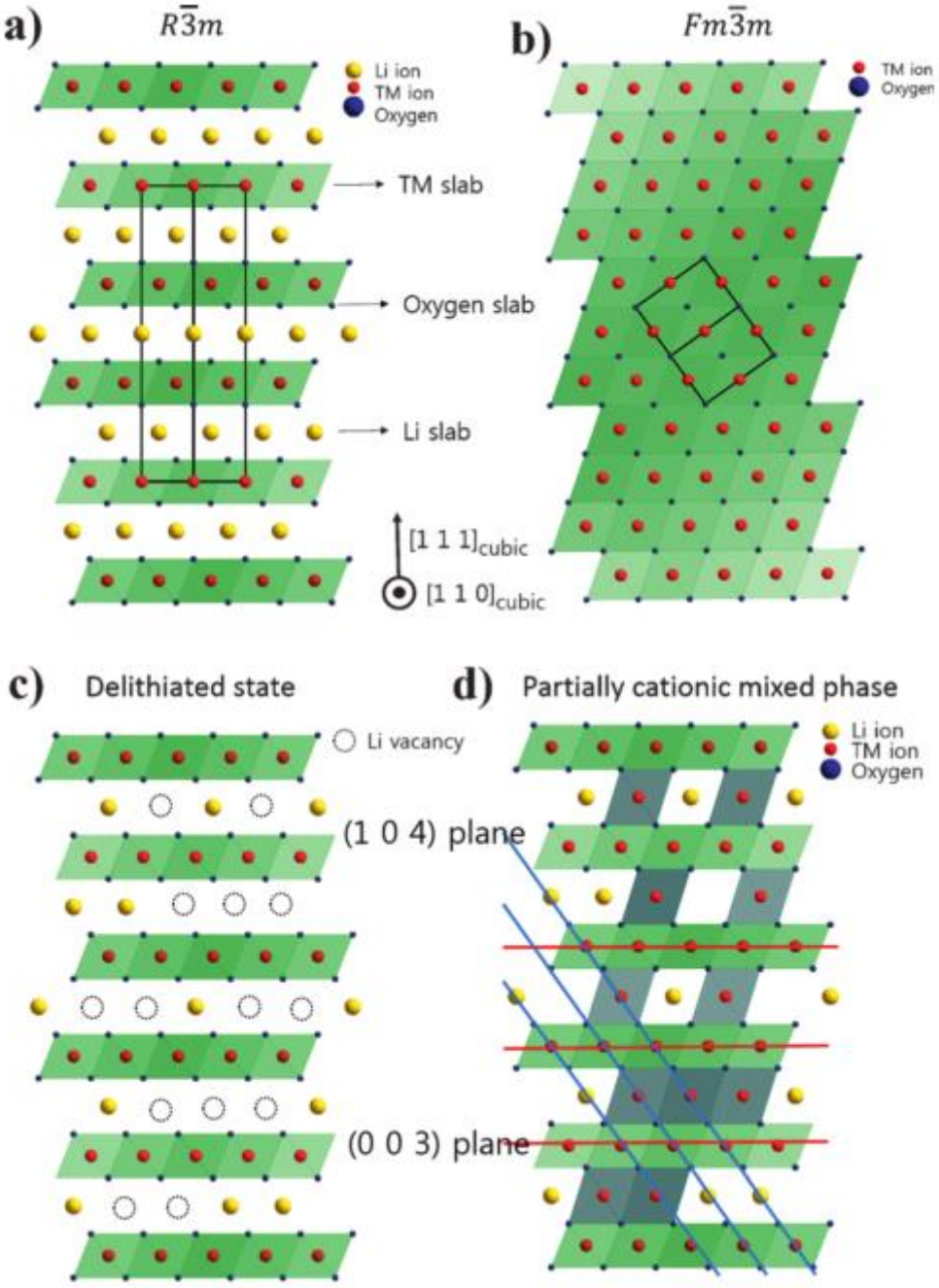

Figure 2.1.3. Illustration of the ordered and disordered phase in layered lithium metal oxides and their structural transformation. a) Well-ordered R3¯m structure; b) The cation disorder or cation mixing phase with Fm3¯m structure c) R3¯m structure; with Li vacancies in highly charged state; d) Partially cation mixed phase with TM ions in Li slab. Li atoms yellow, transition metals red, coordinated oxygen atoms dark blue.[8]

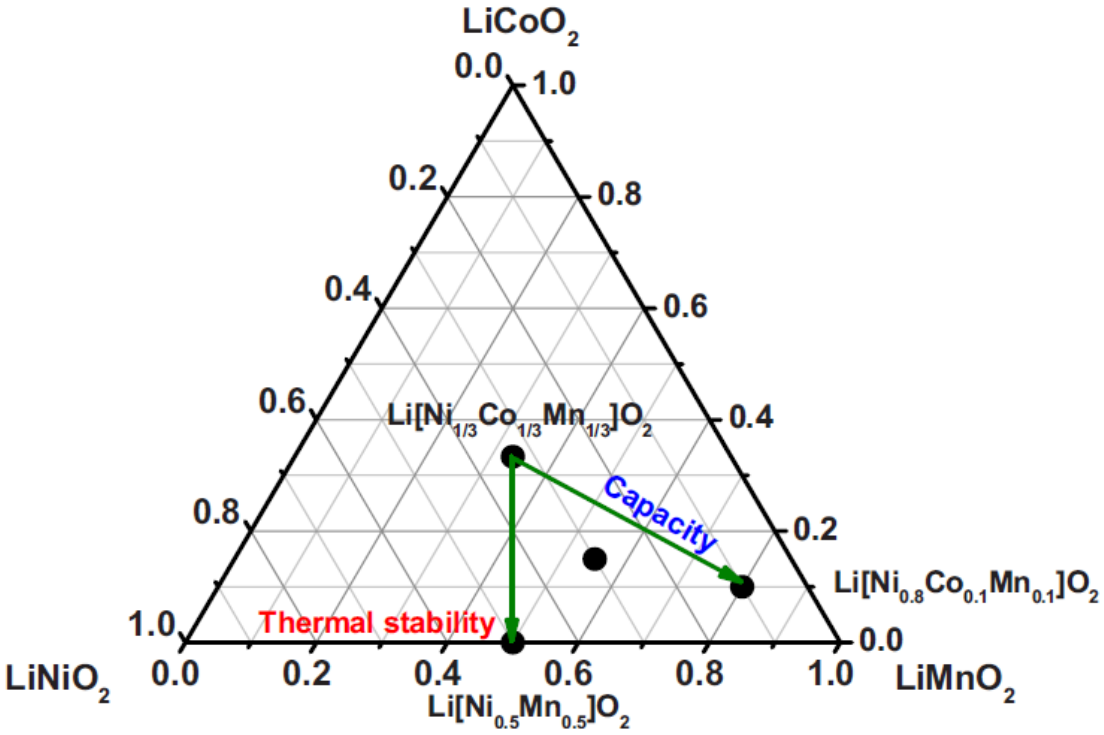

Figure 2.1.4. Phase diagram of ternary $LiCoO_2$–$LiNiO_2$–$LiMnO_2$. Note that $LiNi_{0.55}Co_{0.15}Mn_{0.30}O_2$ lies at the center of $LiNi_{1/3}Mn_{1/3}Co_{1/3}O_2$, $LiNi_{0.8}Mn_{0.1}Co_{0.1}O_2$, and $LiNi_{1/2}Mn_{1/2}O_2$, so that it represents a compromise between high capacity and thermal stability.[1]

2.2 Degradation mechanism of Ni-rich cathode materials

To improve their intrinsic properties, it is necessary to understand the degradation mechanism of the Ni-rich layered cathode materials in cycling. In the lithiation/delithiation process, the cathode materials undergo several degradation reactions such as structural transformation, surface reaction with electrolyte, decomposition reaction with oxygen release, etc. Those degradation reactions lead to characteristic breakdowns in electrochemical and thermal properties. To comprehend those reaction mechanisms deeply, many researchers have investigated the three degradation reactions: 1) structural degradation; 2) surface degradation; and 3) morphological degradation.

Firstly, the layered structure shows a space group of $R\bar{3}m$ with lattice parameters of a = 2.862 Å and c = 14.227 Å in a hexagonal setting. Also, the structure is composed of a regular O-Li-O-M-O-Li-O-M-O arrangement along the (111) plane of rock-salt structure. For the layered structure, the lithium ions occupy an octahedron site when the MO_2 layers are repeated three times in the unit cell. Those arrangement are known as "O3-structure", by the combination of O, symbolizing the octahedron occupied lithium ions; and 3, symbolizing the number of repetition. In the initial delithiation process of the layered structure, the lattice is expanded along the *c*-axis by repulsion between the oxygen atoms of the MO_2 layers. And the lattice is contracted along the *c*-axis after full delithiation by vacant lithium slabs. In this respect, the layered structure shows diverse structural transformations depending on the lithium contents in the $LiMO_2$ cathode materials as shown Figure 2.2.1.

In Li_xCoO_2, the O3-structure changes to P3 structure when x<0.5. On the other hand, $Li_xNi_yCo_zTM_{1-y-z}O_2$ (TM = Mn or Al) cathode materials maintained the O3-structure despite x<0.2, and therefore the materials can maintain electrochemical properties at high charge voltage. However, the ternary systems of $Li_xNi_yCo_zTM_{1-y-z}O_2$ (TM = Mn or Al) show different structural changes according to the ratio of transition metals. For example, Nam et al. investigated the microscopic structural origin of the thermal instability for the $Li_xNi_{0.8}Co_{0.15}Al_{0.05}O_2$ and $Li_xNi_{1/3}Co_{1/3}Mn_{1/3}O_2$ at an overcharged state by combining in-situ synchrotron X-ray diffraction and absorption techniques with transmission electron microscopy.[2] They studied the systematically structural changes of $LiNi_{0.8}Co_{0.15}Al_{0.05}O_2$ and $LiNi_{1/3}Co_{1/3}Mn_{1/3}O_2$ cathode materials at overcharged states during heating by using in-situ synchrotron-based time-resolved X-ray diffraction (TR-XRD) and mass spectroscopy (MS), X-ray absorption spectroscopy (XAS), and in situ transmission electron microscopy (TEM). Thermal instability of the cathode materials is an important safety issue in lithium ion batteries. The thermal instability is related to structural change with oxygen release. That is why an understanding of the structural origin is needed to improve the thermal stability. Generally, Ni-based layered cathode bears on several structural transitions,

including $R\bar{3}m$ (layered) → $Fd\bar{3}m$ (spinel) → $Fm\bar{3}m$ (rock-salt). Figure 2.2.2 shows time-resolved XRD (TR-XRD) patterns of the overcharged $Li_{0.33}Ni_{0.8}Co_{0.15}Al_{0.05}O_2$ and $Li_{0.33}Ni_{1/3}Co_{1/3}Mn_{1/3}O_2$ during heating up to 600℃.The structural change of overcharged $Li_{0.33}Ni_{0.8}Co_{0.15}Al_{0.05}O_2$ from a rhombohedral ($R\bar{3}m$) to a disordered spinel ($Fd\bar{3}m$) phase starts at about 212 ℃, and is completed at about 256 ℃, as shown in Figure 2.2.2. After that, the spinel structure ($Fd\bar{3}m$) gradually changes to a rock-salt structure ($Fm\bar{3}m$) with increasing temperature, and finishes at around 471 ℃. On the contrary, the $Li_{0.33}Ni_{1/3}Co_{1/3}Mn_{1/3}O_2$ shows considerably different phase transition to that of the $Li_{0.33}Ni_{0.8}Co_{0.15}Al_{0.05}O_2$ sample. The rhombohedral phase of the layered structure starts to change to a spinel phase at around 216 ℃, and the spinel phase is maintained above 337 ℃. According to the following theoretical calculation (M denoted by the Ni, Co, and Al ions);

$$Li_{0.33}M(^{3.67+})_{1.0}O_2 \text{ (layered, } R\bar{3}m) \rightarrow Li_{0.33}M(^{3.21+})_{1.0}O_{1.77} \text{ (Spinel, } Fd\bar{3}m) + 0.115O_2\uparrow$$

$$Li_{0.33}M(^{3.21+})_{1.0}O_{1.77} \text{ (Spinel, } Fd\bar{3}m) \rightarrow Li_{0.33}M(^{2.33+})_{1.0}O_{1.33} \text{ (Rock-salt, } Fm\bar{3}m) + 0.22O_2\uparrow$$

the amount of oxygen released is associated with the phase transitions. In this regards, the higher Ni content in layered cathode materials can lead to poor thermal stability with larger oxygen release and sever structural changes.

Secondly, the surface of Ni-rich cathode materials are very unstable when they are exposed to the atmosphere because the cathode materials react with atmospheric CO_2 and O_2. As a result, Li_2CO_3 impurities are formed on the surface of the cathode powders, as in the following reaction:[9]

$$Li(Ni, Co)O_2 + \frac{1}{2}xCO_2 + \frac{1}{4}xO_2 \rightarrow Li_{1-x}(Ni, Co)O_2 + \frac{1}{2}xLi_2CO_3$$

The lithium carbonate occurs side reaction with electrolytes and forms solid electrolyte interphase (SEI) layer, and it leads to deterioration of electrochemical properties of the cathode materials. Generally, $LiPF_6$ is used as salt for the electrolyte of Li-ion batteries due to its high ionic conductivity. However, the $LiPF_6$ is easily decomposed by the presence of moisture and produces strong Lewis acid of PF_5.[10] The consecutive decomposition reaction by PF_5 and HF causes the formation of an SEI layers such as LiF, Li_xPF_y, and $Li_xPO_yF_z$. The reaction model is represented in Figure 2.2.3. Those SEI layers can work as resistance on the surface of cathode materials because of poor ionic conductivity and Li-ion diffusion. Therefore, the electrochemical performances can therefore be diminished.

Thirdly, the Ni-based cathode materials are composed of an aggregation of many grains with anisotropic orientation. As mentioned above, the lattice of the cathode materials are changed in lithium insertion/desertion with volume change. Micro-cracks therefore occur in cycling. Those cleavages of the particles, which provide new active sites, can lead to a new SEI layer inside

particles through a side reaction with electrolytes (Figure 2.2.4).[11] Furthermore, the structural degradation was deepened by phase transition inside the particles.

These problems worsen at high voltage and high temperature during cycling. The batteries can easily expose to high temperature and overcharge state in our life. To use the battery with high performance and safety, the degradation problems should be solved.

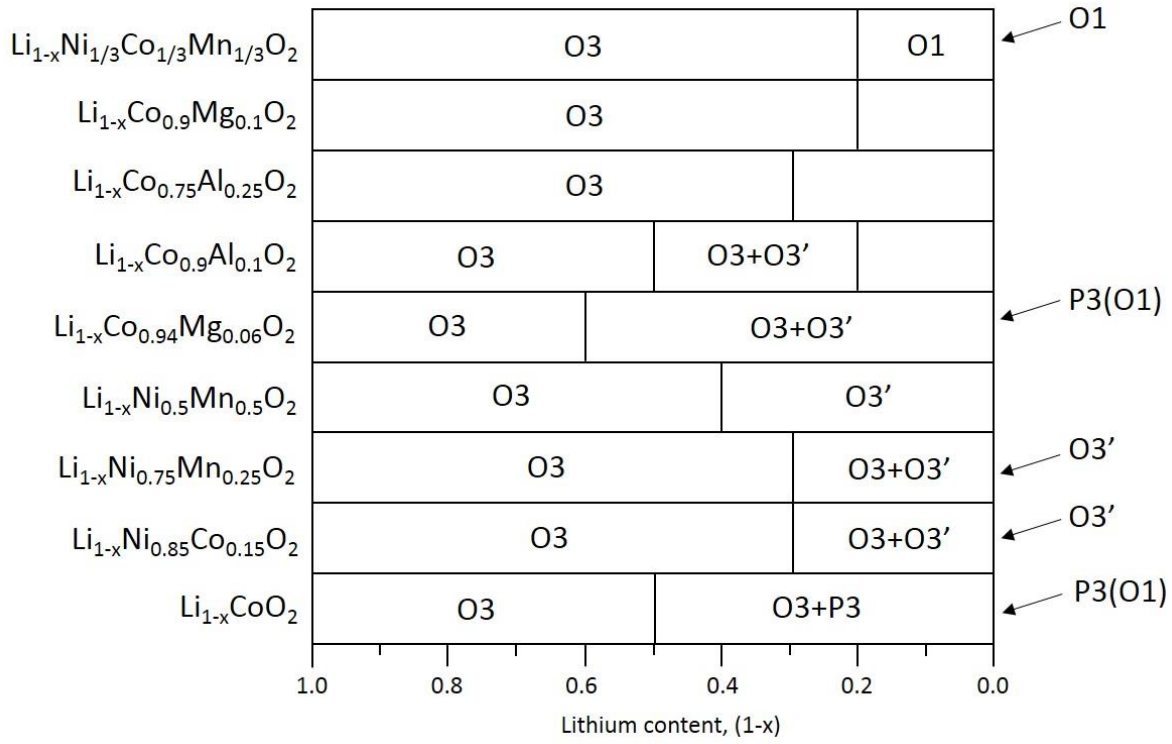

Figure 2.2.1. Phase transition of $LiMO_2$ layered cathode materials as different lithium content (copied by principles and applications of lithium secondary batteries)

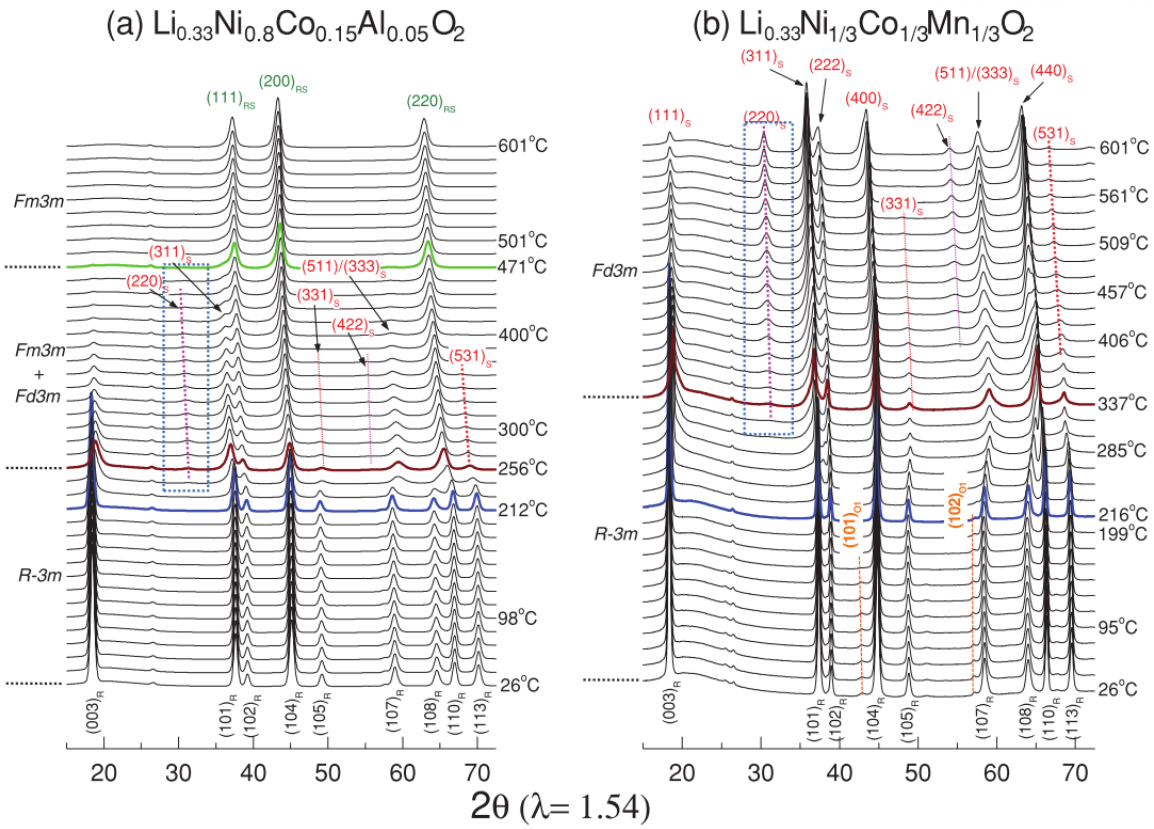

Figure 2.2.2. Time-resolved (TR) XRD patterns of the overcharged a) $Li_{0.33}Ni_{0.8}Co_{0.15}Al_{0.05}O_2$, and, b) $Li_{0.33}Ni_{1/3}Co_{1/3}Mn_{1/3}O_2$ during heating up to 600 ℃. The overcharged cathode samples sealed in quartz capillaries were heated from 25 to 600 ℃ for 4 h during the TR-XRD measurement (heating rate = 2.4 ℃ min^{-1}). The subscripts R, S, and RS denote rhombohedral, spinel, and rock-salt structure, respectively. The subscript O1 represents CdI_2-type MO_2 (M = Ni, Co and Mn) structure. The expanded (220)s peak regions.[2]

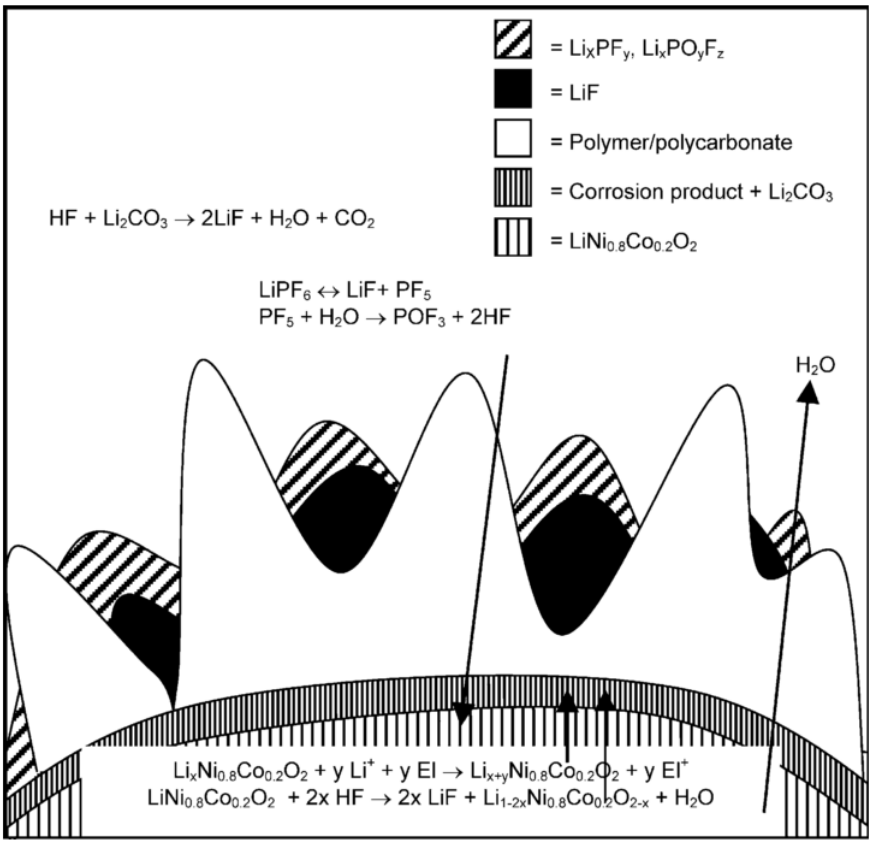

Figure 2.2.3. A proposed model for the SEI surface layer on a $LiNi_{0.8}Co_{0.2}O_2$ electrode.[9]

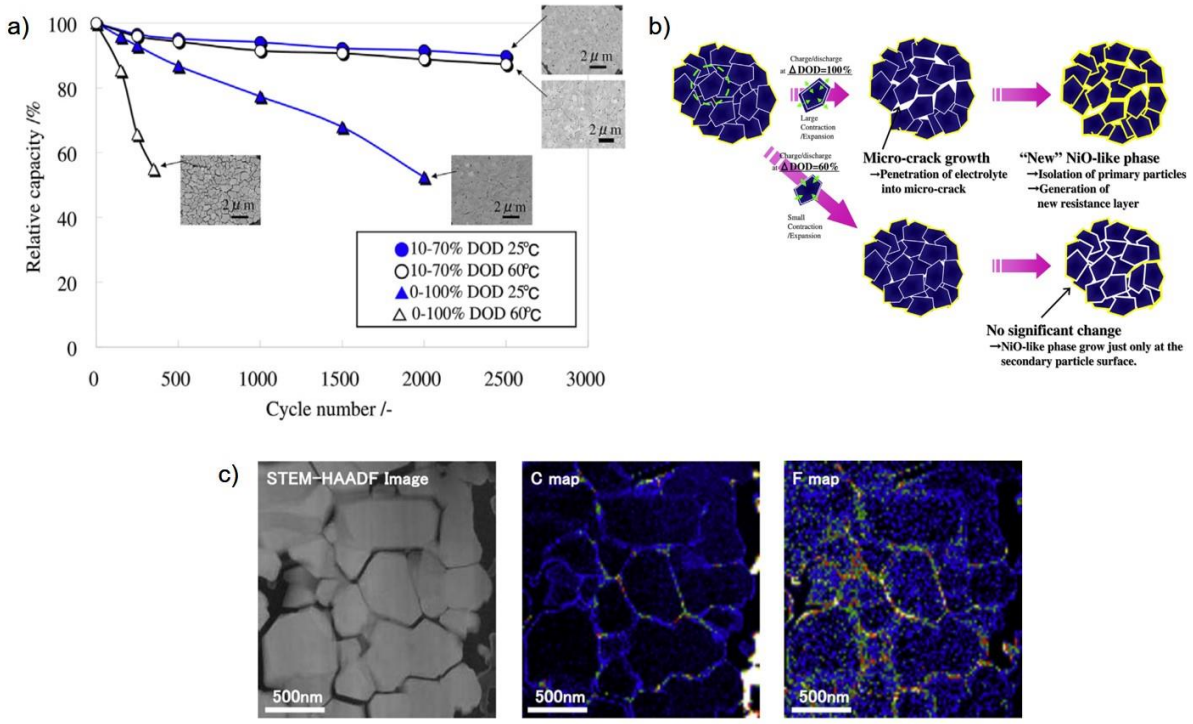

Figure 2.2.4. a) Cycle performance of cylindrical model cells and cross-sectional SEM images of the NCA cathode in two ΔDOD conditions at 25 and 60 °C; (●) 10 - 70% at 25 °C, (○) 10 - 70% at 60 ℃, (▲) 0 - 100% at 25 °C and (Δ) 0 -100% at 60 ℃. b) A schematic model for the deterioration of NCA particle during cycle test. c) HAADF-STEM images and maps of C and F atoms for an NCA particle after 350 cycles in the ΔDOD of 0 - 100% at 60 ℃.[11]

2.3 Surface modification of Ni-rich cathode materials

To improve the electrochemical properties and safety of Ni-rich cathode materials, many researchers have studied surface modifications such as surface coating, hetero-structure, concentration gradient, etc. In the case of the metal oxide coating, the coating layer acts as a protecting layer and effectively diminishes the side reaction with electrolytes on the surface of particles. In 2001, Cho et al. reported the ZrO_2 coating effect for the $LiNiO_2$ cathode material.[12] According to the literature, zirconium oxide encapsulates the $LiNiO_2$ as a thin film and suppresses the dimensional change during lithium intercalation/deintercalation. The XRD pattern of ZrO_2-coated cathode material shows peak broadening without new peaks when compared to a pristine sample. This is considered as a surface reaction between ZrO_2 and $LiNiO_2$ during calcination, and it can form a thin $LiNi_{1-y}Zr_yO_2$ solid-solution layer surrounding the $LiNiO_2$ particle. Al_2O_3-coated $LiCoO_2$ and $LiMnO_2$ materials show similar surface reactions.[13] While the pristine sample shows multiphase transition with the electrochemically induced compositional changes during lithiation/delithiation, the ZrO_2-coated sample suppress the phase transition, H1→ M, M → H2, and H2 → H3 (M and H represent monoclinic and hexagonal, respectively). The M → H2 and H2 → H3 phase transitions affect the capacity fading in cycling as shown in Figure 2.3.1. This means that the metal oxide coating shows improvements in the structural stability of the cathode materials in lithium intercalation/deintercalation. However, the metal oxide coating cannot solve the thermal stability of the Ni-rich cathode materials.

Manganese ions provide thermal stability for the cathode materials by higher Mn-O bonding in layered structure than other transition metals. For example, concentration-gradient cathode material was reported by Sun et al. in 2009.[14] The cathode material is composed of Ni-rich bulk and Mn-rich outer layer in one particle and synthesized by the co-precipitation method. The Co and Mn concentrations increased from inter-surface (10%) to outer surface (22%) between different compositions. Meanwhile, the Ni concentration decreased gradually from bulk (80%) to outer layer (56%) as shown in Figure 2.3.2. This cathode material shows a high capacity based on the bulk composition of $Li[Ni_{0.8}Co_{0.1}Mn_{0.1}]O_2$, and an improvement of capacity retention and safety. The enhanced electrochemical properties are attributed from concentration-gradient outer layer and the surface composition of $Li[Ni_{0.46}Co_{0.23}Mn_{0.31}]O_2$.

Cho et al. reported the spinel-layered core-shell cathode material with an average composition of $Li[Ni_{0.54}Co_{0.12}Mn_{0.34}]O_2$ to improve the thermal stability.[15] The core and shell of the material consist of the spinel ($Fd\bar{3}m$) and the layered ($R\bar{3}m$) structure, respectively. The spinel structure on the surface effectively suppressed the phase transition related to the oxygen loss from the lattice, as in the following equation:

$$2Li_{z/2}NiO_2 \text{ (layered)} \rightarrow 2O_2\uparrow + Li_zNi_2O_4 \text{ (spinel)}$$

The differential scanning calorimetry (DSC) measurements of a fully charged sample were implemented to compare the thermal stability. The total generated heat (amount of oxygen release) of the core-shell structure was significantly decreased to 310 J g^{-1}, which is 3-4 times lower than in a pristine sample. In addition, the cathode material shows good capacity retention at high temperature of 60 ℃.

These researches have been focused on secondary particles' surface reaction and modification, and they shows improved electrochemical performance with suppressed side reaction between particles' surface and electrolytes. However, micro-crack in the particle is the important factor of diminishing the electrochemical performance and stability. To obtain the remarkable improvement of the performance and stability of the batteries, we should control the micro-cracks in cycling. In this regard, I suggested the surface treatment of primary particle to secure the structural stability and suppress the micro-cracks inside the particle.

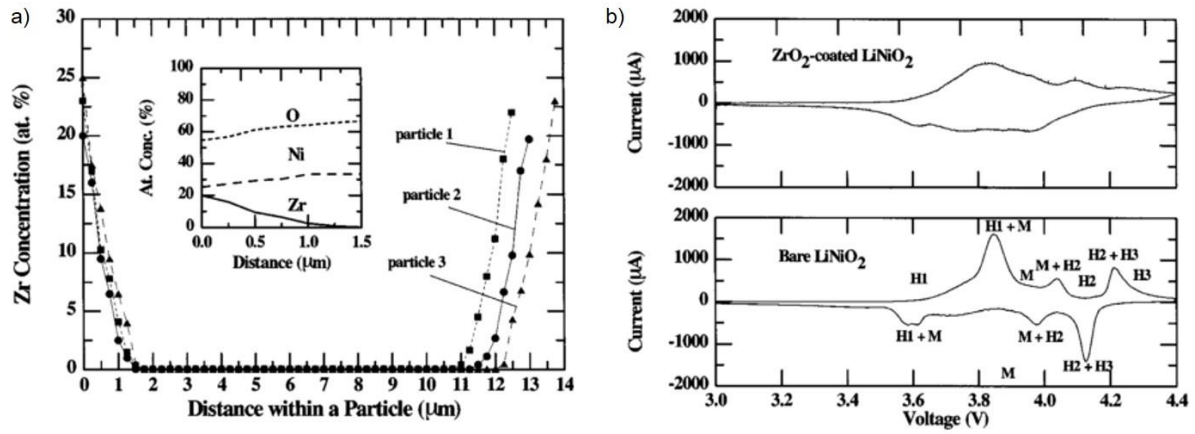

Figure 2.3.1. a) EPMA analysis of Zr distribution near the surface of $LiNiO_2$ particle. The inset shows elemental analysis of Zr, O, and Ni inward from the particle surface. b) Cyclic Voltammetry (CV) of bare and coated samples with the scan rate of 0.02 mV s^{-1}.[12]

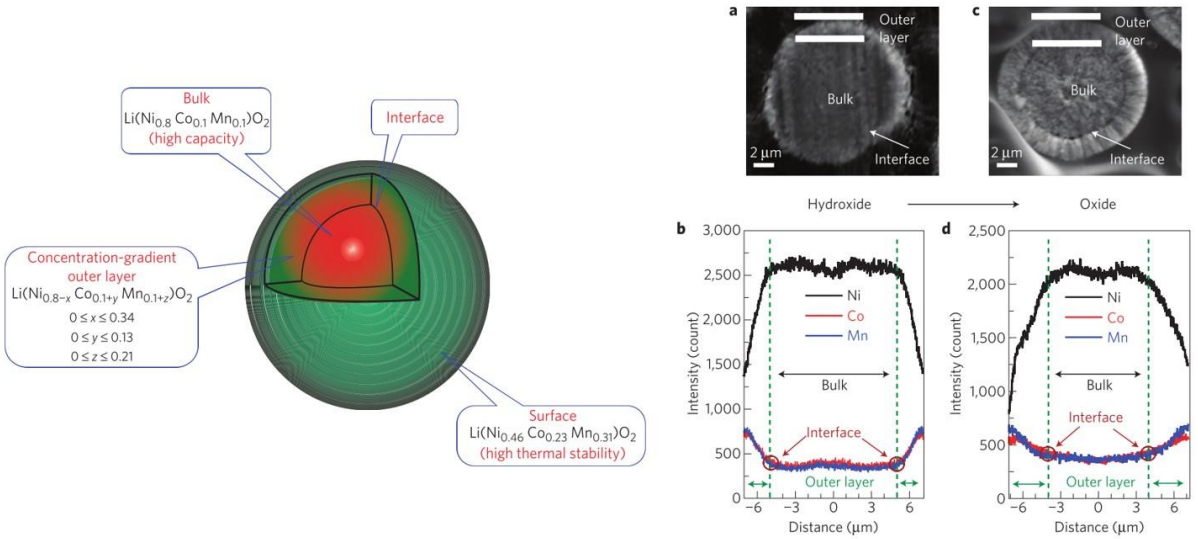

Figure 2.3.2. (Left side) Schematic diagram of concentration-gradient cathode material. (Right side) Scanning electron microscopy (SEM) and electron-probe X-ray micro-analysis (EPMA) results. SEM images of a) precursor metal hydroxide and c) final lithiated metal oxide. EPMA line scan results of b) precursor metal hydroxide and d) final lithiated metal oxide.[14]

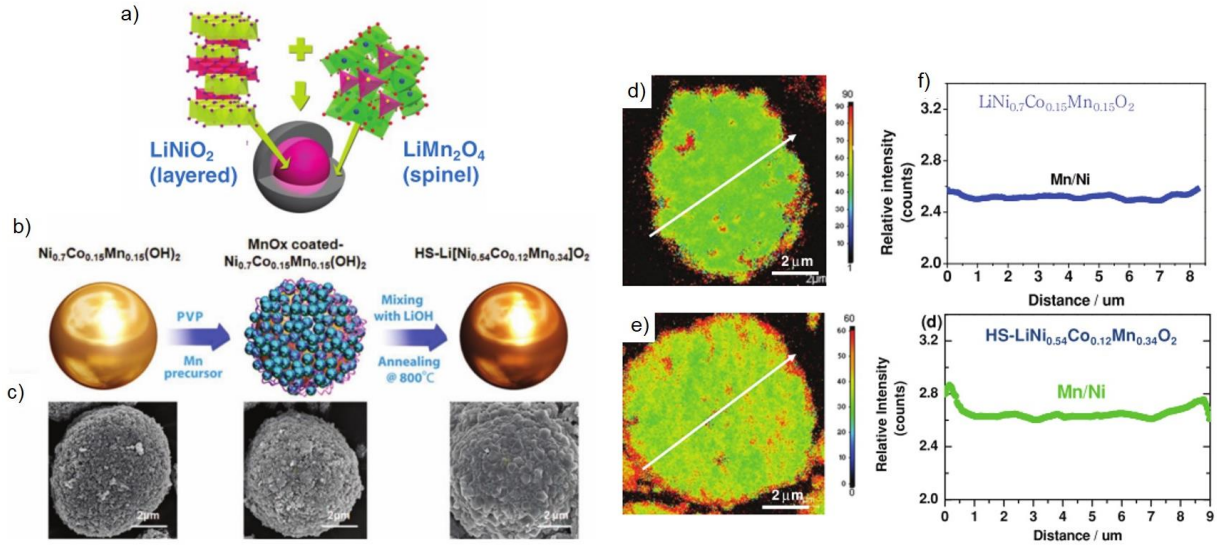

Figure 2.3.3. a) Schematic diagram of a core-shell structure. b) Schematic view for the synthetic method of the heterostructures. c) SEM images of the particles corresponding to Figure 2.3.3a.[15]

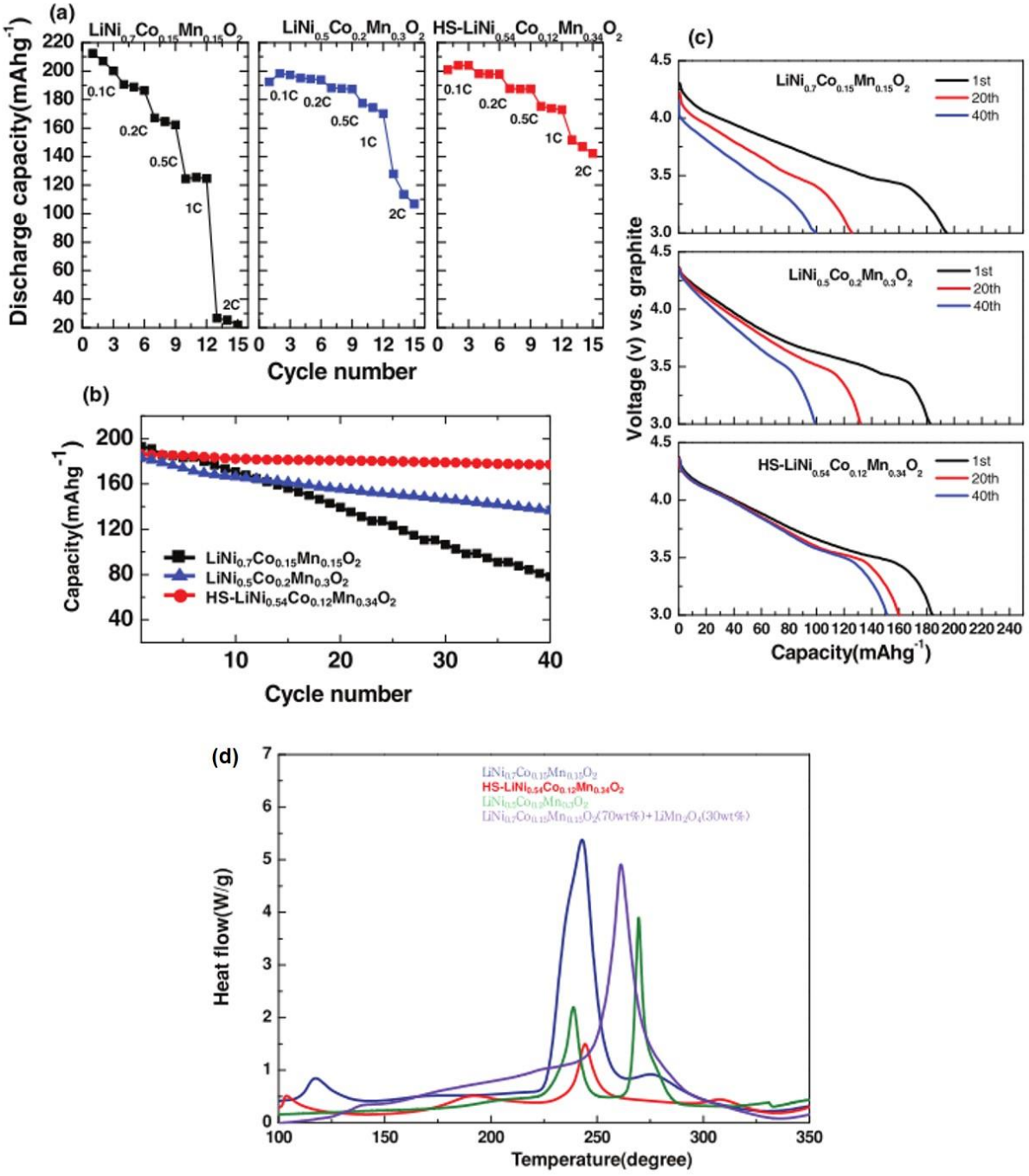

Figure 2.3.4. a) Rate capability of the pristine ($LiNi_{0.7}Co_{0.15}Mn_{0.15}O_2$), reference ($LiNi_{0.5}Co_{0.2}Mn_{0.3}O_2$), and core-shell materials ($HS\text{-}LiNi_{0.54}Co_{0.12}Mn_{0.34}O_2$) at different c-rates between 3.0 and 4.5V in coin-type half-cell. b) Capacity retentions of the three samples (pristine, reference, and core-shell hetero-structure materials) at 0.5C charge and discharge rate. c) Voltage profiles of the three samples (pristine, reference, and core-shell hetero-structure materials) for the discharge process at 1st, 20th, and 40th cycles at 60 °C. d) DSC profiles of the pristine ($LiNi_{0.7}Co_{0.15}Mn_{0.15}O_2$), reference ($LiNi_{0.5}Co_{0.2}Mn_{0.3}O_2$), and core-shell materials ($HS\text{-}LiNi_{0.54}Co_{0.12}Mn_{0.34}O_2$) after charging up to 4.5 V.[15]

Ⅲ. Experiment

3.1 New Coating Method for Alleviating Surface Degradation of $LiNi_{0.6}Co_{0.2}Mn_{0.2}O_2$ Cathode Material: Nano-scale Surface Treatment of Primary Particles

3.1.1 Introduction

Cathode materials for the next generation of lithium-ion batteries require higher energy density, longer cycle life, and better safety for applications in electric vehicles and stationary energy storage.[16] Nickel-rich systems ($LiNi_xM_{1-x}O_2$; M = Mn, Co, and Al; $x > 0.5$) are considered as promising candidates to meet such requirements, although their structural degradation and thermal instability pose challenging hurdles.[17] These problems worsen with higher Ni content, higher temperature, and higher cut-off voltage (>4.4 V vs. Li^+/Li).[18] In general, Ni-rich cathode materials with a layered structure commonly undergo structural degradation from the layered phase ($R\bar{3}m$) to the spinel-like phase ($Fd\bar{3}m$) and rock-salt phase ($Fm\bar{3}m$) during cycling and at an elevated temperature.[17b, 18-19] The structural change is caused by the migration of the transition metal (TM) ions into the lithium layer during charging and discharging.[20] The TM ions' migration leads to the layered-to-spinel phase transformation, and the transformation is intensified by high-voltage and high-temperature cycling because of the increasing number of vacant Li sites during full delithiation and the diffusion of TM ions. These phase transitions with TM-ion migration are accompanied by changes in the lattice constants and volume, which release oxygen from the lattice. Such results can lead to thermal and structural instability.[21]

The Ni-rich cathode materials, commonly prepared by a general co-precipitation method, are composed of round-shape secondary particles in which many micrometer-sized primary particles (grains) are aggregated.[22] Since all these primary particles have different crystallographic orientation and slip planes, anisotropic lattice volume expansion or contraction between the grains during lithium intercalation or de-intercalation result in micro-cracks that act as new reaction sites with the electrolytes, in turn leading to electrical disconnection between the grains.[23] As a result, a new solid electrolyte interface (SEI) layer, comprising decomposition products of the electrolyte, is formed along the active surface of the primary particles (grains) developed by the micro-cracks. The SEI layers on the surface of the grains inhibit electron and lithium transport through the grain–electrolyte interface, thus diminishing the electrical performance.[11] To resolve the structural and thermal instability of the Ni-rich cathode materials, many researchers have implemented surface modification such as surface coating (Al_2O_3, $AlPO_4$, ZrO_2)[24] and developed core–shell structures.[25] Although the structural degradation is intensified during cycling because of the microstructural evolution caused by the reaction between primary particles and the electrolyte inside the secondary

particles,[11, 26] most researchers have focused on the surface modification of the secondary particles.[24a, 25, 27]

Herein, we propose the nanoscale surface treatment of primary particles of $LiNi_{0.6}Co_{0.2}Mn_{0.2}O_2$ cathode material using a mixed ethanol solution with dissolved lithium and cobalt precursors. This new approach resulted in improved structural and thermal stability under severe conditions such as high cut-off voltage (>4.4 V) and high temperature (>50 ℃).

3.1.2 Experimental method

Preparation of electrode materials: The cathode materials of $LiNi_{0.6}Co_{0.2}Mn_{0.2}O_2$ were synthesized by a co-precipitation method.[28] The ST-NCM sample was prepared from a fully ionized solution. First, 0.17 mol of CH_3COOLi and 0.2 mol of $(CH_3COO)_2Co$ were completely dissolved in ethanol (50 g). Next, 100 g of the cathode powder synthesized as cathode material was added to the solution. The mixed solution was vigorously stirred at 70 ℃ until the solvent completely evaporated. Finally, it was calcinated at 800 ℃ for 4 h in air to remove the impurities after drying at 150 ℃ for 1 h.

Electrochemical properties: The electrochemical properties were tested in a coin-type 2032R cell with a lithium-metal anode. Composite electrodes were prepared with 92% active material, 4% Super-P carbon black, and 4% poly(vinylidene fluoride) (PVDF) binder in *N*-methyl-2-pyrrolidinone and cast onto aluminum current collectors with active material loadings of 8–9 mg/cm^2. The electrolyte for the half-cells was 1.15 M $LiPF_6$ with ethylene carbonate–dimethylene carbonate–diethylene carbonate (30:40:30 vol%) (Panax Etec). The cycling tests of the half-cell were performed between 3.0 and 4.45 V at a 0.5 C charge rate and a 1 C discharge rate at 60 ℃.

Materials characterization: Powder X-ray-diffraction (XRD) (D/Max2000, Rigaku) measurements at 2θ = 10–80 °, using Cu K α radiation, were used to identify the phases. The morphology of the samples was observed using scanning electron microscopy (SEM). The cross-sectional TEM samples of particles were prepared by a focused ion beam (FIB) technique (FEI Helios Nano Lab 450). Additionally, the samples were thinned by a low-energy Ar-ion milling system (Fischione Model 1040 Nanomill). The HAADF-STEM images were taken using a probe-side aberration corrected TEM ((JEOL JEM-2100F). EELS spectra were recorded using an image-side aberration corrected TEM (FEI Titan^3 G2 60-300) operated at an accelerating voltage of 80 KV. *In situ* transition metal (Ni, Co, Mn) K-edge X-ray absorption near edge structure (XANES) and extended X-ray absorption fine structure (EXAFS) spectra were collected on BL10C beam line at the Pohang Accelerator Laboratory (PAL), Korea. The monochromatic X-ray beam can be obtained from high intense X-ray photons of multiple wiggler source using liquid-nitrogen cooled Si (111) double crystal monochromator (Bruker ASC). The transimitted XAFS spectra were collected using home-made heating stage in the temperature region from room temperature to 450 ℃ for ~4h (i.e., heating rate= 2 ℃/min). Differential scanning calorimetry (DSC) samples of the cathodes were prepared by charging to 4.5 V at a 0.1 C rate and then the dissembled electrodes were prepared in the dry-room. The dissembled electrodes washed with dimethyl carbonate (DMC) solvent several times, and fresh electrolytes added after drying the electrode. The electrode transferred to aluminum pan and heated at a rate of 5 ℃/min.

3.1.3 Results and Discussion

The schematic illustration in Figure 3.1.1a shows the surface treatment process for the primary particles of $LiNi_{0.6}Co_{0.2}Mn_{0.2}O_2$ (NCM). A completely ionized solution consisting of lithium and cobalt ions could penetrate the core part of the particle along the grain boundaries because there were many empty microspaces between the primary particles. The cathode material was calcined at 800 ℃ for 4 h (denoted as ST-NCM), and the calcinated particles had a smooth surface, with no morphological changes when compared with the pristine sample (Figure 3.1.2). However, the Al_2O_3-coated reference samples clearly showed that the coated nanoparticles were distributed throughout the surface of the secondary particles because Al-isopropoxide, which was used as a precursor, was precipitated as $Al(OH)_3$ nanoparticles in the isopropanol solvent (Figure 3.1.2). Figure 3.1.1b shows a cross-sectional scanning electron microscope (SEM) image of a NCM particle composed of the aggregated, fine, micrometer-sized primary particles. Scanning transmission electron microscope (STEM) image in Figure 3.1.1c shows many microvoids between the particles, enabling the surface treatment solution to penetrate the core. Energy-dispersive X-ray spectroscopy (EDXS) of the ST-NCM sample (along the yellow arrow in Figure 3.1.1c) confirmed the higher content of Co atoms than Mn and Ni atoms at a depth of ~60 nm into the interior (Figure 3.1.1d and Figure 3.1.3). The higher Co content in the Ni-based cathode materials led to better electrochemical performance.[29] In addition, the EDXS result of randomly selected primary particle showed same trend to Figure 3.1.1d (Figure 3.1.4).

Figure 3.1.5 presents more detailed structural and chemical information on a primary particle's surface, obtained by high-angle annular dark field (HADDF)-STEM and electron energy-loss spectroscopy (EELS) analysis of the samples. Region 1 of the pristine $LiNi_{0.6}Co_{0.2}Mn_{0.2}O_2$ (NCM) sample exhibited an uneven NiO-like cation-mixing (CM) layer with a space group of $Fm\bar{3}m$ and thickness of 1–2 nm, as shown in Figure 3.1.5b (also refer to Rietveld refinement results in Fig. 3.1.6 and Table 3.1.1). Here, bright spots of Li slabs resulted from Ni^{2+} migration from the original TM slabs to lithium slabs because Ni^{2+}, which has an ionic radius (0.69 Å) similar to that of Li^+ (0.76 Å), could easily move to Li sites. The layered phase with a space group of $R\bar{3}m$ was verified by the fast Fourier-transform (FFT) pattern (inset of Figure 3.1.5c). In the ST-NCM sample, region 1 consisted of the CM layer with a thickness of ~10 nm, as confirmed by the FFT pattern (inset of Figure 3.1.5e). In region 2, however, Figure 3.1.5f shows that only the layered (space group of $R\bar{3}m$) phase was observed, which is identical to the result for the pristine NCM sample. The NiO-like phase with a nanometer-range thickness has been reported to act as a pillar layer that suppress the inter-slab collapse during cycling;[27d] therefore, particle pulverization is expected to be also reduced in our study.

More detailed observation on the surface chemical state of primary particles of the NCM and ST-NCM cathodes was carried out with EELS. The EELS profiles of the O K-edge and Mn $L_{2,3}$-edges located around 530 and 640 eV, respectively, are directly linked to the electronic structure of the materials (Figure 3.1.5g and h). The ratio of the integrated intensities of L_3 and L_2, $I(L_3)/I(L_2)$, is correlated with the valence state of the transition metals, and increasing the $I(L_3)/I(L_2)$ ratio corresponds to decreasing the oxidation state of manganese ions.[30] Table 3.1.2 summarizes the integrated $I(L_3)/I(L_2)$ ratio for the each region of the NCM and ST-NCM samples. Region 2 of the NCM sample had a $I(L_3)/I(L_2)$ ratio of 1.98, which is indicative of the dominance of Mn^{4+}. However, region 1 of the NCM sample had a $I(L_3)/I(L_2)$ ratio of 3.02, indicating a lower valence state of $Mn^{\sim 2.7+}$ than that in region 2. On the other hand, the ST-NCM sample had a quite similar ratio of ~2.0, which is consistent with the presence of Mn^{4+} between the two regions. The pre-peak of the O K-edge near 530 eV, as indicated by the red arrow in Figure 3.1.5g and h, was reported to be the result of the transition from the O 1s state to the O 2p−TM 3d hybridized state.[31] This peak became weaker and shifted to a higher energy as the oxidation state of Mn decreased because of the weakened hybridization of the O 2p–Mn 3d orbital owing to the 3d orbital of Mn with the filled e_g state.[30b] In Figure 3.1.5g, the pre-peak of the O K-edge weakened and shifted to a higher energy owing to the low oxidation state of Mn^{3+} in region 1 of the NCM sample. However, the ST-NCM sample showed no difference between the pre-peaks for both regions because of the same oxidation state of Mn^{4+}. Consequently, we can recognize that the Mn ions in the NCM sample had mixed oxidation states of 3+ and 4+ on the surface of the primary particles. Generally, the oxidation states of Ni, Co and Mn in $LiNi_{1-x-y}Co_xMn_yO_2$ cathode materials are 2+, 3+, and 4+, respectively, with small concentrations of Ni^{3+} and Mn^{3+} ions.[27d, 32] When Ni^{3+} and Mn^{3+} serve as the Jahn–Teller active ions, Jahn–Teller (J–T) distortions are allowed by breaking the symmetry of the cell.[33] In the case of the ST-NCM sample, the CM layer on the surface, which resulted from the migration of Ni^{2+} ions from TM slabs to Li slabs, induced a higher Mn^{4+} proportion to compensate the charge valence (Figure 3.1.7). The high average oxidation state of Mn^{4+} in the ST-NCM sample could effectively diminish the J–T distortion.

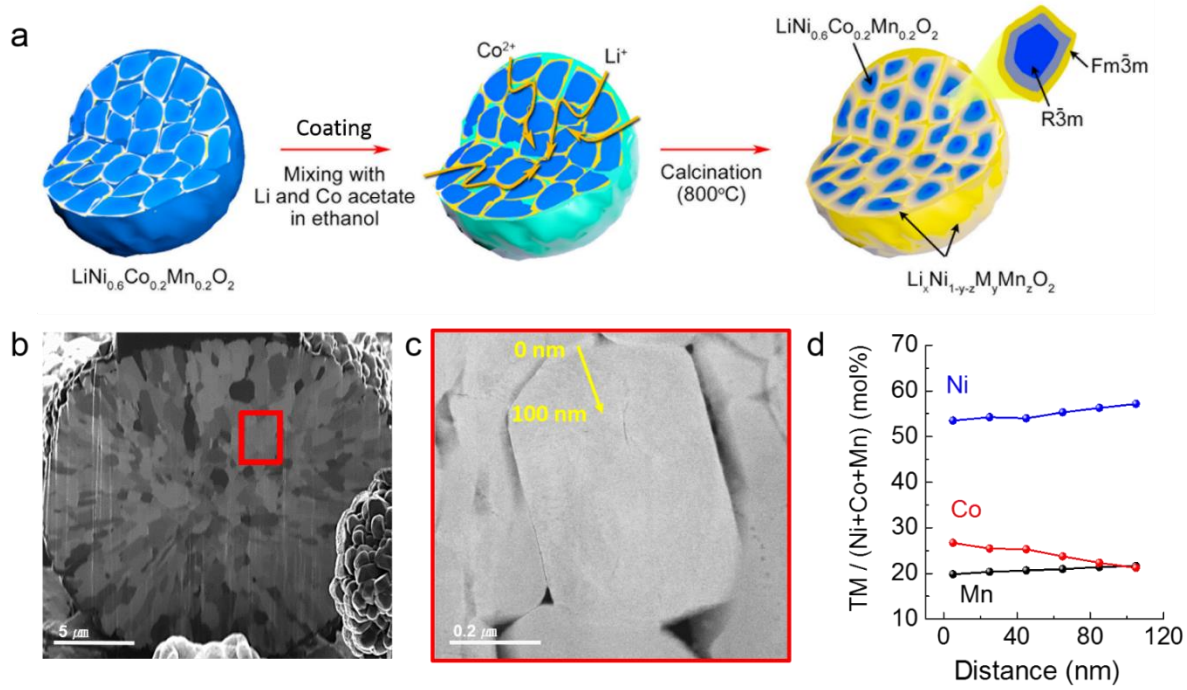

Figure 3.1.1. (a) Schematic diagram of the surface treatment on the primary particles. (b) Cross-sectional SEM image of the synthesized ST-NCM cathode material. (c) STEM image of the primary particle in the region indicated by a red rectangle in (b). (d) EDXS profile of the ST-NCM surface corresponding to the yellow arrow in (c).

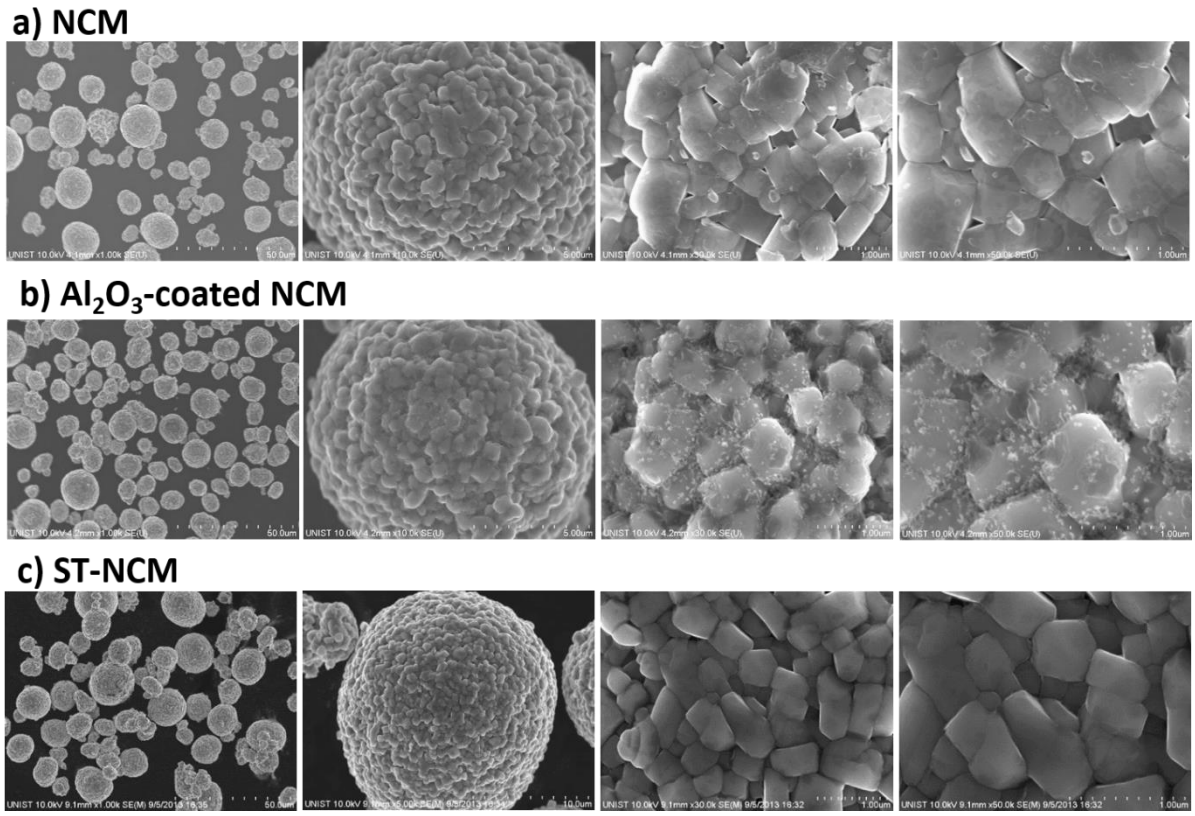

Figure 3.1.2. SEM images of the (a) NCM, (b) Al_2O_3-coated NCM, and (c) ST-NCM samples after surface modifications.

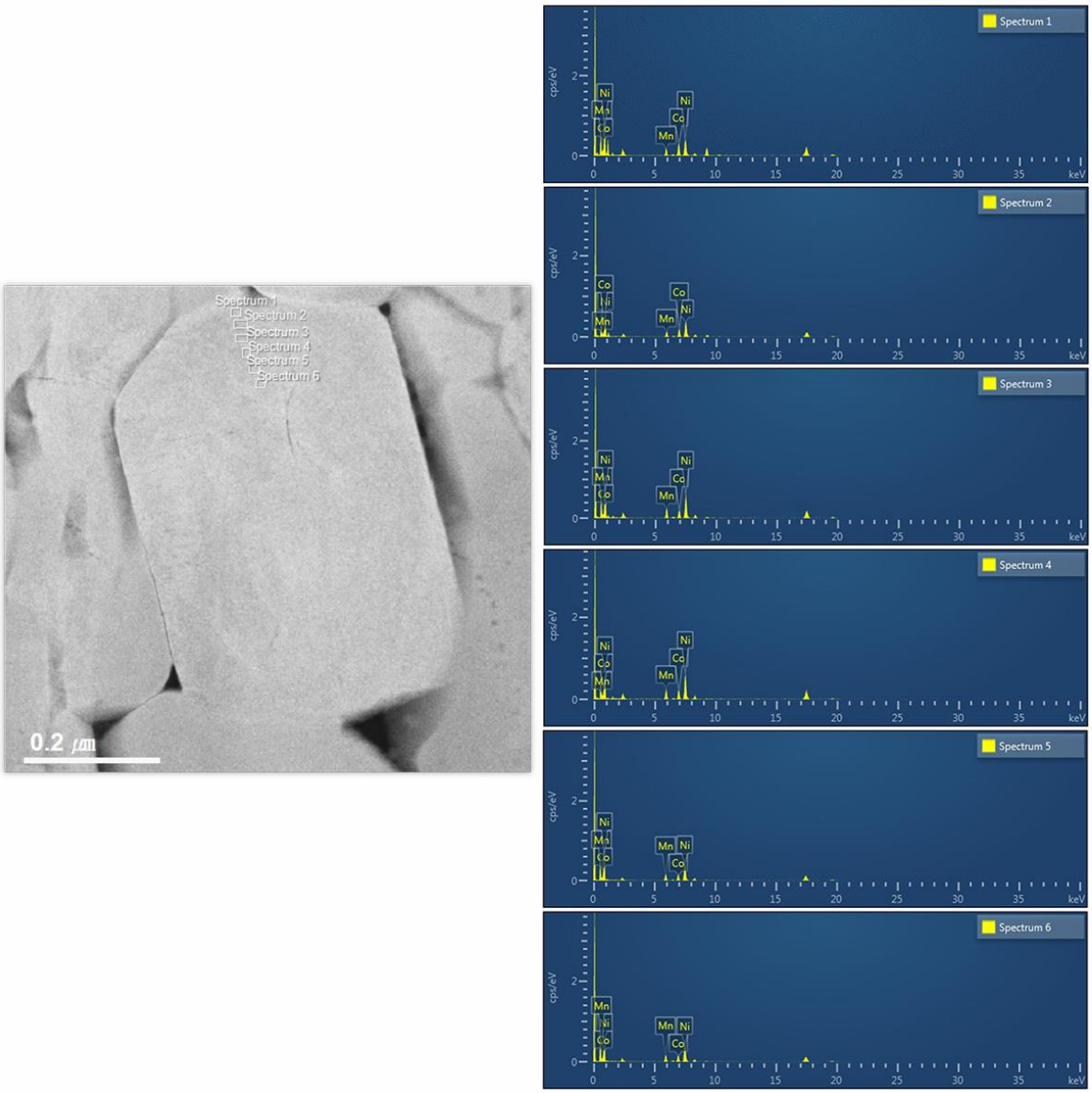

Figure 3.1.3. EDXS data of ST-NCM at the six different point to clarify the EDXS profile of Figure 1d.

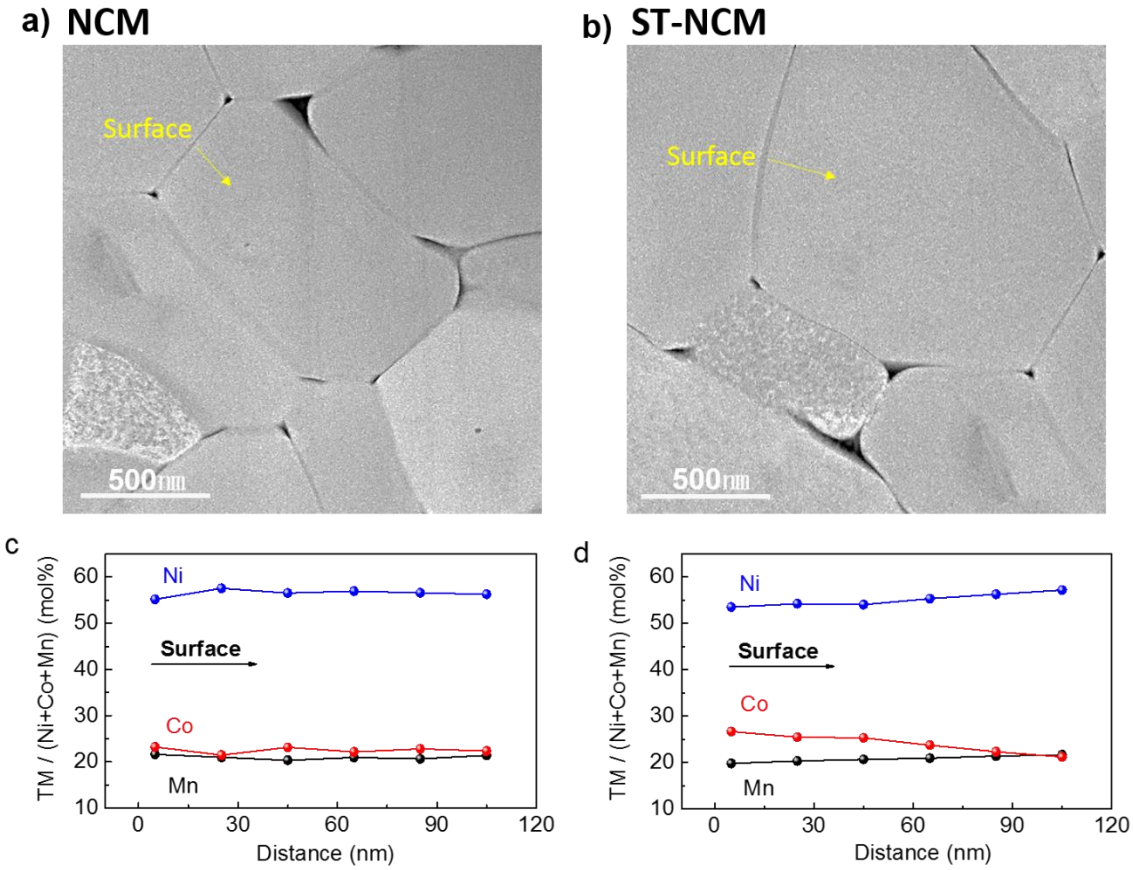

Figure 3.1.4. HR-TEM images of the inner primary particles (grains) for the (a) NCM and (b) ST-NCM particles. EDX profiles from outer side to inner side on the surface of the primary particle for the (c) NCM and (d) ST-NCM particles.

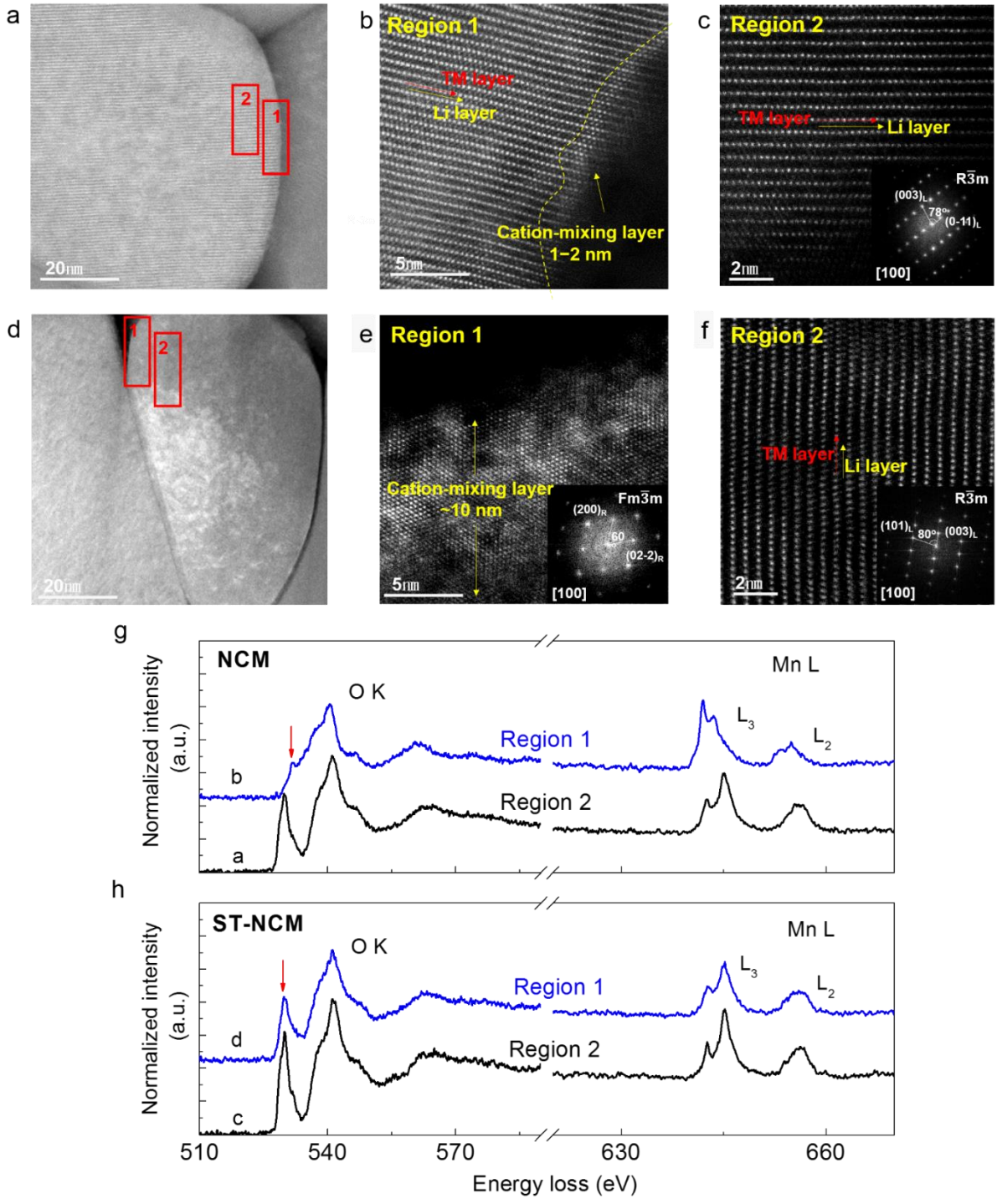

Figure 3.1.5. HADDF-STEM image of (a) $LiNi_{0.6}Co_{0.2}Mn_{0.2}O_2$ (NCM) on the surface of a primary particle (grain). Magnified STEM image of the NCM in (b) Region 1 and (c) Region 2 in (a). HAADF STEM image of (d) surface-treated $LiNi_{0.6}Co_{0.2}Mn_{0.2}O_2$ (ST-NCM) on the surface of the primary particle (grain). Magnified STEM image of the ST-NCM in (e) Region 1 and (f) Region 2 in (d). The insets of STEM images show digitalized fast-Fourier-transformed (FFT) patterns. EELS spectra obtained on the surface of a primary particle in Regions 1 and 2 of (g) NCM and (h) ST-NCM.

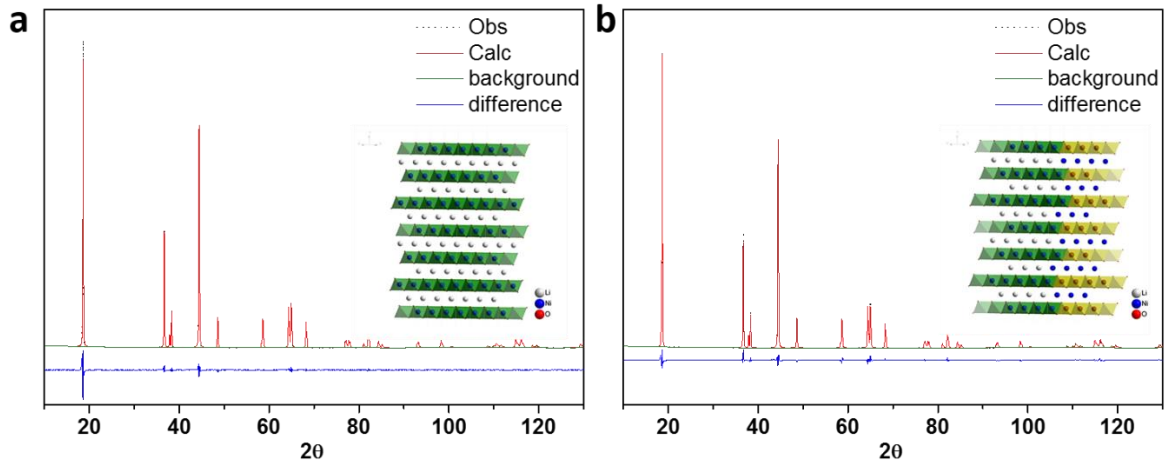

Figure 3.1.6. XRD patterns with Rietveld refinement plot for the (a) NCM and (b) ST-NCM samples.

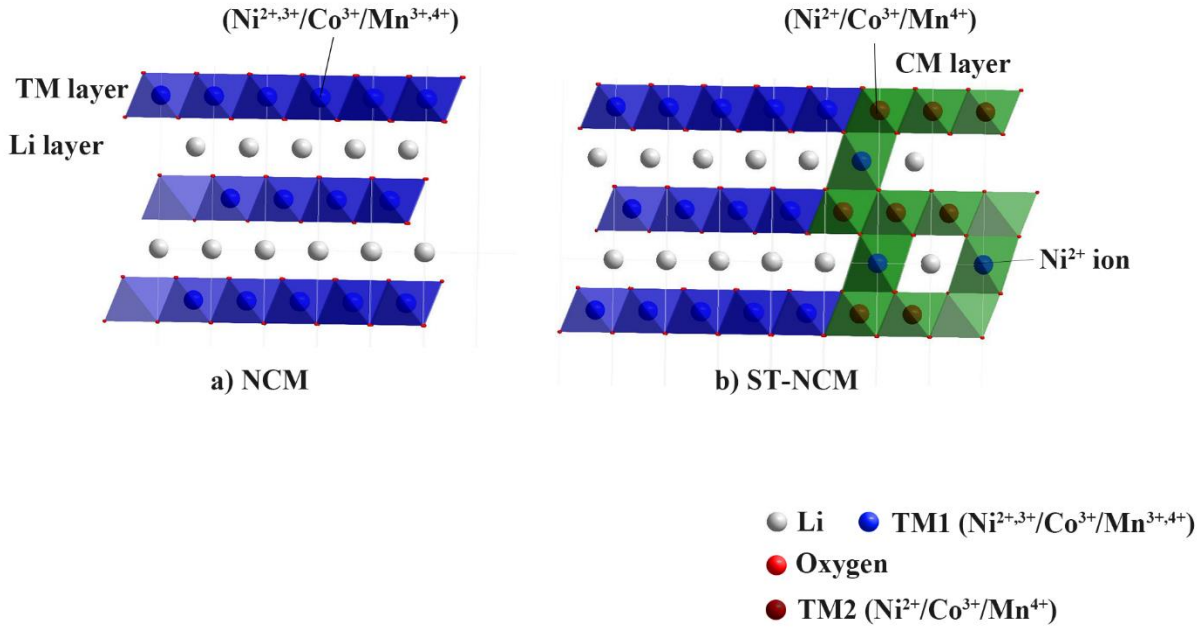

Figure 3.1.7. Structure of the NCM and ST-NCM samples for the primary particle. (a) General layered structure of NCM, (b) Mixed structure of ST-NCM with layered and CM layer. The oxidation state of transition metals indicated for each material.

The electrochemical properties of each sample were evaluated using coin-type 2032R lithium half-cells between 3.0 to 4.45 V at 60 ℃. The first charge–discharge profiles of the NCM and ST-NCM samples at room temperature (RT, 25 ℃) displayed no capacity decrease even after surface treatment, with discharge capacities of 192 mAh g^{-1} (Figure 3.1.8a). The ST-NCM sample also showed higher capacity retention of 80% after 150 cycles (from 195 to 156 mAh g^{-1}) than the NCM sample (65% retention from 198 to 130 mAh g^{-1}), as shown in Figure 3.1.8b. In addition, the ST-NCM sample exhibited better cycle performance than the Al_2O_3-coated sample (Figure 3.1.9c). The voltage profiles corresponding to Figure 3.1.8b indicate that the average working voltage of the NCM sample became higher than that of the ST-NCM sample with increasing cycle number during charging (Figure 3.1.8c). Differential curves of the NCM and ST-NCM samples for 150 cycles at 60 ℃ revealed dominant double peaks at around 3.7 V, which are related to the phase transition from the hexagonal1 (H1) phase to the monoclinic (M) phase in the charging process. As the number of cycles increased, the peak at 3.75 V of the ST-NCM sample maintained a similar intensity after 150 cycles, in contrast to the peak of the NCM sample (Figures 3.1.8d). The decreasing peak intensity of the NCM sample is associated with the irreversible phase transition from H1 to M that was caused by the J–T distortion of transition-metal ions such as Ni^{3+} and Mn^{3+}.[34] In this aspect, the J–T inactive Mn^{4+} ions in the CM layer, on the primary particles' surface of the ST-NCM sample, prevented the irreversible phase transition by suppressing the distortion. Despite the formation of the CM layer, the rate capability of the ST-NCM sample was quite similar to that of the NCM sample (Figure 3.1.8e). According to Ceder et al.,[35] Li diffusion in a cation disordered rock-salt phase proceeds by Li ions hopping from one octahedral site to another via an intermediate tetrahedral site (o-t-o diffusion). Thus, the thin CM layer of the NiO-like phase on the surface of ST-NCM primary particles led to the favorable rate performance with no Li-diffusion limitation.

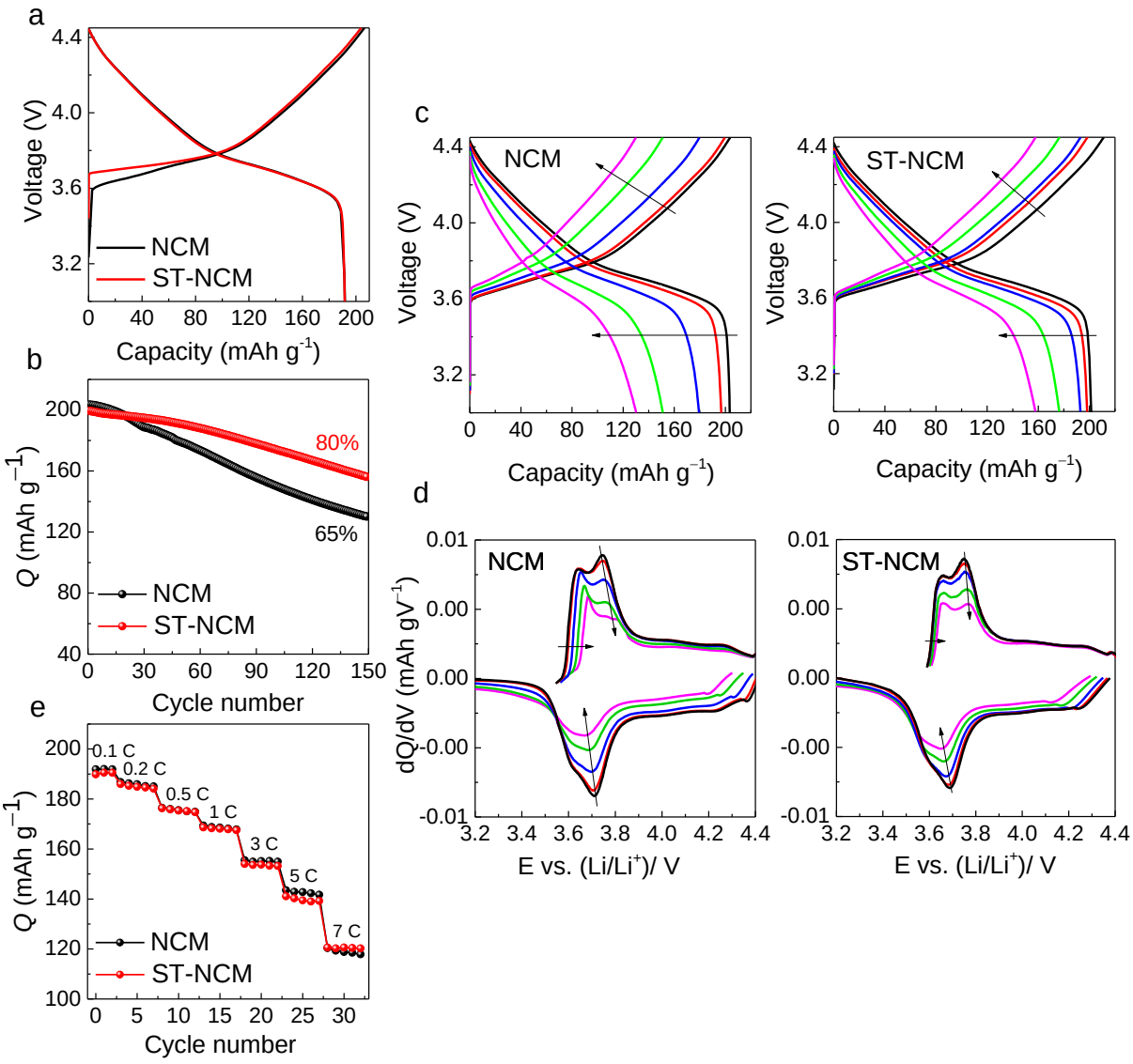

Figure 3.1.8. (a) First charge–discharge profiles of the NCM and ST-NCM samples at 0.1 C rate between 3.0 and 4.45 V at 25 ℃. (b) Cycle performance of the NCM and ST-NCM samples between 3.0 and 4.45 V at 60 ℃ (charge rate: 0.5 C; discharge rate: 1 C, *Q* = discharge capacity). (c) Charge and discharge voltage profiles of the NCM and ST-NCM samples after the 10th, 20th, 50th, 100th, and 150th cycles at 60 ℃ (each cycle matched with black, red, blue, green, and pink color lines, respectively). (d) Differential curves of the NCM and ST-NCM samples corresponding to (c). (e) Rate capabilities of NCM and ST-NCM evaluated between 3.0 and 4.45 V at 25 ℃. (*Q* = discharge capacity)

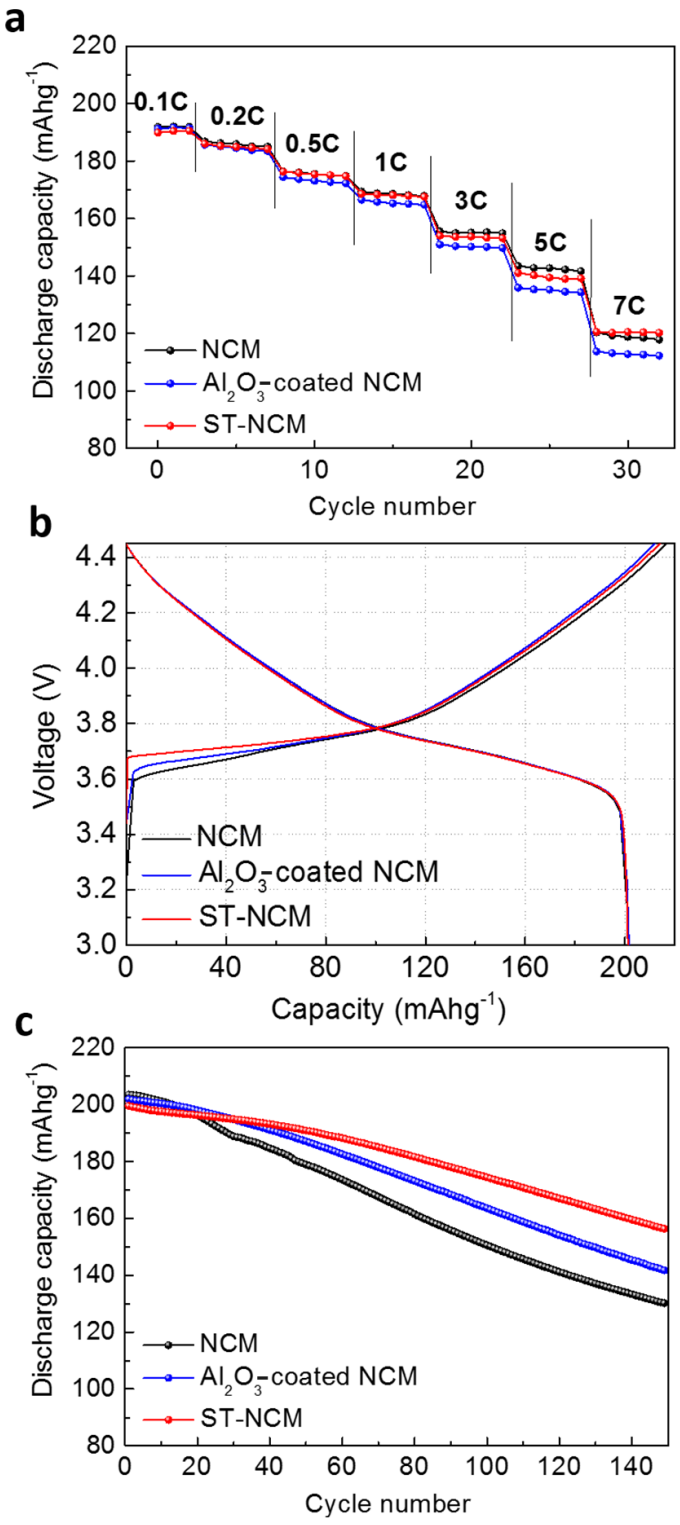

Figure 3.1.9. (a) Rate capability at RT 25ºC, (b) voltage profile at initial cycle between 3.0 – 4.45 V at 60ºC, (c) cycle performance between 3.0 – 4.45 V at 60ºC for the NCM, Al_2O_3-coated NCM, and ST-NCM samples.

Figure 3.1.10a and b show cross-sectional SEM images of the NCM and ST-NCM particles, respectively, after 150 cycles at 60 ℃ (also refer to Fig. 3.1.11). The NCM sample had extensive micro-cracks along the grains, but those cracks were significantly diminished in the ST-NCM sample. Figure 3.1.10c–h show HAADF-STEM images of the NCM and ST-NCM samples after 150 cycles. The secondary particles of the NCM sample had severe cleavages along the grain boundaries, as shown in Figure 3.1.10c. Furthermore, the primary particles of the NCM sample had many fractures (Figure 3.1.10e) in contrast to the ST-NCM sample (Figure 3.1.10f). Micro-cracks led to the penetration of the electrolyte along the grains and the reaction between the penetrating electrolyte and interior particles, accelerating structural degradation and side reactions.[11] The magnified image of Figure 3.1.10e (Figure 3.1.10g) shows that along the cracks inside the particle of the NCM, the layered phase partially changed to the spinel-like phase and rock-salt phase after cycling, and the phases were identified by inserting FFT patterns (randomly selected another STEM images also exhibit same trend in Figure 3.1.12). The phase transition in the NCM sample was deepened by the reaction between the grains and electrolyte, with many micro-cracks providing an increasing number of active sites. On the other hand, the ST-NCM sample displayed a similar phase on the surface of the grains without showing noticeable phase change compared to that before cycling (Figure 3.1.10h). Owing to the pillar effect, the migration of transition-metal ions to the lithium slab was contained, therefore the volume change (caused by phase transition) of the grains was effectively suppressed after 150 cycles. As a result, the ST-NCM sample exhibited improved electrochemical performance as it was relieved from the loss of electrical pathways.

The exothermic oxygen evolution with the structural change during heating in a fully charged state is a crucial problem for thermal stability in battery systems.[36] To evaluate the thermal stability and safety of NCM and ST-NCM as cathode materials, differential scanning calorimetry (DSC) measurements were carried out on the NCM and ST-NCM electrodes soaking in the electrolyte after charging to 4.5 V; the DSC profiles are presented in Figure 3.1.13. The main peak temperature of 264 ℃ for the ST-NCM sample is higher than the NCM sample's peak temperature of 230 ℃, indicating a significantly increased peak temperature of oxygen evolution from the lattice in ST-NCM. Furthermore, the peak area indicative of the total generated heat (resulting from the oxygen evolution) in the ST-NCM sample was 696.8 J g^{-1}, which is lower than that in the NCM sample (910.9 J g^{-1}). A correlated study using X-ray absorption spectroscopy (XAS) was performed to understand the thermal decomposition mechanism with structural change in each sample. The XAS spectral measurement is a powerful method to identify fine structure information, such as electronic states and local environments for each transition-metal ion.

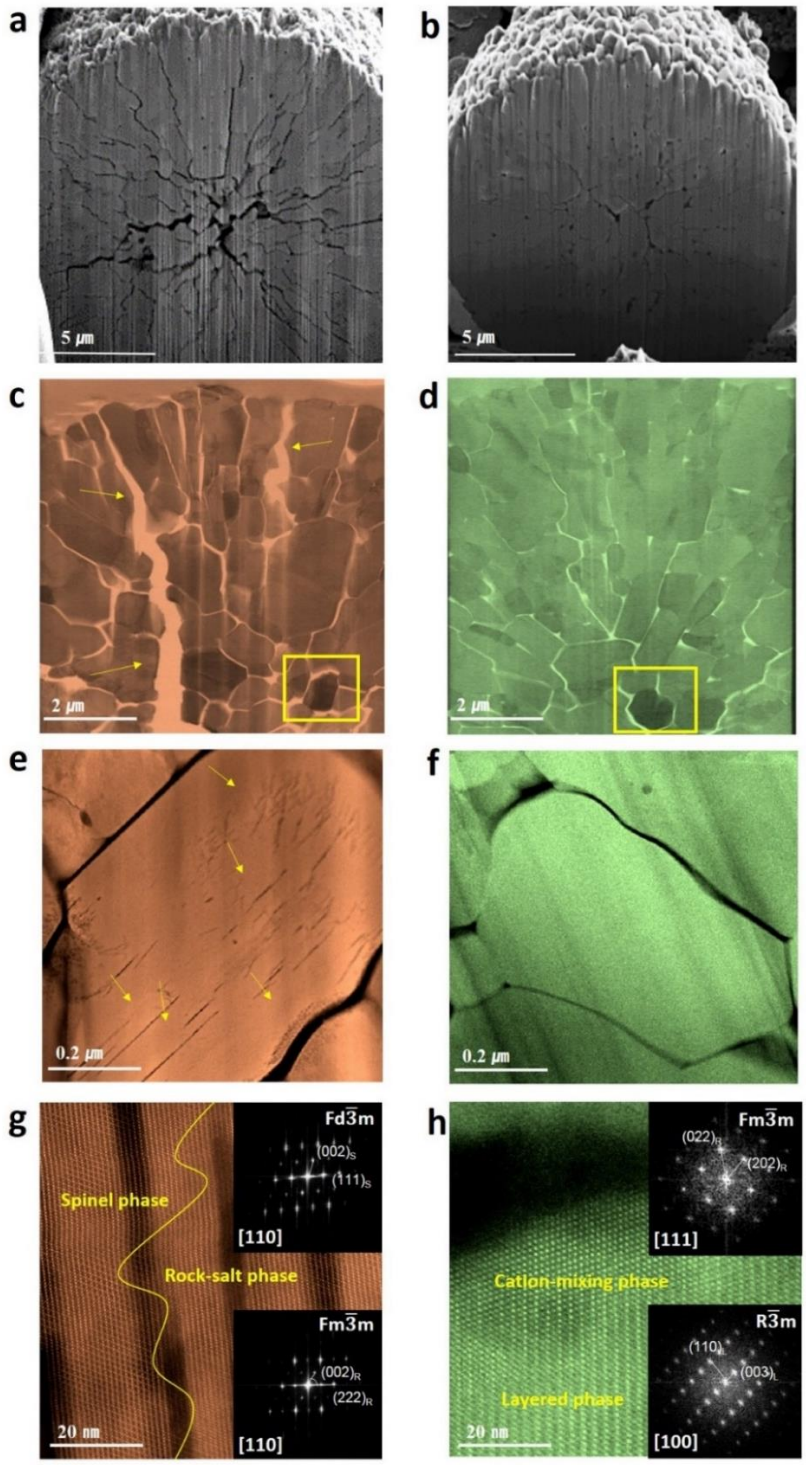

Figure 3.1.10. Particle morphology and fine structure of primary particles after 150 cycles between 3.0 and 4.45 V at 60 ℃. Cross-sectional FIB-SEM images of the (a) NCM and (b) ST-NCM particles. HAADF-STEM images of (c) NCM and (d) ST-NCM particles. Magnified STEM images of (e) NCM and (f) ST-NCM particles in the regions indicated by the yellow frames in (c) and (d), respectively. High-magnification STEM images of (g) NCM and (h) ST-NCM particles in (e) and (f), respectively. The insets of (g) and (h) show the FFT patterns.

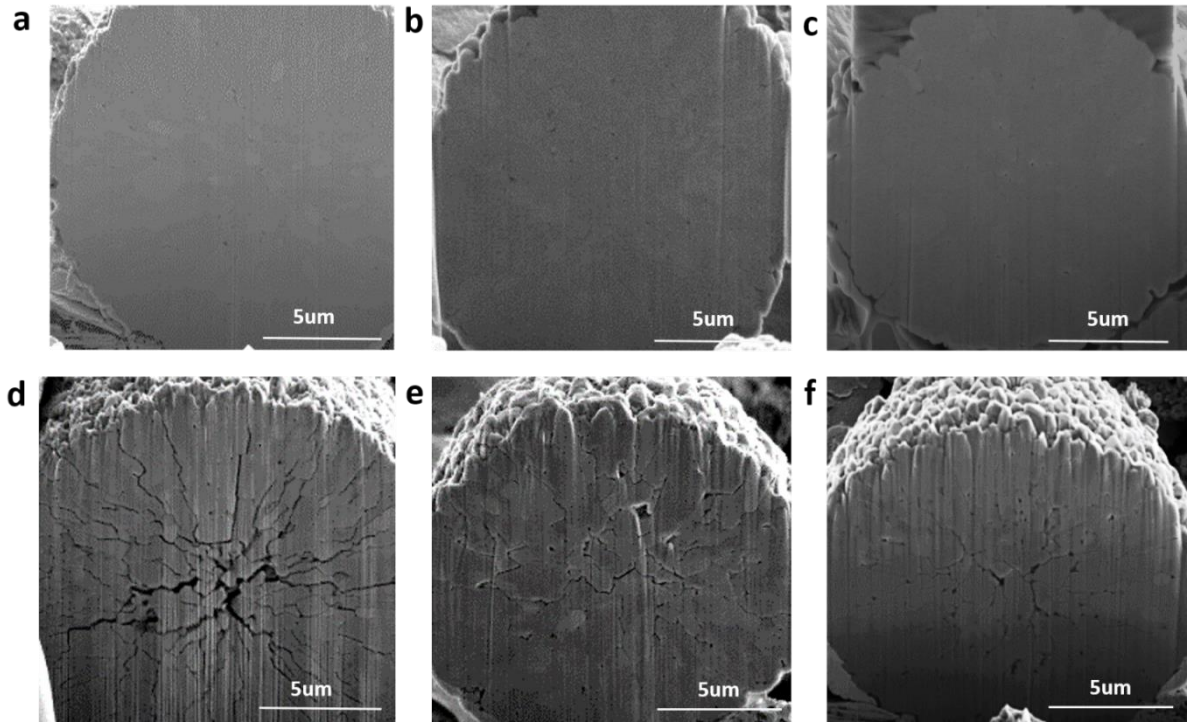

Figure 3.1.11. Cross-sectional FIB-SEM images of the NCM and ST-NCM particles before and after cycles at 60 ºC, cross-sectional SEM images of pristine particle of (a) NCM, (b) Al_2O_3-coated NCM and (c) ST-NCM, cross-sectional SEM images of (d) NCM, (e) Al_2O_3-coated NCM and (f) ST-NCM after 150 cycles between 3.0 and 4.45 V at 60 ºC.

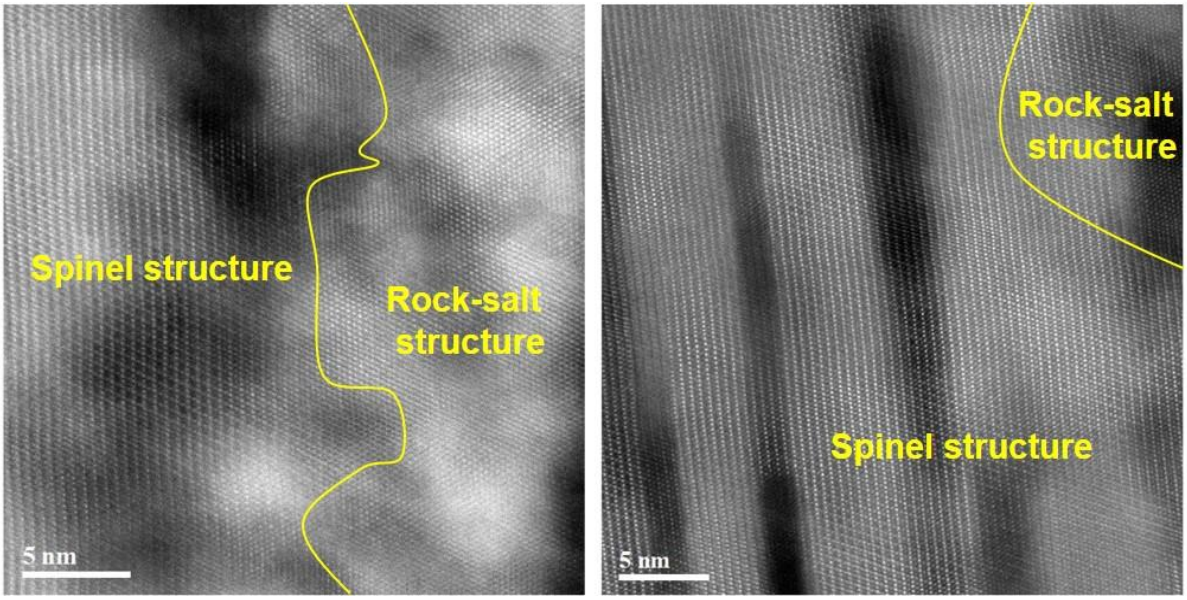

Figure 3.1.12. STEM images of NCM sample for the each primary particles after 150cycles.

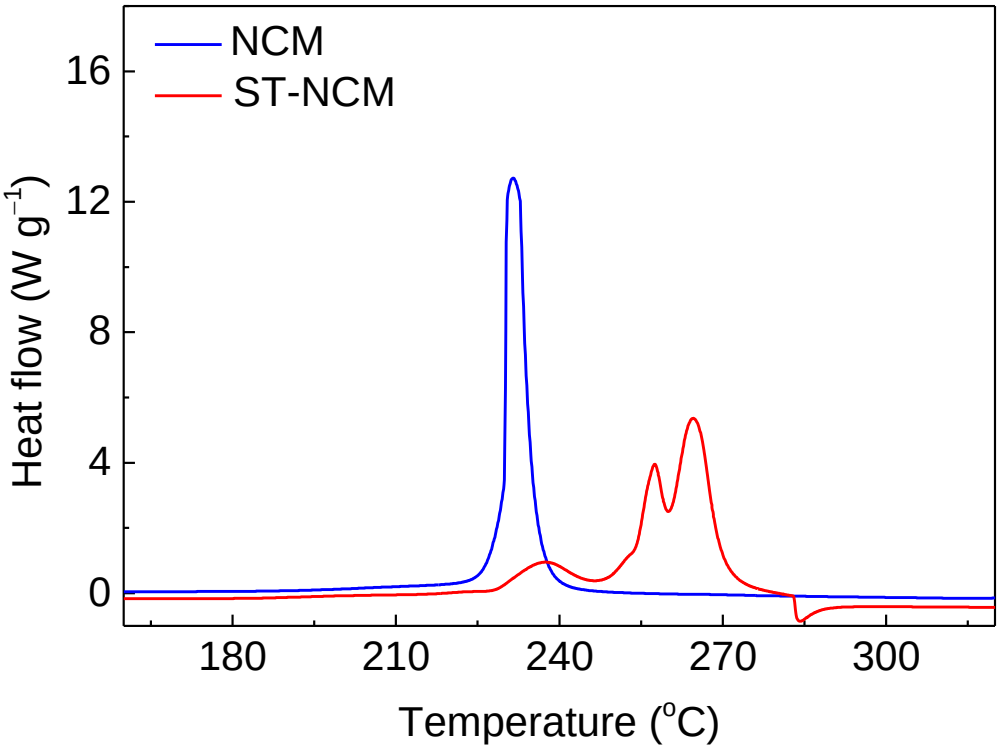

Figure 3.1.13. DSC profiles of NCM and ST-NCM after charging to 4.5 V.

Figure 3.1.14 shows the temperature dependence of Ni, Co, and Mn K-edge X-ray absorption near edge structure (XANES) spectra for the fully charged NCM and ST-NCM materials at 4.5 V during heating at temperatures up to 450 ℃. All TM K-edge XANES spectra showed characteristic peaks of a layered structure with $R\bar{3}m$ symmetry, including typical quadrupole-allowed 1s → 3d (peak A) and dipole-allowed 1s → 4p transitions with and without ligand-to-metal charge transfer (LMCT) (peaks B and C, respectively). Since the peak is associated with changes in the average oxidation state of the absorbing atoms, an *in situ* thermal XANES study can support the direct probing method for atomic-selective electronic structural characterization. The Ni and Co ions in both fully charged NCM and ST-NCM materials were oxidized to states of 4+, while the Mn ion remained in the initial 4+ state. As the temperature was increased beyond 300 ℃, the overall absorption peak features for all the transition metals in the NCM sample abruptly shifted to the lower energy region and finally showed rock-salt like characteristics, which means that the transition-metal ions were effectively reduced to Mn^{2+}, Ni^{2+}, and Co^{2+} and the phase transition to divalent TM oxides occurred. On the other hand, the ST-NCM sample showed relatively smaller peak shifts to the lower energy region compared with those of the NCM sample. All TM K-edge XANES spectra gradually evolved to show typical spinel-like peak features with shoulder peaks B_1 and B_2, not rock-salt-like features. At temperatures above 300 ℃, the Mn and Co K-edge XANES spectra corresponded to the trivalent Mn^{3+} and Co^{3+} states, respectively, while the Ni K-edge XANES spectrum showed a clear Ni^{2+} peak feature.

Figure 3.1.15 shows the corresponding radial distribution functions (RDF) of Fourier-transformed (FT) transition-metal K-edge EXAFS spectra for the charged electrodes heated to 450 ℃. Before heating, the fully charged NCM and ST-NCM samples displayed typical RDF features of the $R\bar{3}m$ layered structure, with both six-coordinated TM–O and edge-shared TM–TM bonding pairs. Below ~250 ℃, on the whole, both the charged NCM and ST-NCM samples retained the layered structure, showing a constant RDF peak feature. Above ~250 ℃, however, the RDFs of the two samples exhibited different spectral tendencies, reflecting the effect of surface treatment of primary particles with pillar layer on the thermal behavior. In the NCM sample, the RDF features of all TM elements abruptly changed to their cubic $Fm\bar{3}m$ rock-salt-like local structures (TM^{2+}–O phase) and remained constant up to 450 ℃. The cubic structural environment with divalent TM^{2+} ions led to the overall FT peak shift to higher ***r*** space region (marked with ◆), compared to those of the $R\bar{3}m$ layered structure. It should be noted that the edge-shared TM–TM in $Fm\bar{3}m$ symmetry can be differentiated from that in the $R\bar{3}m$ layered structure. On the other hand, the ST-NCM sample showed a rather different RDF dependence, compared with NCM, on the same thermal conditions.

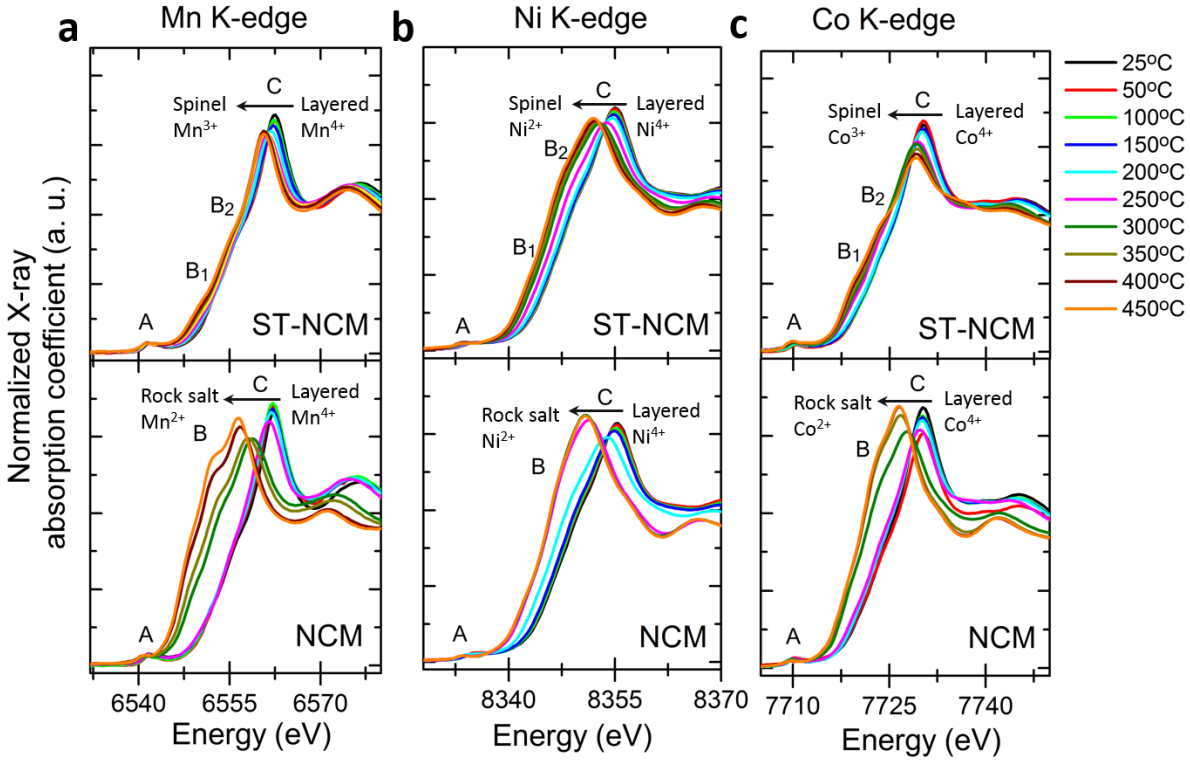

Figure 3.1.14. Normalized TM K-edge XANES spectra of the (a) Mn K-edge, (b) Ni K-edge, and (c) Co K-edge of NCM and ST-NCM as functions of heating temperature.

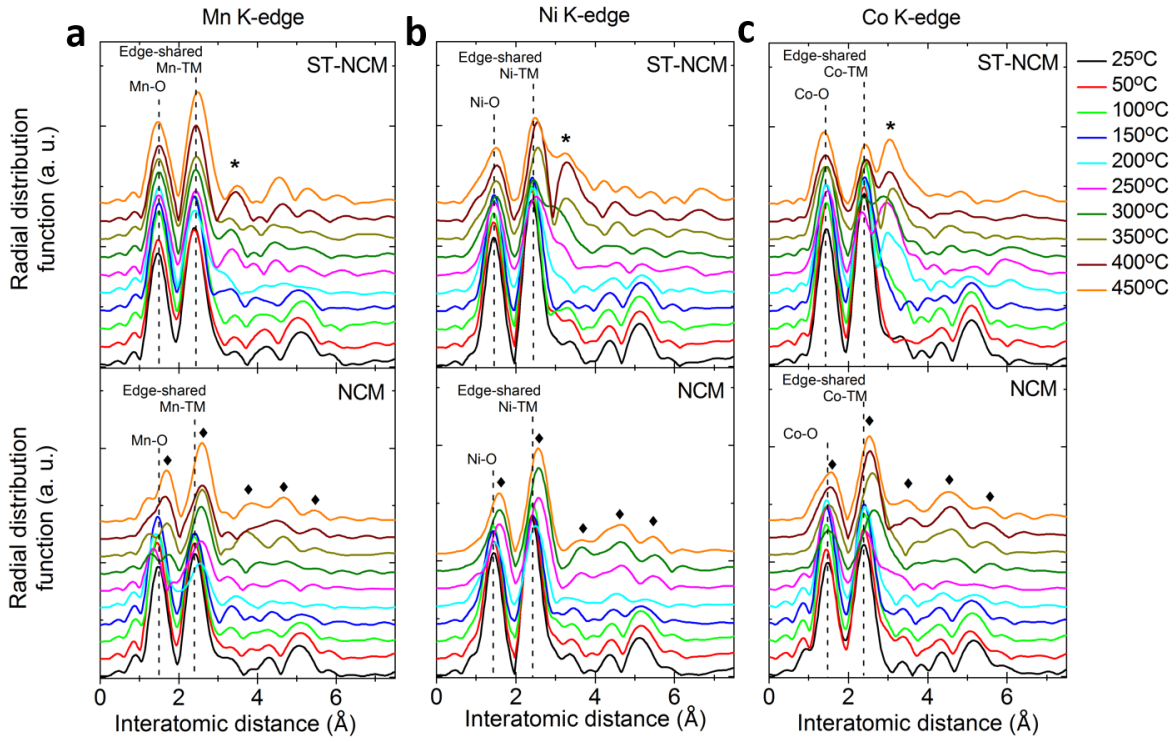

Figure 3.1.15. Radial distribution functions (RDF) for Fourier-transformed k^3-weighted TM K-edge EXAFS spectra of the (a) Mn K-edge, (b) Ni K-edge, and (c) Co K-edge of NCM and ST-NCM as functions of heating temperature.

Above ~250 ℃, the RDFs for all of the TM ions developed features of the cubic $Fd\bar{3}m$ spinel-like phase with the coexistence of edge-shared and corner-shared octahedral sites. This means that the pillar layer on the surface of primary particle could lessen the thermal shock to the core-charged NCM material. Under the thermally-mitigated environment, the Co and Ni ions in the layer would have the chance to easily migrate to the empty interstitial sites between the edge-shared octahedral slabs, instead of participating in the direct phase transition to cubic $Fm\bar{3}m$ rock salt. The atomic rearrangement resulted in a new generation of corner-shared TM–TM interactions (marked by * in Figure 3.1.15) and then the formation of short-range order of the spinel-like phase. Based on the XANES result of the Ni^{2+}, Co^{3+}, and Mn^{3+} states at the higher temperatures, the locally thermal-driving phase was estimated to be a mix of the normal spinels of $Ni^{2+}Co^{3+}{}_2O_4$ and $Ni^{2+}Mn^{3+}{}_2O_4$.

As shown by the results, a thermally driven structural degradation mechanism can be suggested for the NCM and ST-NCM samples, based on the assumption that the atomic-selective thermal reductions of the TM elements during heating gave rise to the oxygen release from the lattice. The reaction can be classified as follows:

NCM sample: $3(NCM)^{4+}O_2$ (layered) → $3(NCM)^{2+}O$ (rock-salt like) + $\frac{3}{2}O_2\uparrow$

ST-NCM sample: $3(NCM)^{4+}O_2$ (layered) → $(Ni^{2+}Co^{3+}Mn^{3+})_3O_4$ (spinel-like) + $O_2\uparrow$

The structural change accompanied the oxygen evolution from the lattice, and the amount of the evolved oxygen for the structural transformation from the layered to rock-salt phase was higher than that for the transformation from the layered to spinel phase. This result is attained by the stabilized structure with pillars on the surface of grains. In addition, the stronger Mn–O bonding by Mn^{4+} in the ST-NCM primary particle's surface restrained the release of oxygen, and therefore the ST-NCM sample showed lower total generated heat in the highly delithiated state.

Table 3.1.1. Rietveld refinement results of the (a) NCM and (b) ST-NCM samples.

a

Goodness-of-fit parameters		**Lattice parameter**	**c/a : 4.9585**
Reduced χ^2	**1.886**	**a**	2.8677
Total R_{wp}[a]	**5.46**	**c**	14.2196

Fractional coordinates					**Space group**	**R-3m**
Atom	**Site**	**x**	**y**	**z**	**Occupancy**	
Li1	3b	0.0000	0.0000	0.0000	0.9493	
Li2	3a	0.0000	0.0000	0.5000	**0.0553**	
Ni1	3a	0.0000	0.0000	0.5000	0.5960	
Co1	3a	0.0000	0.0000	0.5000	0.2089	
Mn1	3a	0.0000	0.0000	0.5000	0.2081	
O1	6c	0.0000	0.0000	0.2416	0.9823	
Ni2	3b	0.0000	0.0000	0.0000	0.0561	

b

Goodness-of-fit parameters		**Lattice parameter**	**c/a : 4.9627**
Reduced χ^2	**1.215**	**a**	2.8673
Total R_{wp}[a]	**4.48**	**c**	14.2295

Fractional coordinates					**Space group**	**R-3m**
Atom	**Site**	**x**	**y**	**z**	**Occupancy**	
Li1	3b	0.0000	0.0000	0.0000	0.9736	
Li2	3a	0.0000	0.0000	0.5000	**0.0854**	
Ni1	3a	0.0000	0.0000	0.5000	0.5577	
Co1	3a	0.0000	0.0000	0.5000	0.1954	
Mn1	3a	0.0000	0.0000	0.5000	0.1968	
O1	6c	0.0000	0.0000	0.2416	0.9186	
Ni2	3b	0.0000	0.0000	0.0000	0.0318	

Table 3.1.2. Information of the integrated L_3/L_2 ratio of the Mn L-edge on the Region 1 and 2.

	I (L_3)/I (L_2) ratio	**Oxidation state of Mn**
NCM (region1)	3.02	~2.67+
NCM (region2)	1.98	4+
ST-NCM (region1)	1.97	4+
ST-NCM (region2)	2.01	4+

3.1.4 Conclusion

In conclusion, the $LiNi_{0.6}Co_{0.2}Mn_{0.2}O_2$ cathode material with surface-treated primary particles (ST-NCM) was prepared using the solution with completely ionized lithium and cobalt sources. The ST-NCM primary particles' surface, which consisted of a cation-mixing layer as a pillar layer, effectively improved the structural stability and electrochemical performance by suppressing the microcracks in the particles and grains during cycling. Moreover, the ST-NCM evidently prevented the oxygen evolution from phase transition at elevated temperature by suppressing the structural degradation and stronger Mn–O bonding. This concept of coating for the primary particles can be applied as a new strategy for surface modification to realize improvements in both electrochemical properties and thermal stability.

3.2 Generation of Nano glue-like layer as bridge of grains for stable Ni-rich cathode materials in lithium ion batteries

3.2.1 Introduction

The demand for high-performance lithium-ion batteries (LIB) in terms of energy density and life time have increased with an expansion in their applications from mobile devices to electric vehicles (EVs) and energy storage systems (EESs).[37] Thus, cathode materials should fulfil important criteria such as high energy density, high power density, long cycle life, and thermal stability in a wide range of temperatures. Ni-rich cathode materials, such as $LiNi_xCo_{1-x-y}Al_yO_2$ ($x \geq 0.8$, $y \leq 0.05$), $LiNi_xCo_{1-x-y}Mn_yO_2$ ($0.6 \leq x \leq 0.9$, $0.1 \leq y \leq 0.2$) have garnered attention for their application in advanced LIBs due to the high specific capacity and economical merits of the materials.[38]

The higher Ni-content in the structure leads to higher specific capacity, but as Ni-content increases, the material exhibits poor cycling performance and thermal instability caused by the acceleration of cation mixing and surface side reaction, especially at elevated temperature.[2, 8, 39] In this regards, several researchers have undertaken efforts to modify the Ni-rich material by using surface coatings (metal oxide, metal phosphates, etc.), introducing a concentration-gradient of a transition metal, and developing a core-shell structure.[27e, 40] Nevertheless, Ni-rich cathodes still have several problems at elevated temperatures caused by morphological degradation.

Ni-rich cathode materials show the morphology of secondary particles, which consists of single crystals with an average size <0.5 μm. Accordingly, the secondary particles contain many grain boundaries and voids that are distinct from $LiCoO_2$ single particles.[41] Thus, Ni-rich materials tend to be pulverized upon cycling because of anisotropic volume-changes in each single crystal having different crystal orientations in a secondary particle.[11] This morphological degradation causes a loss in electronic conductivity and exposes new active sites, resulting in continuous performance degradation in terms of rate capability, cyclability, and structural stability upon cycling. Moreover, the electrochemical deterioration of Ni-rich materials also gets worse at temperatures >45 ℃.

Our group has reported the possibility of an internal coating in a secondary particle by using a fully dissolved precursor solution as a coating source.[42] Subsequently, we found that a stable active material coating on spinel cathode materials using a solution-based process could effectively enhance their electrochemical performance without sacrificing their high capacity. We have demonstrated several advantages of the coating such as epitaxial growth of coating layer, high coating coverage, capacity contribution and enabling primary particle coating in a secondary particle, metal oxidation state tuning, and surface structure tuning.[43] Recently, we have applied the

concept of coating to a layered $LiNi_{0.6}Co_{0.2}Mn_{0.2}O_2$ cathode.[44] We successfully introduced stable Li_xCoO_2 with a layered structure on both the inside and outside of secondary particles, and the cathode exhibited improved electrochemical performance. However, the capacity retention of the surface modified sample at 60 ℃ was 80% for 150 cycles, indicating a large difference in capacity retention between 60 ℃ and 25 ℃.

Herein, we demonstrate a simple coating to introduce a glue-nano-filler layer (denotes as G-layer) between the grains of the $LiNi_{0.8}Co_{0.15}Al_{0.05}O_2$ (NCA) cathode materials, which consists of middle-temperature Li_xCoO_2 (MT-LCO, $x < 1$) with a spinel-like structure. By applying the coating, we accomplished outstanding capacity retention of 87% after 300 cycles at 60 ℃ without using any electrolyte additives, even when the Ni content of this material was as high as 80%. We investigate the role of the coating layer using the combination of an electron microscope, powder characterization, and electrochemical characterization along with a computational method.

3.2.2 Experimental method

Preparation of pristine sample. To prepare $Ni_{0.89}Co_{0.11}(OH)_2$, a typical co-precipitation method was implemented.[45] The stoichiometric amount of Al acetate was dissolved in ethanol. The $Ni_{0.89}Co_{0.11}(OH)_2$ precursor powder was poured into a separately prepared aluminium solution and mixed vigorously for 1 h, and dried at 80 ℃ in a vacuum oven. The dried powder was mixed with $LiOH \cdot H_2O$ (molar ratio 1:1.03) and annealed at 450 ℃ for 5 h, followed by heating at 750 ℃ for 18 h under oxygen gas blowing. Finally, the $LiNi_{0.8}Co_{0.15}Al_{0.05}O_2$ (denoted by NCA) powders were obtained.

Fabrication of glue-like filler layer. 100 g of the NCA powders were added to a coating solution which includes dissolved lithium and cobalt acetate in ethanol. The amounts of lithium were decided by the amount of residual lithium in the NCA cathode materials. The amount of coating material (MT-LCO) was optimized to 1 wt% of the NCA powder. The solvent was evaporated at 60 ℃ with stirring, and the powder was calcined at 600 ℃ for 4 h.

Material characterization. The morphology of particles and cross-sectional images were obtained by using focused ion beam (FIB)-scanning electron microscopy (SEM) technique (FEI Helios Nano Lab 450). Additionally, the samples were thinned by a low-energy Ar-ion milling system (Fischione Model 1040 Nanomill). The HAADF-STEM images were taken using a probe-side aberration corrected TEM (JEOL JEM-2100F). The pellet density (PD) of the cathode powder was measured by preparing pellets with 13 mm diameter 2.5 g powder under 25 MPa (253.93 kgf cm^{-2}) for 30 s.

Electrochemical evaluation. The electrochemical performance was evaluated by a coin-type 2032R lithium half-cell. The cathode electrode was prepared by mixing a typical slurry with cathode materials powder, carbon black and PVDF binder with a mass ratio of 92:4:4 in *N*-methyl-2-pyrrolidinone. The loading level of cathode material was ~8.0 mg cm^{-2} (Std. Dev 0.1). The cells were assembled in an argon-filled glove box with a 2032R type cell kit. The electrolyte for the half-cells was 1.15 M $LiPF_6$ with ethylene carbonate–dimethylene carbonate–diethylene carbonate (30:40:30 vol%) (Panax Etec). The galvanostatic electrochemical impedance spectroscopy (GS-EIS) was performed by two channels of multichannel potentiostats (BioLogic/VSP-300). Channel 1 provided a galvanostatic signal (a biased current) to the cells, and channel 2 applied a series of small AC waves on the galvanostatic signal of channel 1, resulting in potential waves to calculate impedances.

MD simulation. To investigate the effect of the voids on the interaction between NCA particles, stoichiometric NCA particles with spherical shape were modelled with a radius of 25 Å and 50 Å. The flat (001) surfaces were introduced to the particles, which were terminated with O

and Li (Inset of Figure 3.2.12a). For the interfacial study of NCA and MT-LCO, the near coincidence site lattice (NCSL) theory[46] was used to minimize the strain energy caused by lattice mismatch. We constructed two systems of slab model (i.e. NCA/NCA or NCA/MT-LCO) with the percentage of lattice misfit less than 2% (Fig. S9a). The thickness of each slab was approximately 30 Å, and they were separated from each other by 5 Å in the simulation box, where the height was set to be 200 Å (Fig. S9b and d). Each slab was made of cross attachments from (001), (104), (101), or (110) NCA surfaces and (001), (101), (111) or (113) MT-LCO surfaces. Each slab of the rectangular unit cell was cleaved from the bulk system in such a way that the surface became stoichiometric and electroneutral; several types of terminations of surfaces were obtained (Fig. S9c). We mainly classified slabs by their polarity, i.e. polar surfaces included NCA(001), NCA(101), MT-LCO(113), and MT-LCO(111) and nonpolar surfaces included NCA(104), NCA(110), MT-LCO(001), and MT-LCO(101). Polar surface was defined to have a dipole due to atomic arrangement along the z-axis. When interfaces were constructed, possible combinations of surface termination and 90° rotation relative to each surface were taken into account. For NCA models (Fig. S9c), NCA (001) slab was made of O and Li terminations on top and bottom surfaces, respectively, and thus its surface exhibited relatively large local dipole inducing high chemical reactivity.[47] On the other hand, NCA (104) slab has no dipole with terminations of Li, O, and Ni_{5c} (i.e. 5-coordinated) at both surfaces. NCA (101) slab, which looks like a tilted structure of NCA (104) slab, was made of Li and O terminations inducing a local dipole. NCA (110) slab was made of Li, Ni_{4c} (i.e. 4-coordinated), and O terminations at both surfaces, so a local dipole was not induced. For MT-LCO (Fig. S9d), MT-LCO (001) slab was made of Li, Co_{5c}, and O terminations and each termination had the same surface structure if rotated by 90°. MT-LCO (101) slab had two different terminations, where the top one (i.e. $LiCo_{4c}O$-1) was rectangular-centred Li termination while the bottom one (i.e. $LiCo_{4c}O$-2) was rectangular-primitive Li termination. Although these two terminations were different, there were no surface dipoles along the z-axis because of their identical stoichiometries at surfaces. MT-LCO (113) slab had two different terminations with $LiCo_{3c}$ and O, which induced a local dipole. MT-LCO (111) slab, which was particularly very unstable to contain a local dipole, was constructed by distributing terminated oxygen atoms into top and bottom surfaces to minimize dipole moment. Table S3 presents the structural properties of each surface model. All-atom molecular dynamics simulations were performed using the Large-scale Atomic/Molecular Massively Parallel Simulator (LAMMPS) package.[48] The calculations were based on the Born model of ionic solids which have been commonly used for metal oxides. In this model, the interionic interactions were described by long-range Coulombic interactions and short-range Buckingham potential representing electron–electron repulsion and van der Waals forces as follows:

$$E_{ij} = A_{ij}e^{-r_{ij}/\rho_{ij}} - \frac{C_{ij}}{{r_{ij}}^6} + \frac{q_i q_j}{r_{ij}}$$

where A_{ij}, ρ_{ij}, and C_{ij} are empirical pair potential parameters, r_{ij} is the interionic separation, and q_i and q_j are the charge of ion i and j, respectively. Each ion was treated as a non-polarizable formal charge. The potential parameters used in this study for NCA and MT-LCO are listed in Table S4. The empirical parameters of Li-O, Ni-O, Co-O, and O-O were taken from the literature.[49] A cutoff radius of 12.0 Å was used for short-range interactions and the particle–particle particle–mesh (PPPM) method[50] was incorporated for the electrostatic interactions. The velocity Verlet algorithm was used with a timestep of 2 fs. Periodic boundary conditions were implemented. The temperature and pressure of the system were controlled by a Nose-Hoover thermostat with a damping parameter of 0.1 ps and a Nose-Hoover barostat with a damping parameter of 1 ps, respectively. All simulations were conducted under the $NP_{xx}P_{yy}L_{zz}T$ ensemble, where P_{xx} and P_{yy} were set to 1 atm and L_{zz} was fixed. MD simulations of model systems were carried out initially at the temperature of 1300 K for 400 ps. After that, the systems were cooled down to near 0 K at a cooling rate of 1 K/ps. Additional 200 ps of simulations near 0 K were performed to optimize the structures. This approach was previously used to make the surfaces at the interface come closer and overpass energy barriers to find the global minimum of the potential energy surface.[51] To compare the relative binding strength between NCA/NCA interface and NCA/MT-LCO interface, binding energy per unit area between the two slabs was calculated with the final configuration of the simulation, which is described by the equation below:

$$E_{binding} = \frac{E_{interface} - E_{slab1} - E_{slab2}}{A_{interface}}$$

where $E_{interface}$ is the energy of the total system, E_{slab1} and E_{slab2} are energies of electroneutrally cleaved top and bottom slabs at the interface, and $A_{interface}$ is the area of the interface.

3.2.3 Results and Discussion

The coating solution was prepared by completely ionized lithium and cobalt acetate in ethanol solution (Figure. 3.2.1). We have reported this simple method in our previous work (also, see Methods).[43a, 44] Ionized coating sources infiltrated into the secondary particles through the gap between each primary particles, enabling the coating inside and outside of secondary particles (Figure 3.2.2). In contrast to the process followed in previous work (calcination at 800 ℃ for 4 h) this low firing temperature of 600 ℃ leads to the formation of a spinel-like phase MT-LCO between grains (denoted as G-layer).[52]

There are several important parameters such as powder pH and moisture content which must be considered in the research of Ni-rich cathode material for Li-ion batteries. The water content and pH of the powder associated with residual lithium should be restricted within 250 ppm and <11.7, respectively, or it leads to safety issues in the battery and failures in battery manufacturing processes such as accelerated HF formation and slurry gelation, respectively.[39] In forming the G-layer, as presented in Table 3.2.1, the residual lithium compounds could be consumed as lithium precursors to the coating process because MT-LCO has additional lithium sites of 8a and 16d.

Figure 3.2.3a shows the aberration-corrected high annular dark-field scanning transmission electron microscopy (STEM) image of pristine sample along the [100] zone axis. Each grain of the pristine sample showed a typical layered structure with a space group of $R\bar{3}m$ with lattice fringes of (003) and (012) plane corresponding to the d-spacing of 4.7 Å and 2.3 Å, respectively. Since the Ni-rich cathode consists of anisotropically oriented primary particles (grain), the sample shows several voids and gaps at the nanometer-scale between grains, as shown Fig. 3.2.3b and c. For the G-layer sample, the STEM image shows the atomic arrangement of the coating layer along the $[011]_{cubic}$ zone axis (Figure 3.2.3d). This could be matched with the space group of $Fd\bar{3}m$, which consisted of Co and Li occupying 16d and 16c octahedral sites, respectively.[53] At the calcination temperature of 600 ℃, Li_xCoO_2 called middle-temperature Li_xCoO_2 (MT-LCO, $x < 1$) could be formed with a spinel-like structure.[52, 54] As a result, voids with a size >10 nm and tiny gaps of 2–10 nm could be filled by MT-LCO on the coating process. The thin coating layers of <10 nm between the primary particles in a secondary particle were confirmed by HR-TEM images as shown in Fig. 3.2.3e and f (Figure 3.2.4 and 3.2.5).

The pellet density (PD) of the cathode powder was measured by preparing pellets with 13 mm diameter, 2.5 g powder under 25 Mpa (253.93 kgf cm^{-2}) for 30 s. The PD can be a criterion for the achievable electrode density using the powder, and so it can be correlated with volumetric energy density; commercial Ni-based cathodes have ~3.3 g cm^{-3}.[55] The pellet density of the G-layer was increased to 3.41 g cc^{-1}, as against the pristine sample with 3.32 g cc^{-1}. As shown in Fig.

2g and h, the pristine sample was pulverized after the PD test, in contrast to the G-layer sample. This result indicates enhanced mechanical strength of secondary particles caused by the formation of glue-layer between grains, which results in an extended contact area among the primary particles.

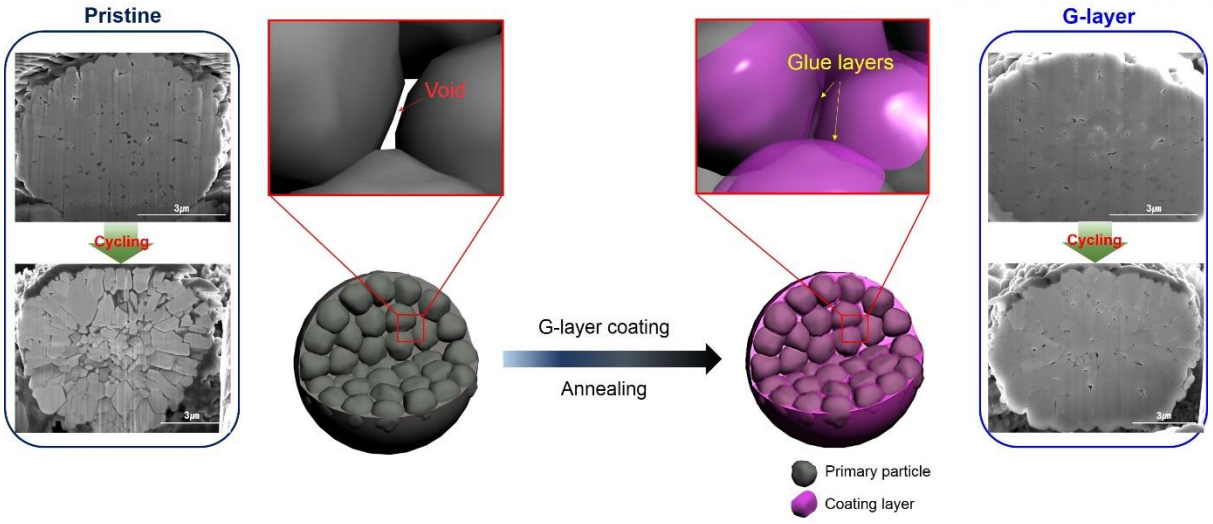

Figure 3.2.1. Schematic diagram of glue-layer fabrication mechanism. The scheme shows a formation of glue layer (purple) in a NCA secondary particle (gray) during the coating processes. The cross-sectional SEM images of the pristine sample show a severe morphological degradation during the electrochemical distinct from that of G-layer sample. The key roles of the glue layer on the electrochemical performance of the materials will be discussed in detail.

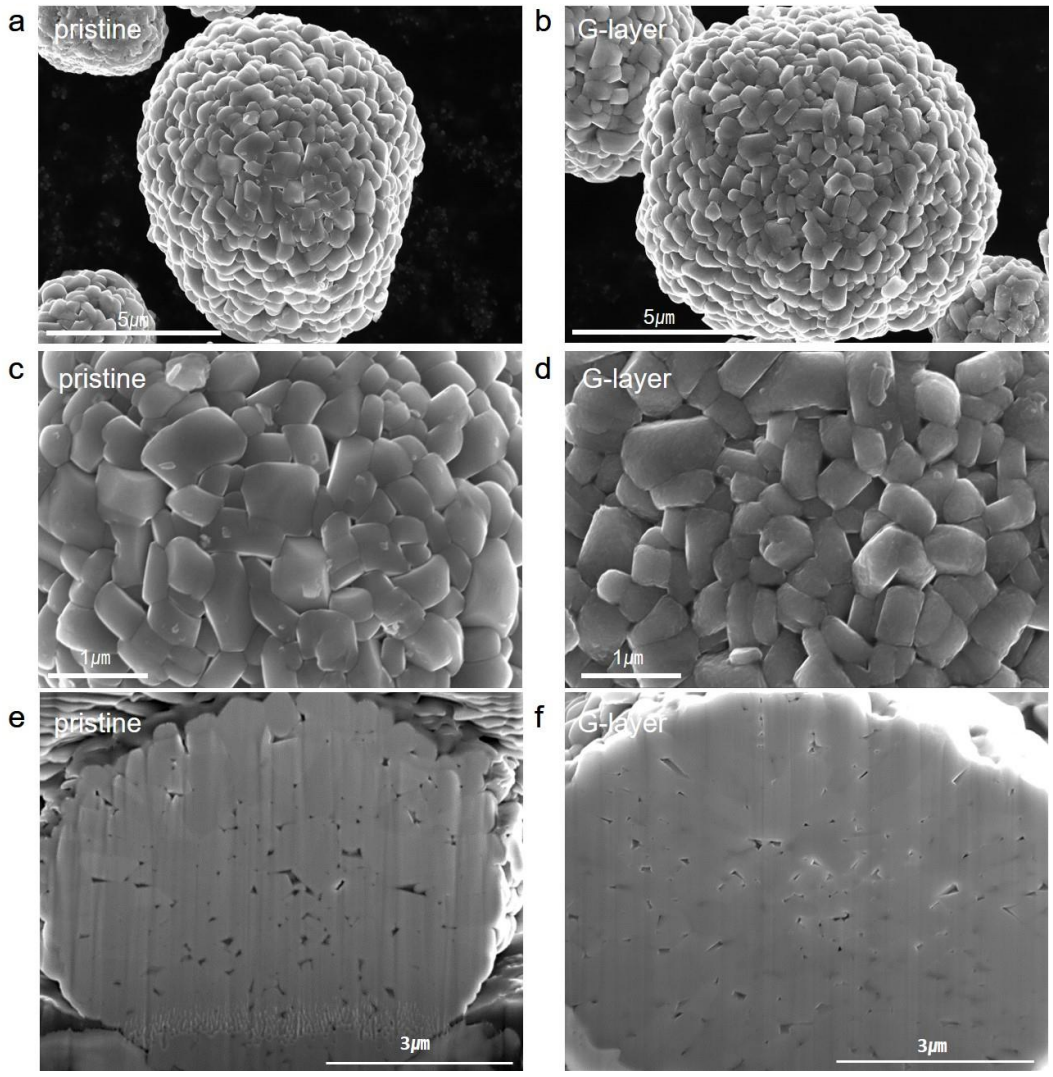

Figure 3.2.2. SEM images for surface morphology of (a, c) Pristine and (b, d) G-layer samples, Cross-sectional images of (e) Pristine and (f) G-layer samples

Table 3.2.1. Comparison of physical properties of pristine and G-layer samples after synthesis. Increasing particle size and decreasing specific surface area by primary particle coating is shown this table.

Physical properties		**Pristine**	**G-layer**
Particle Size Distribution [㎛]	**D_{50}**	7.55	8.25
	D_{min}	4.76	5.64
	D_{max}	13.12	15.25
Tap Density [g/cc]		2.47	2.46
Pellet Density [g/cc]		3.34	3.41
BET Surface Area [m^2/g]		0.43	0.16
Moisture Content [ppm]		1019	212
pH		12	11.5

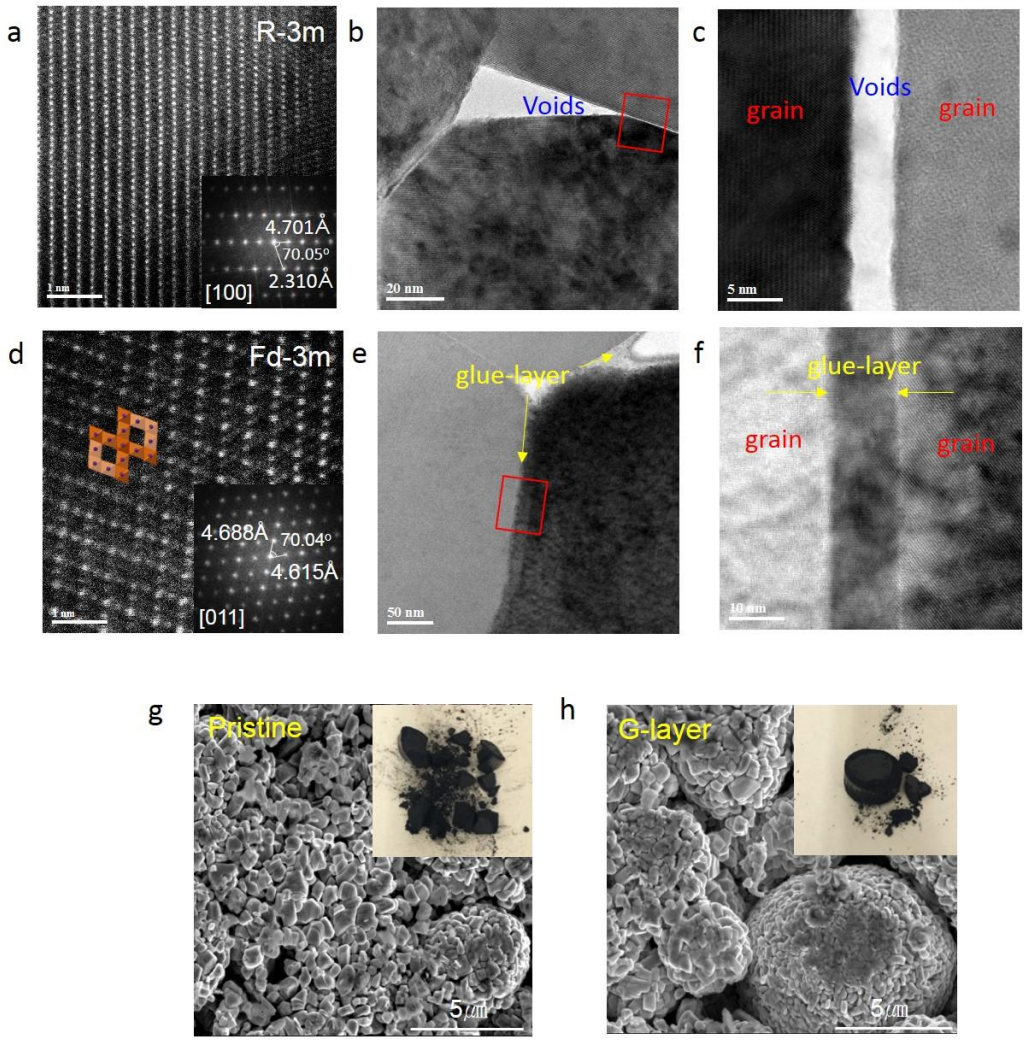

Figure 3.2.3. Photographs and SEM images of pristine and G-layer powders after pellet density test. STEM images of grains of (**a**) Pristine and (**d**) G-layer samples. Fast fourier transform (FFT) image of inserted in (a) and (d), respectively. The HR-TEM images between grains (**b, c**) Pristine ((**c**) Expanded image of red rectangle in (b)) and (**e, f**) G-layer samples ((**f**) Expanded image of red rectangle in (e)). The pellets were collected after pressing with the pressure of 25 MPa (=254.93 kgf cm^{-2}) for 30 sec. Top view SEM images; (**g**) Pristine sample (**h**) G-layer sample. The pellets of the powder were shown in the insert of (**g and h**), respectively.

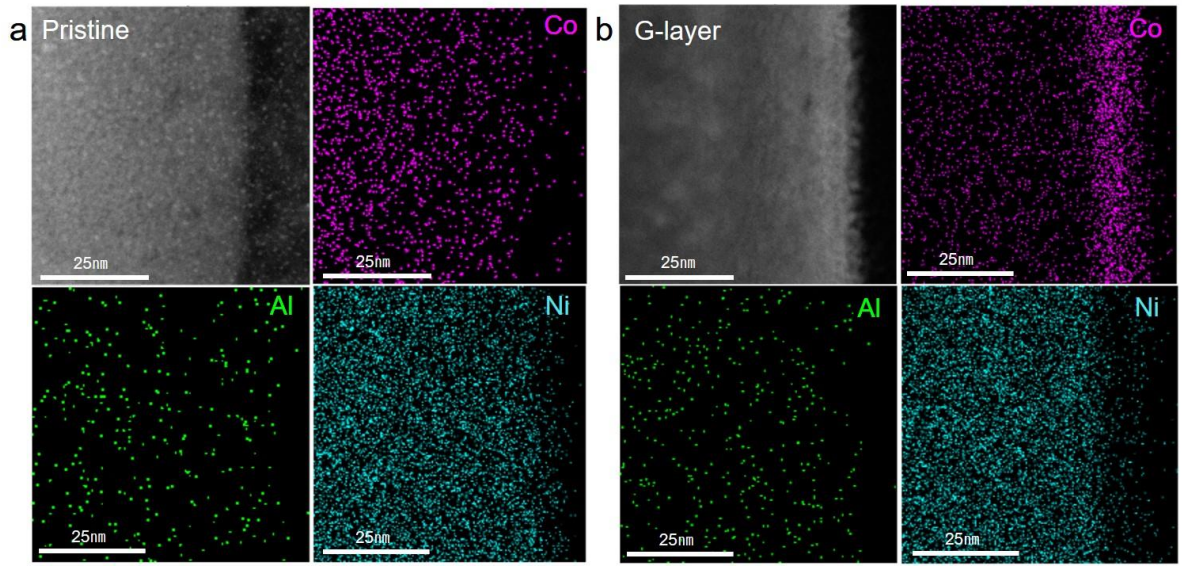

Figure 3.2.4. STEM images and EDS mapping results of (a) pristine and (b) G-layer samples

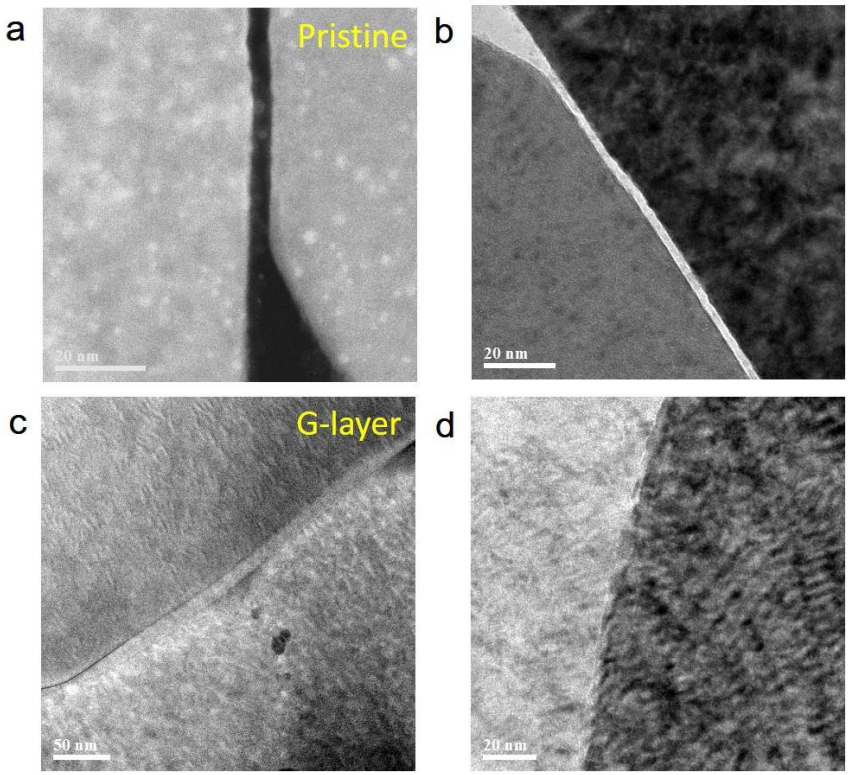

Figure 3.2.5. STEM images for grain boundaries of (a, b) Pristine and (c, d) G-layer samples

To directly compare the capacity retention of the sample between 25 ℃ and 60 ℃, the discharge capacities were normalized by the first discharge capacity (Figure 3.2.6a). Note that both the first discharge capacities of the pristine and G-layer samples were 200 mAh g^{-1}, with coulombic efficiency of 94% (Figure 3.2.7). No decrease in capacity after coating suggests minimal reaction between the pristine and coating material at 600 ℃. In general, a higher coating temperature resulted in the diffusion of the coating material into the pristine sample, which accompanies a decreased discharge capacity. [40d] One of the striking features of the G-layer sample was that the capacity retention curve at 60 ℃ was almost superimposed on that at 25 ℃ in 300 cycles. (Figure 3.2.6a). It is known that capacity degradation of cathode materials becomes more severe as temperature increases due to the accelerated surface side reactions with the electrolytes and structural changes from the layered to rock-salt NiO phases. This outstanding cyclability of the Ni-rich cathode at elevated temperatures has not been reported yet.[14, 40c, 56] For instance, the $Ni_3(PO_4)_2$ coating on $LiNi_{0.80}Co_{0.15}Al_{0.05}O_2$ to improve cycle life at high temperature was reported by Lee *et al*.[57]. The capacity retention of the $Ni_3(PO_4)_2$ coated sample was 75% after 100 cycles at 55 ℃. According to our previous research,[45] the difference in capacity retentions of the $LiNi_{0.81}Co_{0.1}Al_{0.09}O_2$ cathode after 200 cycles at 25 ℃ and 60 ℃ was ~20%. In comparison with previous works, the G-layer sample demonstrated good performance at 25 ℃ and 60 ℃ even after 300 cycles. In the cycling test (Figure 3.2.6b), the operating voltages of the pristine sample were significantly changed, which is indicative of an increase in internal resistances during the charge and discharge process. On the other hand, those of the G-layer sample were almost unchanged. This new coating method was further proved by another high Ni-rich cathode material, $LiNi_{0.8}Co_{0.1}Mn_{0.1}O_2$ (NCM811), which showed substantially improved capacity retention of the coated sample relative to the pristine NCM sample (Figure 3.2.8).

Another important issue with Ni-rich cathodes is poor structural stability in the fully charged state (fully delithiated state) because of their unstable layered structure of vacant lithium slabs.[58] The structural instability leads to dissolution of transition metal ions into electrolytes and the formation of a phase transition, especially at elevated temperatures, which results in safety issues.[59] Figure 3.2.6c shows the discharge curves of the samples before and after storage at 60 ℃ for 14 weeks in a fully charged state (4.3 V). The pristine sample displayed 21.85% deteriorated discharge capacity with 153 mAh g^{-1}. On the other hand, the G-layer sample sustained the discharge capacity of 187 mAh g^{-1}, showing 94% capacity retention. We believe that MT-LCO filler layers provide structural stability to each grain even after delithiation.

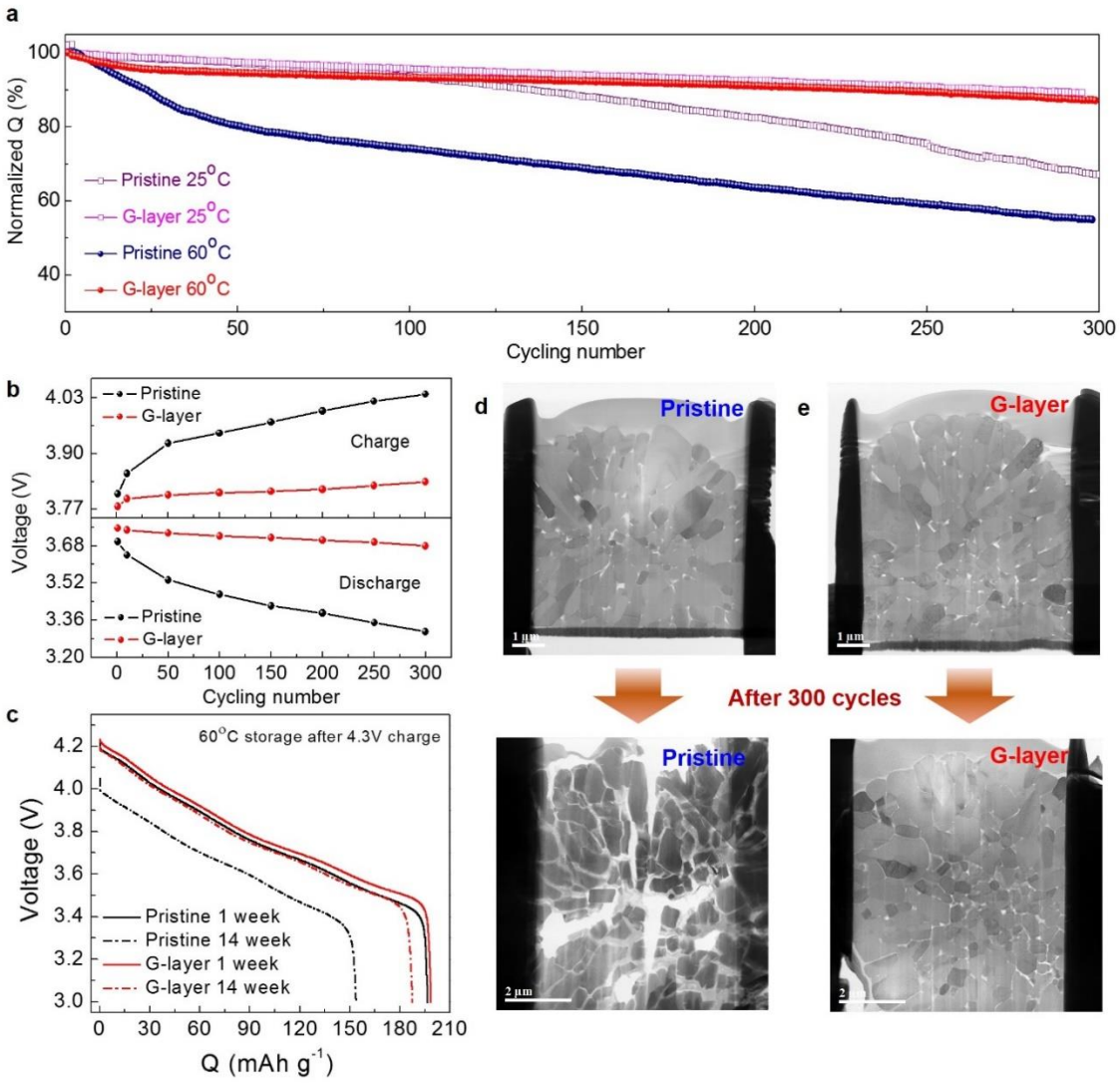

Figure 3.2.6. **Electrochemical evaluation at high temperature and STEM/EDXS images after 300 cycles of the samples.** (**a**) Cycle performance of the pristine and G-layer samples between 3.0 and 4.3 V at 25, 60 ℃ (charge rate: 0.5 C; discharge rate: 1 C). The voltage profiles are available in supplementary figure 4. (**b**) Voltage versus cycle number in cycling at high temperature for pristine and G-layer samples. (**c**) Voltage profile of discharge for storage test at high temperature. The cells are stored at 60 ºC for 14 weeks after 4.3V charge (Q=Discharge capacity). STEM images of the cross-sectioned particle; (**d**) Pristine sample before and after cycle. (**e**) G-layer sample before and after cycle.

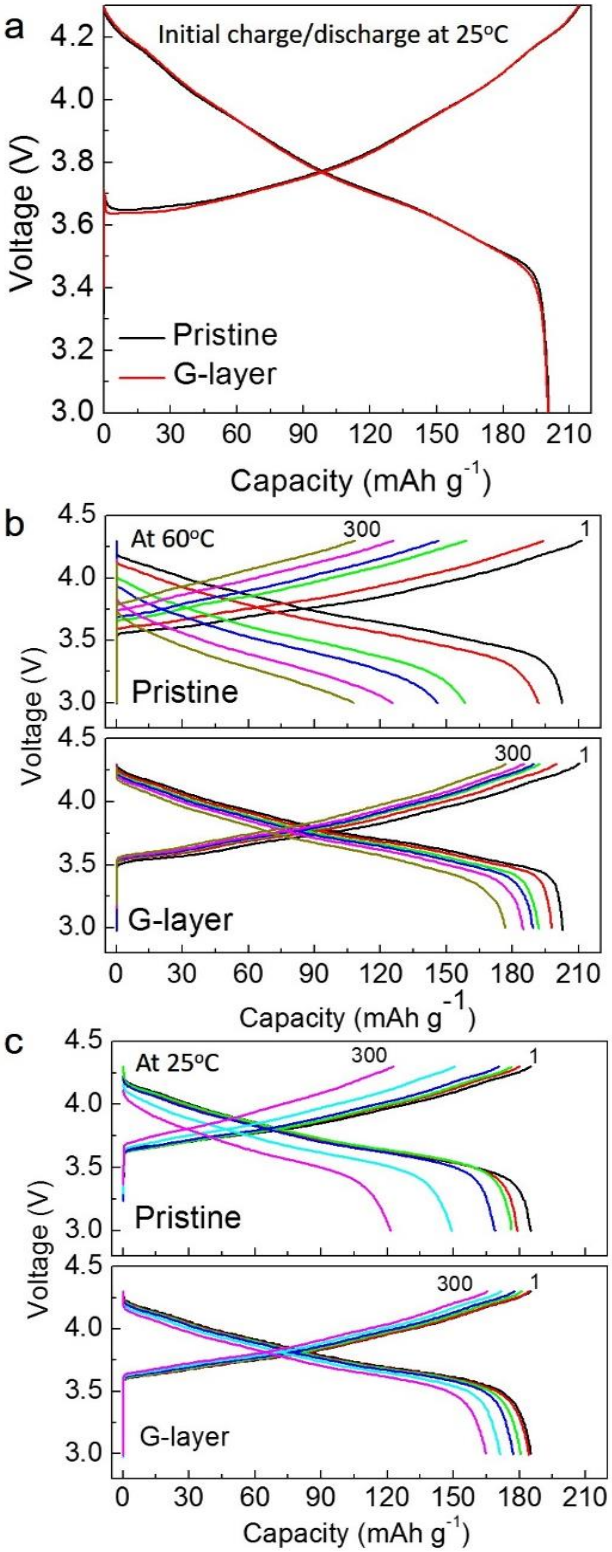

Figure 3.2.7. Voltage profiles of (a) Initial charge and discharge for the Pristine and G-layer sample, (b) Cycling at high temperature (60°C) between 3.0-4.3V, and (c) Cycling at room temperature (25°C) between 3.0-4.3V

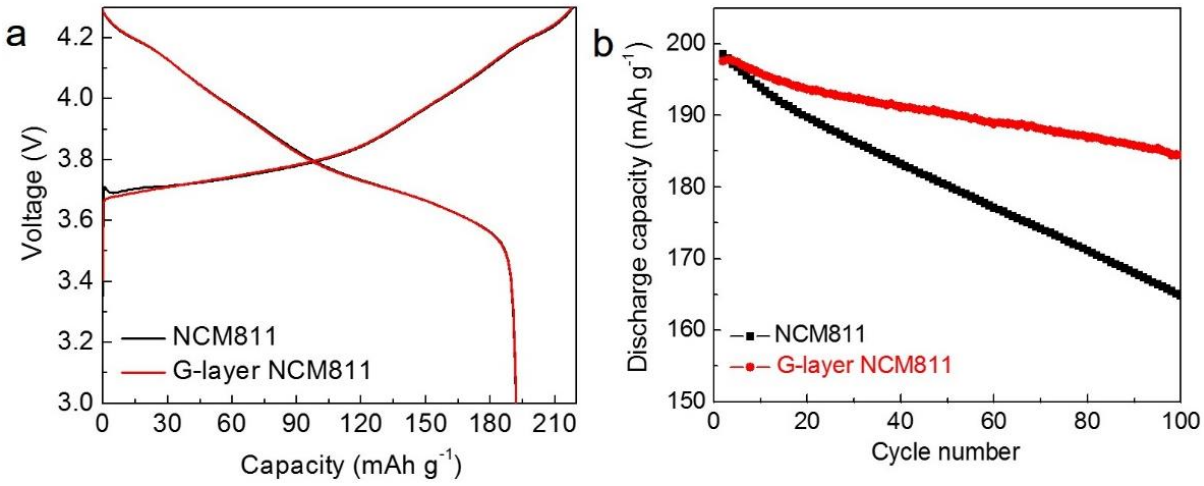

Figure 3.2.8. Voltage profiles of (a) Initial charge and discharge for the $LiNi_{0.8}Co_{0.1}Mn_{0.1}O_2$ (NCM811) and G-layer NCM811 sample, (b) Cycle retention at high temperature (60°C) between 3.0-4.3V for the NCM811 and G-layer NCM811 samples

The Ni-based cathode materials with a layered structure consist of alternately stacked close-packed lithium layers between O-TM-O (TM are transition metals) slabs along the *c*-axis. In the delithiation process, the repulsion force between the two neighbouring oxygen layers was increased by extracting the lithium ions from Li layers. Consequently, lattice parameter *c* increased. Meanwhile, a higher valence state of transition metals leads to a contraction in the ion radius of TM, resulting in a decrease in lattice parameters *a* and *b*. The reverse reaction occurs during the lithiation process, and therefore a large anisotropic lattice volume change occurs during the charge and discharge. The change in lattice parameters for the $LiNi_{0.8}Co_{0.15}Al_{0.05}O_2$ cathode material was reported to be the highest in the layered compounds, showing Δa and Δc of −2.1% and 2.3%, respectively.[60] The large lattice volume change could lead to micro-cracks, inducing an electrochemical grinding effect between grains.[61] On the other hand, a spinel-like structure of the MT-LCO shows a smaller lattice volume change because of concurrent changes in the spinel structure in three-dimension,[62] thereby playing an effective role in mitigating the electrochemical grinding effect.

Figure 3.2.6d and e show the STEM images of the cross-sectional particle of the pristine and G-layer samples after 300 cycles at 60 ℃. Notably, different morphology changes were observed. The pristine sample showed severely developed cleavages of sizes >200 nm between the grains, and all the grains are shattered after the cycling test (Figure 3.2.6d). On the other hand, the G-layer sample retained the pristine morphology of the secondary particle without any collapse (Figure 3.2.6e). These morphological changes were verified in most particles, as shown in Figure 3.2.9. Mitigating micro-cracks in cycling could effectively suppress the development of a new SEI layer as an electrical resistance resulted from the reaction in the electrolyte between grain boundaries (Figure 3.2.10).

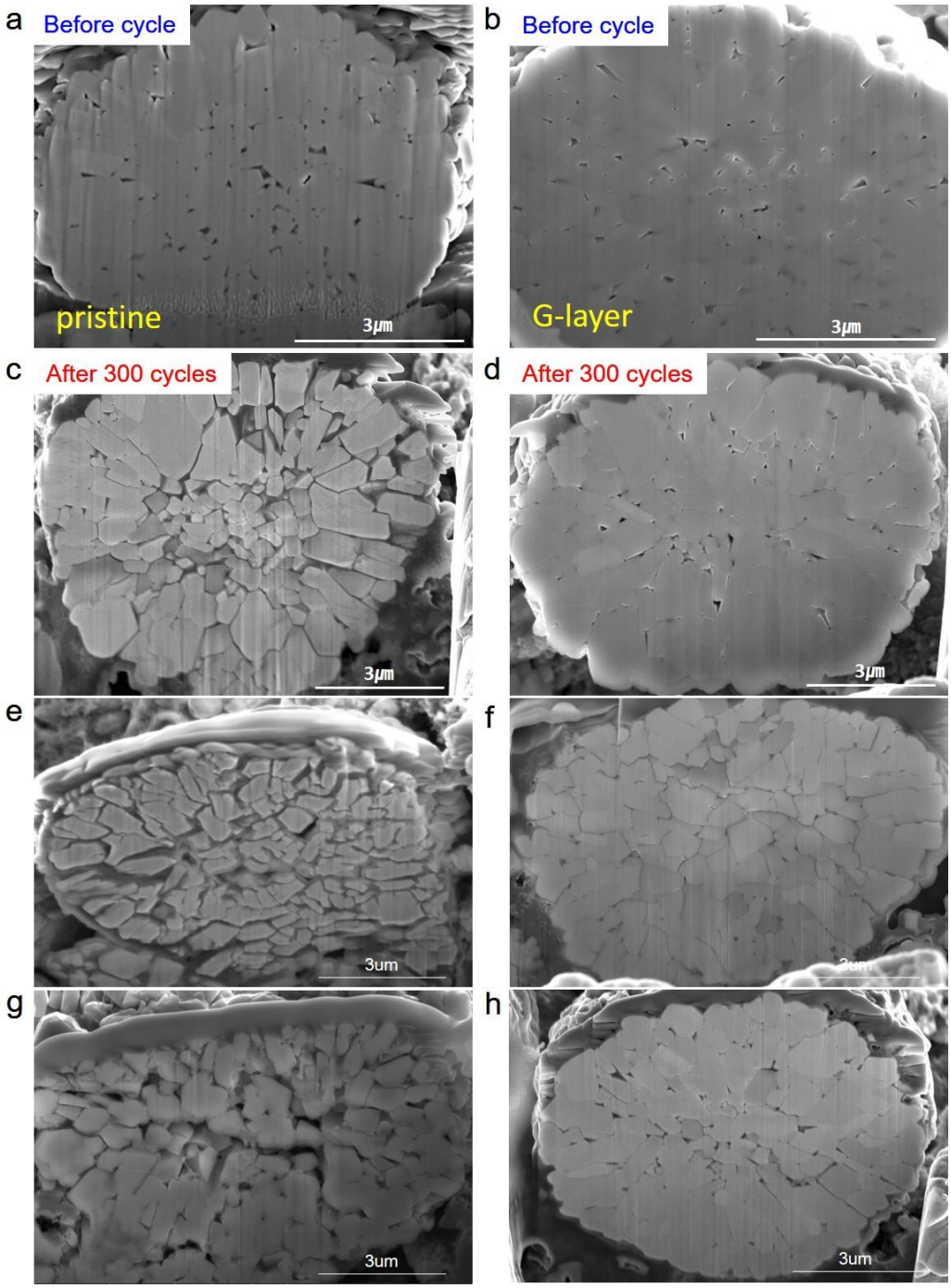

Figure 3.2.9. Cross-sectional SEM images of secondary particles of pristine and G-layer samples. The particle before cycle; (a) Pristine and (b) G-layer samples. The particle after cycle; (c, e, g) Pristine and (d, f, h) G-layer samples.

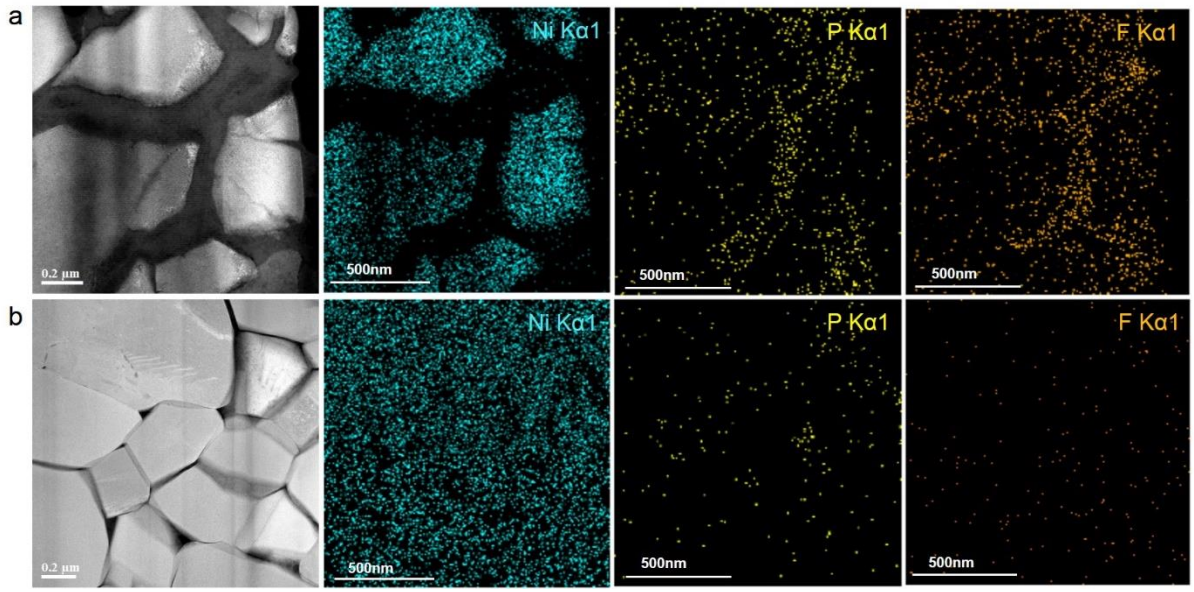

Figure 3.2.10. STEM-EDXS images between grain boundaries of (a) pristine and (b) G-layer samples after 300 cycle at 60 ºC.

Figure 3.2.11a shows the discharge capacity of the two samples as a function of the cycle number with varying discharge current density from 0.1C (= 200 mAh g^{-1}) to 7C (the charge rate was fixed to 0.5C) at 25 ℃. With increasing C-rate, the G-layer sample outperforms the pristine sample and the voltage profiles at different c-rates showed a larger IR drop in the pristine sample than in the G-layer sample. This can be explained by the formation of G-layer in a secondary particle. Nano-sized voids between grains enable an electrolyte to infiltrate the secondary particle so that the high lithium ion diffusivity of the electrolyte can improve the lithium ion mobility in the secondary particle. However, for electron transfer, this morphology is a disadvantage due to the many grain boundaries and voids.[63] Thus, the electron conductivity in the secondary particle can be enhanced by a glue layer as a bridge owing to the following two factors:[64]

1) extended contact area in the secondary particle, and

2) improved electron mobility caused by the higher electron conductivity of MT-LCO

The enhanced rate capability of the G-layer sample was further investigated via in-situ galvanostatic-electrochemical impedance spectroscopy (GS-EIS) during galvanostatic discharge process at 1C rate.[65] The analysis was performed on the charged cell with different depths of discharge (DOD) from 0% to 100% during lithiation. The chronopotentiometric profile of lithiation of the pristine and G-layer samples up to 2.9 V at 1C rate after charging to 4.3 V at 0.5C are presented in Fig. 3.2.11c. Figure 3.2.11d shows the Nyquist plots of the GS-EIS obtained from the charged samples at different ΔDODs of 10, 20, 40, 50, 80, and 90%. The width of intermediate-frequency semi-circles related to R_{CT} increased with increasing ΔDOD. The values of R_{CT} were extracted from the intermediate-frequency semi-circle in the impedance spectra, and the results are presented in Table 3.2.2. At DOD 90%, the R_{CT} value of the G-layer sample was 35 Ω, but that of the pristine sample was 74 Ω. Charge transfer resistance associated with the lithium ion intercalation by reduction reaction should be low in order to deliver a high capacity at high-rate cycling. In this regard, the MT-LCO acting as a bridge between grains could provide the pathway for fast electrons and ion kinetics with effectively reduced charge transfer resistance.

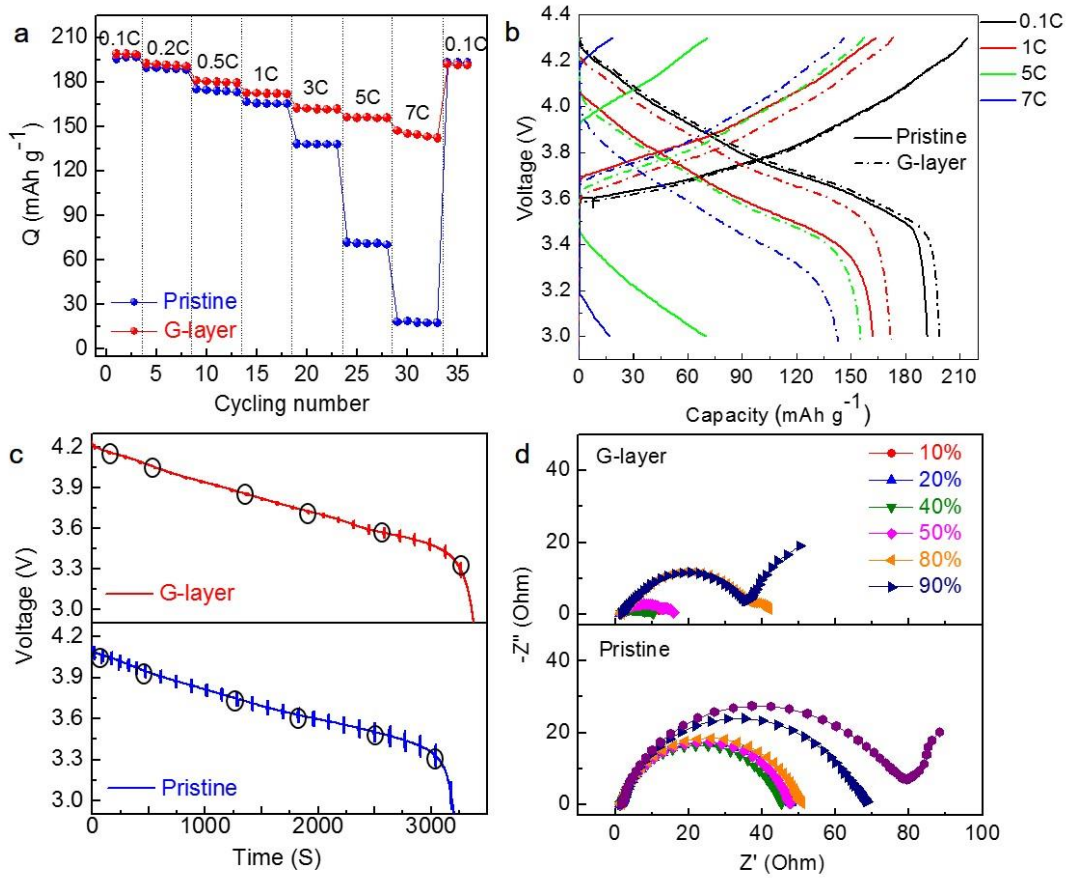

Figure 3.2.11. Rate performance results and GS-EIS analysis data. (**a**) Rate capabilities of Pristine and G-layer evaluated between 3.0 and 4.3 V at 25 ℃. (**b**) Voltage profiles of the first cycles at each C rates during the rate performance test of (a). Galvanostatic-Electrochemical Impedance Spectroscopy (GS-EIS) in discharge at 1C rate; (**c**) Voltage profile of Pristine and G-layer samples. (**d**) Nyquist plots of Pristine and G-layer samples at different DOD of 10%, 20%, 40%, 50%, 80%, and 90% on the chronopotentiometric profiles are measured simultaneously in (c). The EIS spectra consist of high-frequency semi-circles, intermediate-frequency semi-circles, and low-frequency inclined lines. The resistances were characterized by the different frequency semi-circles and inclined lines: (i) solution resistance (R_s) and solid electrolyte interface (SEI) layer resistance (R_{SEI}) by high-frequency semi-circle, (ii) charge transfer resistance (R_{CT}) by intermediate-frequency semi-circle, (iii) Warburg impedance (Z_W) by low-frequency sloped diffusion tail.

Table 3.2.2. GS-EIS fitting results

Parameter	DOD (%)	Pristine	G-layer
R_e /Ω	20%	1.589	1.839
	50%	0.413	1.72
	90%	2.01	1.897
R_{SEI} /Ω	20%	4.131	2.285
	50%	1.263	1.941
	90%	0.825	0.207
R_G /Ω	20%	-	2.861
	50%	-	9.163
	90%	-	11.18
R_{CT} /Ω	20%	42.3	2.081
	50%	48.78	2.51
	90%	74.24	34.99

To investigate the effect of the voids on the interaction between primary particles, the interaction energy was evaluated with respect to the gap distance between two spherical NCA particles of layered structure with (001) facets facing with each other. The (001) facets are dominant in the layered structure with a stable energy state. Three combinations of termination type of each surface (i.e. Li/Li, Li/O and O/O) were taken into account. As shown in Figure 3.2.12a, the interaction energies between two particles become negligible at the gap distance of ~5 nm regardless of the types of terminations. Considering the voids with a size of >10 nm and the tiny gap distance observed using HR-TEM (Figure 3.2.3b) was in a range of 2–10 nm, resulting a weak binding force between the grains. Thus, to observe the filling effect by MT-LCO of the spinel structure as a glue layer, we calculated the binding energies of combinatorial interfaces between NCA (001), (101), (104), or (110), and MT-LCO (001), (101), (113), or (111) surfaces by constructing slab models (Figure 3.2.15 - 3.2.18). Figure 3.2.12b shows the average binding energies of interfaces classified by surface polarity. For all cases, the binding strengths of NCA/MT-LCO interfaces were larger than those of NCA/NCA interfaces. This result clearly suggests that MT-LCO filling the voids can play the role of glue between NCA particles (Figure 3.2.12c).

These glue-like effects were investigated in detail with the structural properties (i.e. surface polarity, surface planar density, coordination number of surface) of each surface of NCA and MT-LCO. Interfaces formed with O-terminated NCA(001) have large binding energies on average due to large polarity (Figure 3.2.14a). Especially, the binding strength between polar O-terminated NCA(001) and polar MT-LCO(113) has the largest value (i.e. -64.71 J m^{-2}), where the dipole moment induces metal infiltration into the interfacial region to develop strong adhesion (Left configuration in Figure 3.2.12d). Other factors such as planar density of each surface and coordination number of atoms located in the outermost surface also acted on the interfacial binding energies.[66] Low surface-planar densities with low-coordinated Ni, Al, and Co usually induced the diffusion of surface atoms due to low coherence so that higher binding energy was eventually expected. To investigate the isolated effects of surface planar density and coordination number of surface, nonpolar surface slabs (i.e. NCA(104), NCA(110), MT-LCO(101), and MT-LCO(001)) were chosen for analysis. The interfaces with higher planar densities and higher coordination numbers of outermost metal atoms (i.e. NCA(104), MT-LCO(001)) had lower binding energies (Figure 3.2.14c). Those factors induced a low diffusivity of surface atoms (Middle configuration in Figure 3.2.12d).

NCA/NCA interfaces were investigated to estimate the binding energies of initial grain boundaries of fully bound NCA primary particles. Among these interfaces, binding energy was found to be relatively high when the interface was formed with NCA(001) surface (Figure 3.2.14b)

because of atomic diffusion into the interfacial region when the same termination (i.e. O/O, Li/Li) was applied (Figure 3.2.17). Especially, for the O-terminated NCA(001) surface, the diffusions of Ni, Al, and Co into the interfacial region induced a large interfacial energy (i.e. -34.01J m^{-2}) (Right configuration in Figure 3.2.12d), which was comparable to that of NCA/MT-LCO. However, it does not change the fact that the average binding strength is still expected to be larger for the interface of NCA/MT-LCO in consideration of the presence of several difference interfaces and also of the presence of voids.

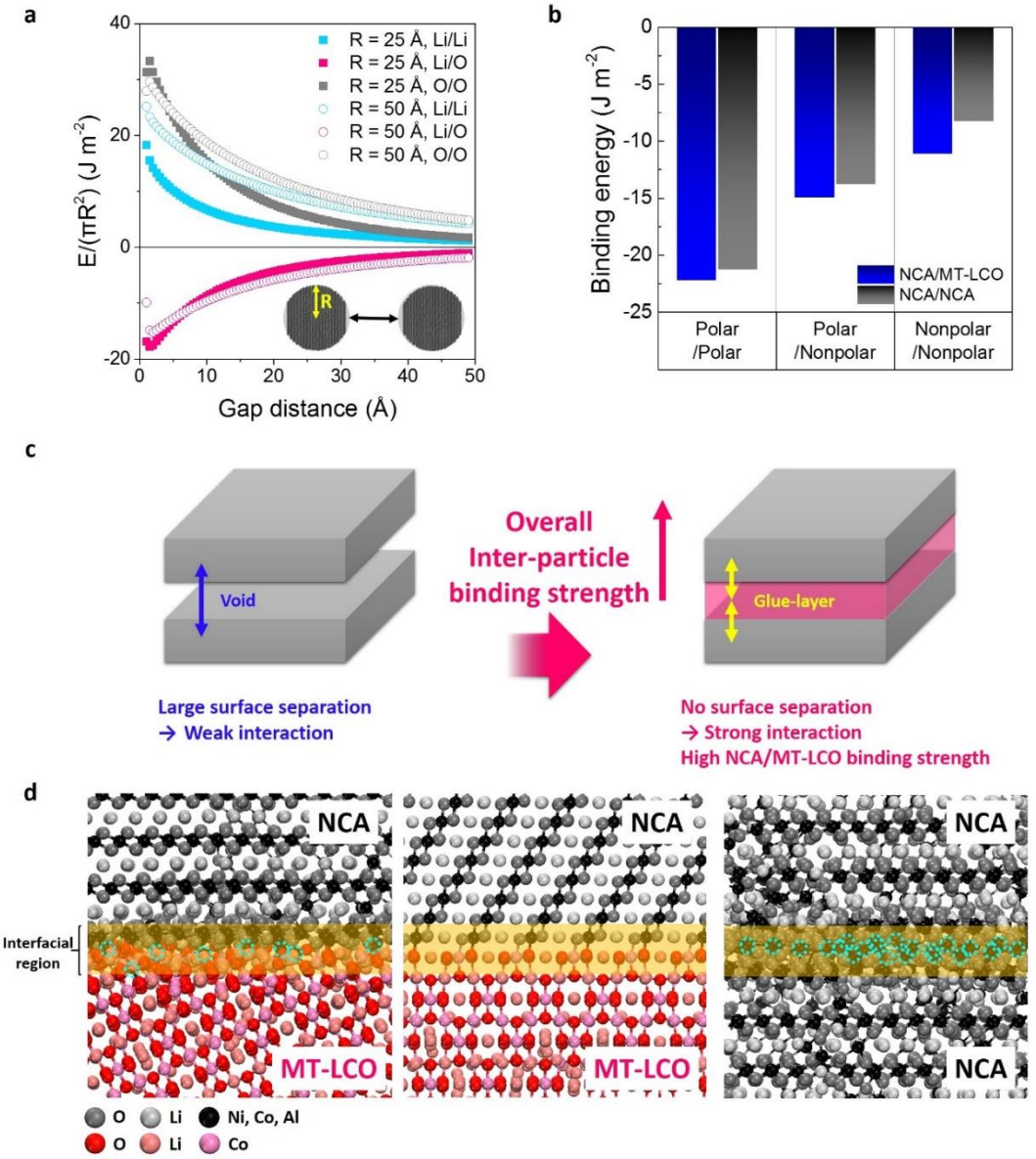

Figure 3.2.12. Results of molecular dynamics (MD) simulation. (a) Interfacial energy gradient depend on distance between NCA particles with radius of 25 Å and 50 Å with different terminations. (i.e. Li termination and Oxygen termination) (b) The average binding energy of unit area (J/m^2) between surfaces classified depending on the surface polarity. (i.e. polar surfaces : NCA(001), NCA(101), MT-LCO(113), and MT-LCO(111), nonpolar surfaces : NCA(104), NCA(110), MT-LCO(001), and MT-LCO(101). Blue bar indicates the binding energy between NCA and MT-LCO surfaces. Grey bar indicates the binding energy between NCA and NCA surfaces. (c) Schematic illustration of interfacial binding energies of void and glue-layer. (d) Left : Interface of O-terminated NCA(001) with O-terminated MT-LCO(113); Middle : NCA(104) with MT-LCO(001); Right : O-terminated NCA(001) with O-terminated NCA(001). Interfacial region is expressed with orange color and infiltrated Ni, Al, and Co atoms from NCA were expressed with cyan dashed-circle.

Table 3.2.3. Planar density of Li, TM, and O atoms at the surface, and coordination number of outermost TM of each surface model.

Surface	Index	Termination	Planar density ($Å^{-2}$)				Coordination # of outermost TM
			Total	Li	TM	O	
NCA	(001)	Li	0.141	0.141	-	-	6
		O	0.141	-	-	0.141	6
	(104)	$LiNi_{5c}O$	0.243	0.061	0.061	0.121	5
	(101)	Li	0.073	0.073	-	-	5
	(101)	O	0.073	-	-	0.073	5
	(110)	$LiNi_{4c}O$	0.171	0.043	0.043	0.085	4
MT-LCO	(001)	$LiCo_{5c}O$	0.249	0.062	0.062	0.125	5
	(101)	$LiCo_{4c}O$-1 & $LiCo_{4c}O$-2	0.176	0.044	0.044	0.088	4
	(113)	$LiCo_{3c}$	0.076	0.057	0.019	-	3
		O	0.057	-	-	0.057	5
	(111)	O-1	0.072	-	-	0.072	6
		O-2	0.072	-	-	0.072	6

Table 3.2.4. Interaction parameters of short-range Buckingham potential and charge of each ion.

Interaction	***A* (eV)**	**ρ (Å)**	***C* (eVÅ $^{-6}$)**	***q*(e)**
Li^{+}−O^{2-}	632.1018	0.2906	0.00	+1
Co^{3+}−O^{2-}	1329.820	0.3087	0.00	+3
Ni^{3+}−O^{2-}	1279.230	0.2932	0.00	+3
Al^{3+}−O^{2-}	1114.9	0.3118	0.00	+3
O^{2-}−O^{2-}	22764.3	0.149	44.53	-2

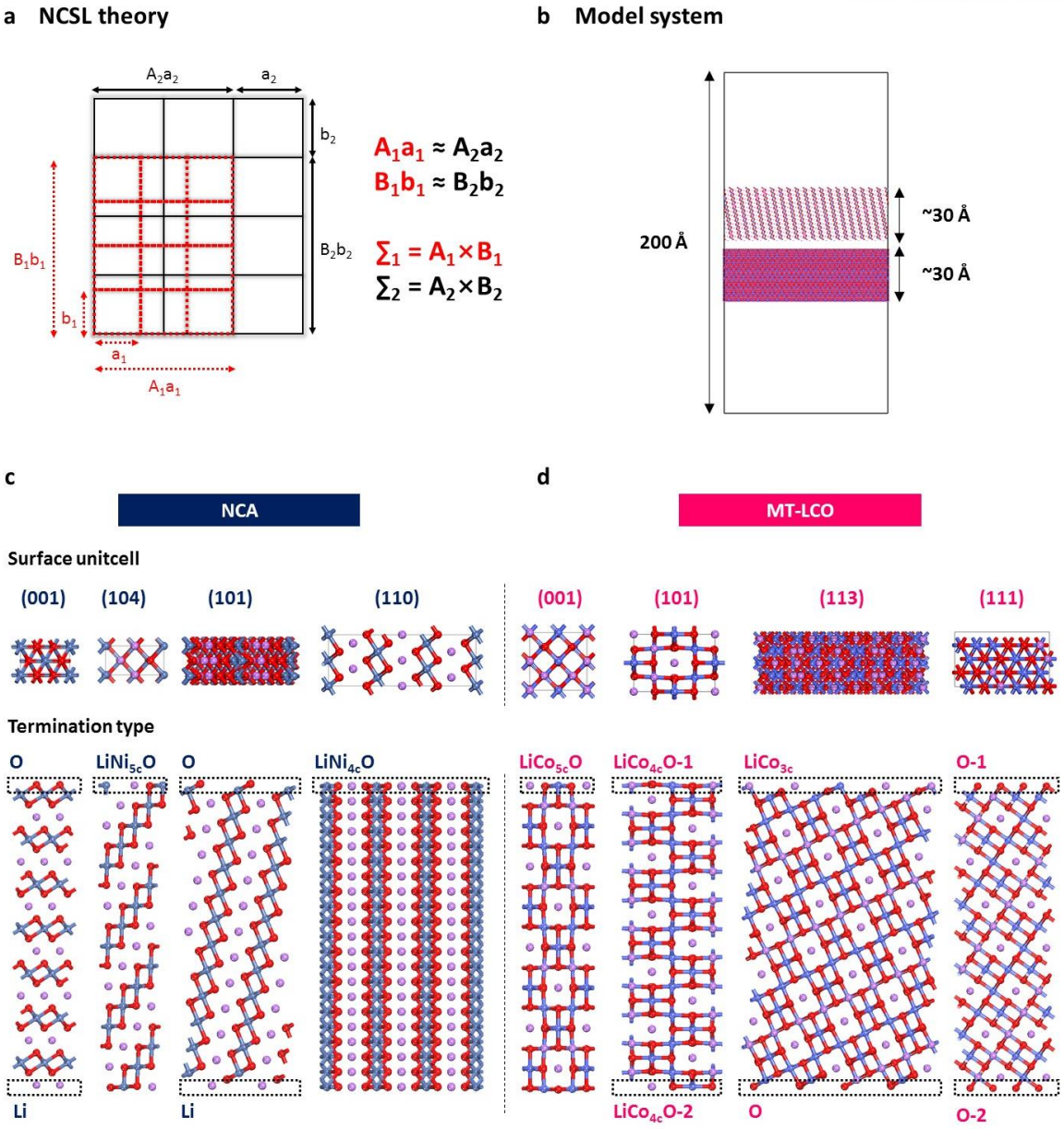

Figure 3.2.13. Scheme of interface modeling. (a) Near Coincidence Site Lattice (NCSL) theory. Two rectangular surface lattices (solid black lines and red dotted lines) are shown with lattice parameters (i.e. a1, b1, a2, and b2) and supercell size parameters (A1, B1, A2 and B2). (b) Representative interface model system composed of two surface slabs. (c) and (d) Top view and side view of each rectangular unit cell of NCA and MT-LCO surfaces, respectively. Dotted-lines represent termination type of each surface. Li, Ni, Co and O atom are bright purple, navy, blue, red color respectively. Al and Co dopants are not shown in NCA surface because Ni atoms are randomly replaced by dopants after building interface.

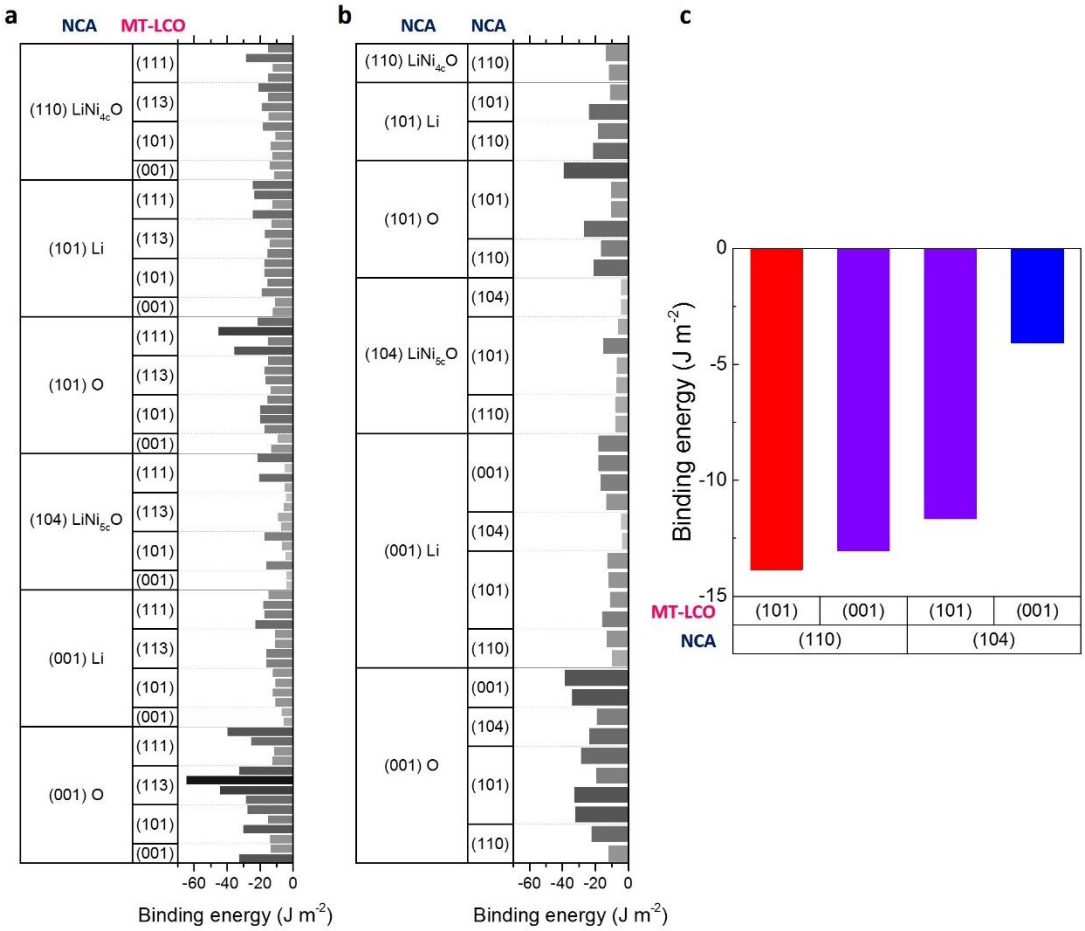

Figure 3.2.14. The binding energy of unit area (J/m2) of each (a) NCA/MT-LCO and (b) NCA/NCA interface. NCA surface slab was described with termination. (c) Non-polar NCA/MT-LCO. Red bar indicates combination of low planar density slabs, purple bar indicates combination of high planar density slab and low planar density slab, and blue bar indicates combination of high planar density slabs.

Figure 3.2.15. Final configuration of each NCA/MT-LCO interface formed with NCA(001) and NCA(104) with planar coincidence densities (i.e. Σ_N and Σ_M for NCA and MT-LCO) and binding energies (J/m^2). Li, Ni, Co, Al and O atom are bright purple, navy, blue, pink, and red color respectively.

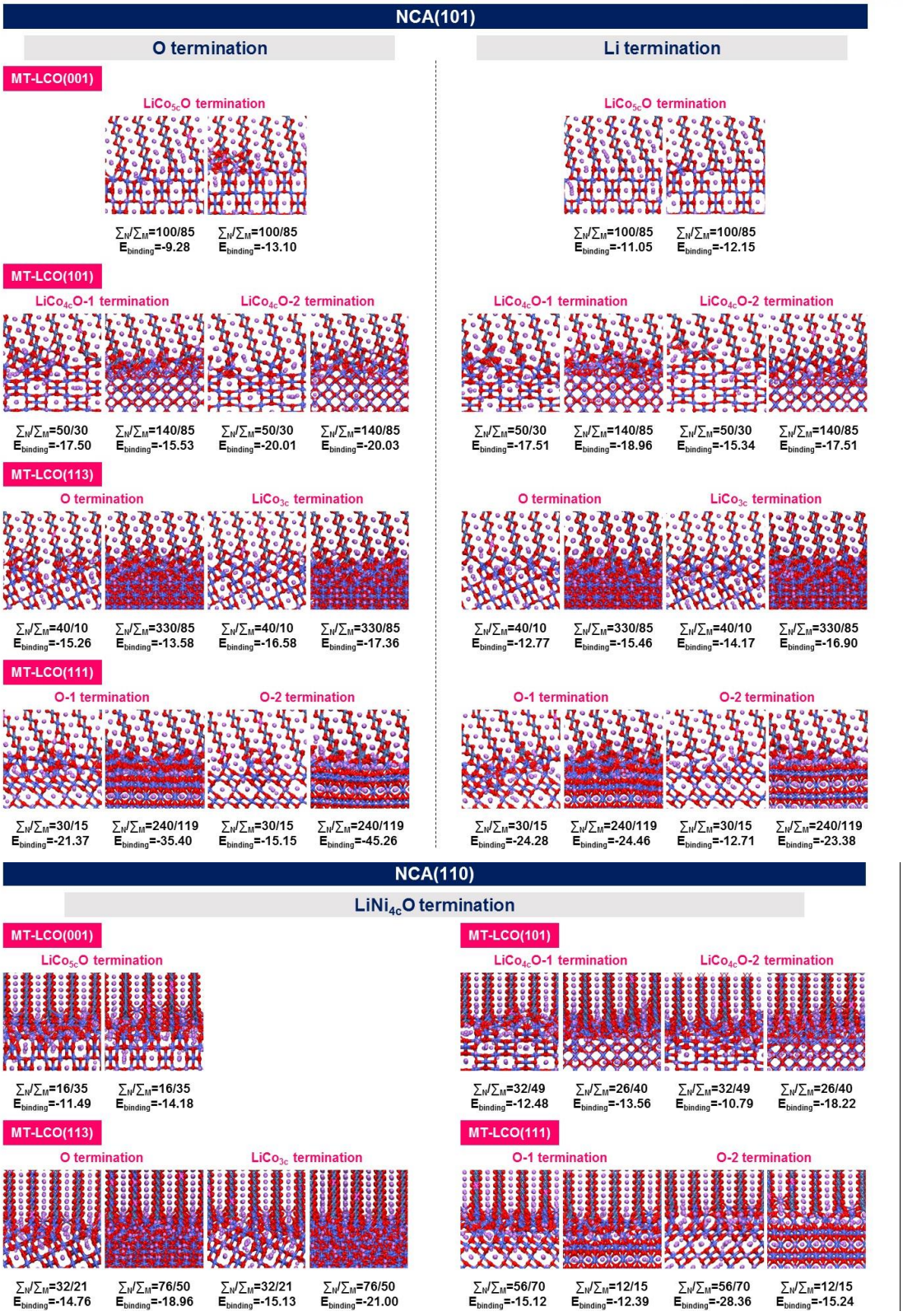

Figure 3.2.16. Final configuration of each NCA/MT-LCO interface formed with NCA(101) and NCA(110) with planar coincidence densities (i.e. Σ_N and Σ_M for NCA and MT-LCO) and binding energies (J/m^2). Li, Ni, Co, Al and O atom are bright purple, navy, blue, pink, and red color respectively.

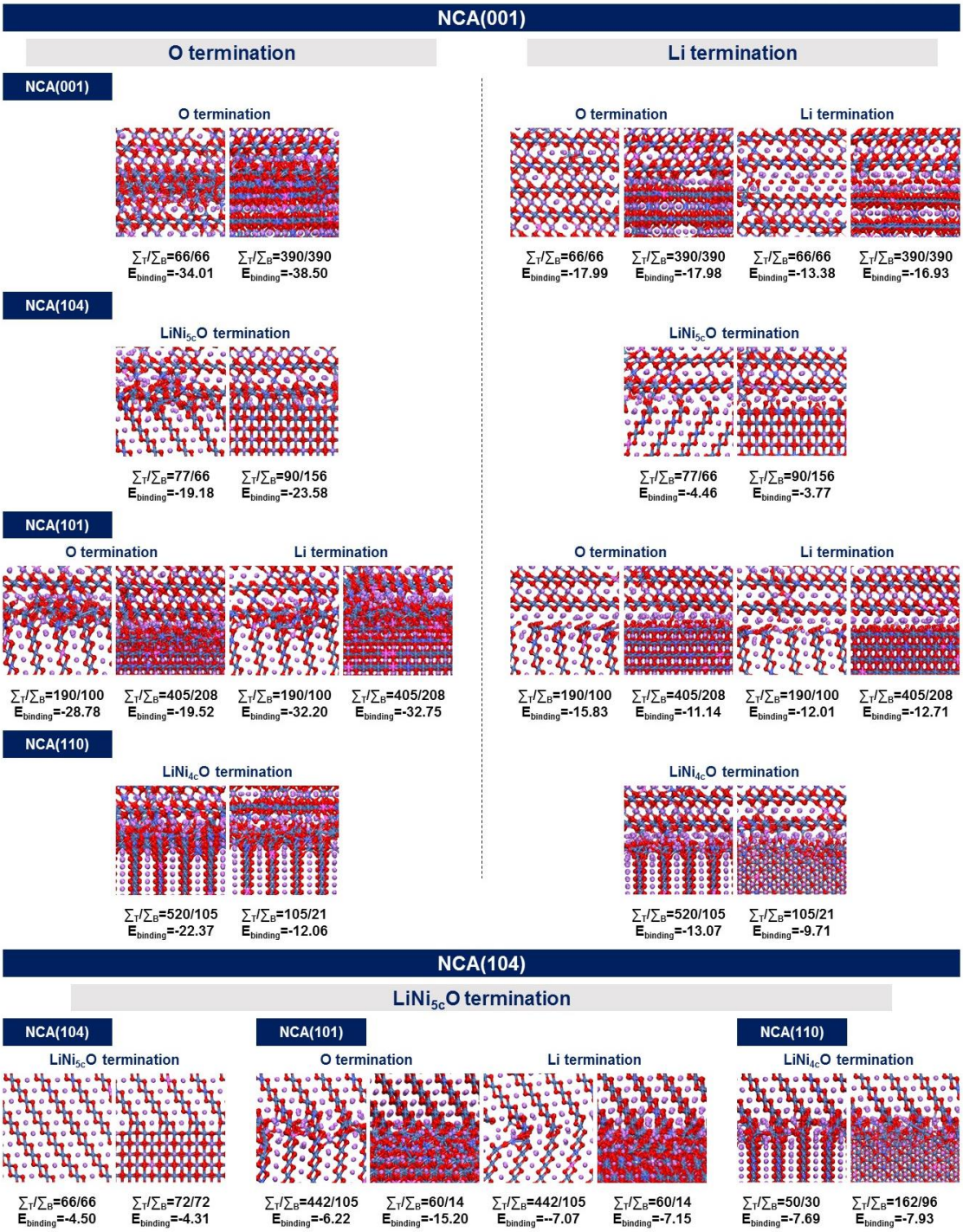

Figure 3.2.17. Final configuration of each NCA/NCA interface formed with NCA(001) and NCA(104) with planar coincidence densities (i.e. Σ_T and Σ_P for NCA on top and bottom) and binding energies (J/m^2). Li, Ni, Co, Al and O atom are bright purple, navy, blue, pink, and red color respectively.

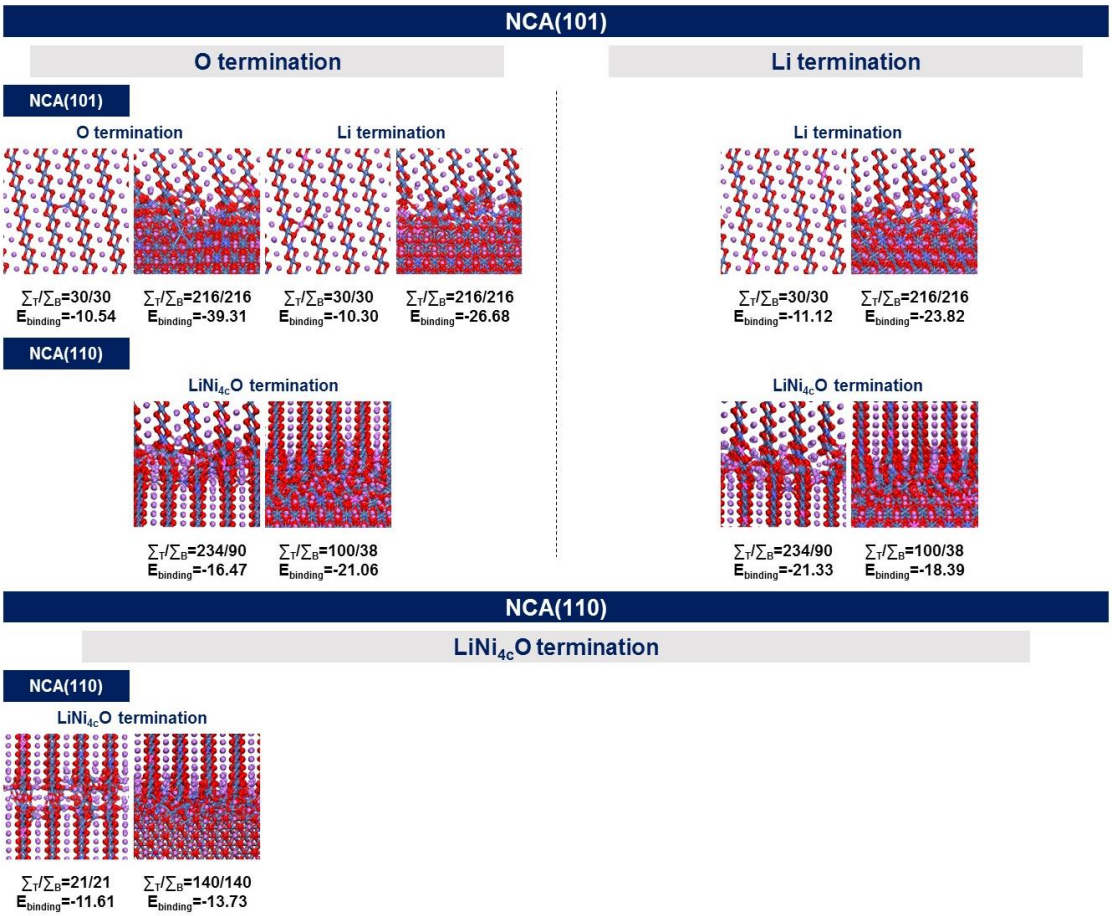

Figure 3.2.18. Final configuration of each NCA/NCA interface formed with NCA(101) and NCA(110) with planar coincidence densities (i.e. Σ_T and Σ_P for NCA on top and bottom) and binding energies (J/m^2). Li, Ni, Co, Al and O atom are bright purple, navy, blue, pink, and red color respectively.

3.2.4 Conclusion

We successfully introduce a thin spinel-Li_xCoO_2 layer in- and outside of a $LiNi_{0.8}Co_{0.15}Al_{0.05}O_2$ (NCA) secondary particle via the solution-based coating method. The obtained cathode demonstrated an outstanding cyclability with ~87% of capacity retention after 300 cycles at both RT and 60 ℃ and an excellent rate capability. The coating layer could effectively protect the unstable surface of primary particles of the Ni-rich cathode during cycles; moreover, the mechanical strength and electronic conductivity of a secondary particle could be enhanced by reducing the gaps between anisotropically oriented grains. The role of spinel-Li_xCoO_2 layer was further investigated through molecular dynamics simulations. The binding strength of NCA/MT-LCO interfaces was larger than that of NCA/NCA interfaces, so that MT-LCO filling the voids in the NCA secondary particle could play a key role in enhancing its mechanical strength. Thus, considering the interfacial binding strength between the host and the coating, the solution-based active material coating on a secondary particle opens up a new approach to advanced Li-ion battery cathode.

REFERENCES

1. Lee, B.-R.; Noh, H.-J.; Myung, S.-T.; Amine, K.; Sun, Y.-K., High-Voltage Performance of Li [Ni0.55Co0.15Mn0.30] O2 Positive Electrode Material for Rechargeable Li-Ion Batteries. *Journal of The Electrochemical Society* **2011,** *158* (2), A180-A186.
2. Kyung-Wan, N.; Seong-Min, B.; Enyuan, H.; Xiqian, Y.; Youngning, Z.; Xiaojian, W.; Lijun, W.; Yimei, Z.; Kyung-Yoon, C.; Xiao-Qing, Y., Combining In Situ Synchrotron X-Ray Diffraction and Absorption Techniques with Transmission Electron Microscopy to Study the Origin of Thermal Instability in Overcharged Cathode Materials for Lithium-Ion Batteries. *Advanced Functional Materials* **2013,** *23*.
3. Julien, C.; Mauger, A.; Zaghib, K.; Groult, H., Comparative Issues of Cathode Materials for Li-Ion Batteries. *Inorganics* **2014,** *2* (1), 132-154.
4. Ohzuku, T.; Ueda, A.; Nagayama, M.; Iwakoshi, Y.; Komori, H., COMPARATIVE-STUDY OF LICOO2, LINI1/2CO1/2O2 AND LINIO2 FOR 4-VOLT SECONDARY LITHIUM CELLS. *Electrochimica Acta* **1993,** *38*, 1159-1167.
5. Zhecheva, E.; Stoyanova, R., STABILIZATION OF THE LAYERED CRYSTAL-STRUCTURE OF LINIO2 BY CO-SUBSTITUTION. *Solid State Ionics* **1993,** *66*, 143-149.
6. (a) Ohzuku, T.; Makimura, Y., Layered lithium insertion material of LiCo 1/3 Ni 1/3 Mn 1/3 O 2 for lithium-ion batteries. *Chemistry Letters* **2001**; (b) Yabuuchi, N.; Ohzuku, T., Novel lithium insertion material of LiCo1/3Ni1/3Mn1/3O2 for advanced lithium-ion batteries. *Journal of Power Sources* **2003,** *119*, 171-174.
7. Lee, M. H.; Kang, Y. J.; Myung, S. T.; Sun, Y. K., Synthetic optimization of Li [Ni 1/3 Co 1/3 Mn 1/3] O 2 via co-precipitation. *Electrochimica Acta* **2004,** *50* (4), 939-948.
8. Liu, W.; Oh, P.; Liu, X.; Lee, M.-J.; Cho, W.; Chae, S.; Kim, Y.; Cho, J., Nickel-Rich Layered Lithium Transition-Metal Oxide for High-Energy Lithium-Ion Batteries. *Angewandte Chemie International Edition* **2015,** *54* (15), 4440-4457.
9. Edström, K.; Gustafsson, T.; Thomas, J., The cathode–electrolyte interface in the Li-ion battery.

Electrochimica Acta **2004,** *50* (2), 397-403.

10. Kawamura, T.; Okada, S.; Yamaki, J.-i., Decomposition reaction of LiPF6-based electrolytes for lithium ion cells. *Journal of Power Sources* **2006,** *156* (2), 547-554.
11. Watanabe, S.; Kinoshita, M.; Hosokawa, T.; Morigaki, K.; Nakura, K., Capacity fade of LiAlyNi1−x−yCoxO2 cathode for lithium-ion batteries during accelerated calendar and cycle life tests (surface analysis of LiAlyNi1−x−yCoxO2 cathode after cycle tests in restricted depth of discharge ranges). *Journal of Power Sources* **2014,** *258* (0), 210-217.
12. Cho, J.; Kim, T. J.; Kim, Y. J.; Park, B., High-performance ZrO2-coated LiNiO2 cathode material. *Electrochemical and Solid State Letters* **2001,** *4* (10), A159-A161.
13. Cho, J.; Kim, Y. J.; Park, B., Novel LiCoO2 Cathode Material with Al2O3 Coating for a Li Ion Cell. *Chemistry of Materials* **2000,** *12* (12), 3788-3791.
14. Sun, Y.-K.; Myung, S.-T.; Park, B.-C.; Prakash, J.; Belharouak, I.; Amine, K., High-energy cathode material for long-life and safe lithium batteries. *Nature materials* **2009,** *8* (4), 320-324.
15. Cho, Y.; Lee, S.; Lee, Y.; Hong, T.; Cho, J., Spinel-Layered Core-Shell Cathode Materials for Li-Ion Batteries. *Advanced Energy Materials* **2011,** *1* (5), 821-828.
16. Bruno, S.; Jürgen, G., Lithium batteries: Status, prospects and future. *Journal of Power Sources* **2010,** *195*, 2419–2430.
17. (a) Arai, H., Thermal behavior of Li1−yNiO2 and the decomposition mechanism. *Solid State Ionics* **1998,** *109*, 295-302; (b) Feng, L.; Isaac, M. M.; Dennis, N.; Tsu-Chien, W.; Mark, D. A.; Huolin, L. X.; Marca, M. D., Surface reconstruction and chemical evolution of stoichiometric layered cathode materials for lithium-ion batteries. *Nature Communications* **2014,** *5*.
18. Jung, S.-K.; Gwon, H.; Hong, J.; Park, K.-Y.; Seo, D.-H.; Kim, H.; Hyun, J.; Yang, W.; Kang, K., Understanding the Degradation Mechanisms of LiNi0.5Co0.2Mn0.3O2 Cathode Material in Lithium Ion Batteries. *Advanced Energy Materials* **2013**, 16931-16940.
19. Nam, K. W.; Bak, S. M.; Hu, E.; Yu, X.; Zhou, Y.; Wang, X.; Wu, L.; Zhu, Y.; Chung, K. Y.; Yang, X. Q., Combining in situ synchrotron X-Ray diffraction and absorption techniques with transmission electron microscopy to study the origin of thermal instability in overcharged cathode materials for

lithium-ion batteries. *Advanced Functional Materials* **2013,** *23* (8), 1047-1063.

20. Gu, M.; Belharouak, I.; Zheng, J.; Wu, H.; Xiao, J.; Genc, A.; Amine, K.; Thevuthasan, S.; Baer, D. R.; Zhang, J.-G.; Browning, N. D.; Liu, J.; Wang, C., Formation of the Spinel Phase in the Layered Composite Cathode Used in Li-Ion Batteries. *ACS Nano* **2012,** *7* (1), 760-767.
21. Kaoru, D., In Situ Observation of LiNiO[sub 2] Single-Particle Fracture during Li-Ion Extraction and Insertion. *Electrochemical and Solid-State Letters* **1999,** *3*, 125-127.
22. Kleiner, K.; Dixon, D.; Jakes, P.; Melke, J.; Yavuz, M.; Roth, C.; Nikolowski, K.; Liebau, V.; Ehrenberg, H., Fatigue of LiNi0.8Co0.15Al0.05O2 in commercial Li ion batteries. *Journal of Power Sources* **2015,** *273* (0), 70-82.
23. Haifeng, W., TEM Study of Electrochemical Cycling-Induced Damage and Disorder in LiCoO[sub 2] Cathodes for Rechargeable Lithium Batteries. *Journal of The Electrochemical Society* **1999,** *146*, 473-480.
24. (a) Min Gyu, K.; Jaephil, C., Air stable Al2O3-coated Li2NiO2 cathode additive as a surplus current consumer in a Li-ion cell. *Journal of Materials Chemistry* **2008,** *18*, 5880–5887; (b) Lee, S. M.; Oh, S. H.; Ahn, J. P.; Cho, W. I.; Jang, H., Electrochemical properties of ZrO2-coated LiNi0.8Co0.2O2 cathode materials. *Journal of Power Sources* **2006,** *159*, 1334-1339; (c) Jaephil, C.; Tae-Joon, K.; Yong Jeong, K.; Byungwoo, P., High-Performance ZrO[sub 2]-Coated LiNiO[sub 2] Cathode Material. *Electrochemical and Solid-State Letters* **2001,** *4*, A159-A161.
25. Yonghyun, C.; Sanghan, L.; Yongseok, L.; Taeeun, H.; Jaephil, C., Spinel-Layered Core-Shell Cathode Materials for Li-Ion Batteries. *Advanced Energy Materials* **2011,** *1*, 821–828.
26. (a) Miller, D. J.; Proff, C.; Wen, J. G.; Abraham, D. P.; Bareño, J., Observation of Microstructural Evolution in Li Battery Cathode Oxide Particles by In Situ Electron Microscopy. *Advanced Energy Materials* **2013,** *3* (8), 1098-1103; (b) Lee, E.-J.; Chen, Z.; Noh, H.-J.; Nam, S. C.; Kang, S.; Kim, D. H.; Amine, K.; Sun, Y.-K., Development of Microstrain in Aged Lithium Transition Metal Oxides. *Nano Letters* **2014**, 4873–4880; (c) Feng, L.; Dennis, N.; Isaac, M. M.; Tsu-Chien, W.; Huolin, L. X.; Marca, M. D., Profiling the nanoscale gradient in stoichiometric layered cathode particles for lithium-ion batteries. *Energy & Environmental Science* **2014,** *7*, 3077–3085.

27. (a) Hyunjung, L.; Yoojung, K.; Young-Sik, H.; Yoojin, K.; Min Gyu, K.; Nam-Soo, S.; Jaephil, C., Structural Characterization of the Surface-Modified Li[sub x]Ni[sub 0.9]Co[sub 0.1]O[sub 2] Cathode Materials by MPO[sub 4] Coating (M=Al, Ce, SrH, and Fe) for Li-Ion Cells. *Journal of The Electrochemical Society* **2006,** *153*, A781-A786; (b) Meng, X.; Yang, X.-Q.; Sun, X., Emerging applications of atomic layer deposition for lithium-ion battery studies. *Advanced materials (Deerfield Beach, Fla.)* **2012,** *24* (27), 3589-3615; (c) Guo-Rong, H.; Xin-Rong, D.; Zhong-Dong, P.; Ke, D., Comparison of AlPO4- and Co3(PO4)2-coated LiNi0.8Co0.2O2 cathode materials for Li-ion battery. *Electrochimica Acta* **2008,** *53*, 2567–2573; (d) Cho, Y.; Oh, P.; Cho, J., A new type of protective surface layer for high-capacity Ni-based cathode materials: nanoscaled surface pillaring layer. *Nano Lett* **2013,** *13* (3), 1145-52; (e) Sun, Y.-K.; Chen, Z.; Noh, H.-J.; Lee, D.-J.; Jung, H.-G.; Ren, Y.; Wang, S.; Yoon, C. S.; Myung, S.-T.; Amine, K., Nanostructured high-energy cathode materials for advanced lithium batteries. *Nat Mater* **2012,** *11* (11), 942-947.

28. Noh, M.; Cho, J., Optimized synthetic conditions of LiNi0. 5Co0. 2Mn0. 3O2 cathode materials for high rate lithium batteries via co-precipitation method. *Journal of The Electrochemical Society* **2013,** *160* (1), A105-A111.

29. Rougier, A.; Saadoune, I.; Gravereau, P.; Willmann, P.; Delmas, C., Effect of cobalt substitution on cationic distribution in LiNi1-yCoyO2 electrode materials. *Solid State Ionics* **1996,** *90*, 83-90.

30. (a) Laffont, L.; Gibot, P., High resolution electron energy loss spectroscopy of manganese oxides: Application to Mn< sub> 3</sub> O< sub> 4</sub> nanoparticles. *Materials Characterization* **2010,** *61* (11), 1268-1273; (b) Rask, J. H.; Miner, B. A.; Buseck, P. R., Determination of manganese oxidation states in solids by electron energy-loss spectroscopy. *Ultramicroscopy* **1987,** *21* (4), 321-326.

31. (a) Boulineau, A.; Simonin, L.; Colin, J.-F.; Canévet, E.; Daniel, L.; Patoux, S., Evolutions of Li1.2Mn0.61Ni0.18Mg0.01O2 during the Initial Charge/Discharge Cycle Studied by Advanced Electron Microscopy. *Chemistry of Materials* **2012,** *24* (18), 3558-3566; (b) Gu, M.; Genc, A.; Belharouak, I.; Wang, D.; Amine, K.; Thevuthasan, S.; Baer, D. R.; Zhang, J. G.; Browning, N. D.; Liu, J.; Wang, C., Nanoscale phase separation, cation ordering, and surface chemistry in pristine

Li1.2Ni0.2Mn0.6O2 for Li-ion batteries. *Chemistry of Materials* **2013,** *25* (11), 2319-2326.

32. Shaju, K.; Subba, G.; Chowdari, B., Performance of layered Li (Ni< sub> 1/3</sub> Co< sub> 1/3</sub> Mn< sub> 1/3</sub>) O< sub> 2</sub> as cathode for Li-ion batteries. *Electrochimica Acta* **2002**, 145-151.
33. Chevrier, V.; Ong, S.; Armiento, R.; Chan, M.; Ceder, G., <title>Hybrid density functional calculations of redox potentials and formation energies<?xpp qa?> of transition metal compounds</title>. *Physical Review B* **2010,** *82* (7), 075122.
34. Shao-Horn, Y., Understanding Phase Transformations in Lithium Battery Materials by Transmission Electron Microscopy. In *Lithium Batteries*, Nazri, G.-A.; Pistoia, G., Eds. Springer US: 2003; pp 478-506.
35. Lee, J.; Urban, A.; Li, X.; Su, D.; Hautier, G.; Ceder, G., Unlocking the Potential of Cation-Disordered Oxides for Rechargeable Lithium Batteries. *Science* **2014,** *343* (6170), 519-522.
36. Nam, K.-W.; Bak, S.-M.; Hu, E.; Yu, X.; Zhou, Y.; Wang, X.; Wu, L.; Zhu, Y.; Chung, K.-Y.; Yang, X.-Q., Combining In Situ Synchrotron X-Ray Diffraction and Absorption Techniques with Transmission Electron Microscopy to Study the Origin of Thermal Instability in Overcharged Cathode Materials for Lithium-Ion Batteries. *Advanced Functional Materials* **2013,** *23* (8), 1047-1063.
37. (a) Armand, M.; Tarascon, J. M., Building better batteries. *Nature* **2008,** *451* (7179), 652-657; (b) Choi, N.-S.; Chen, Z.; Freunberger, S. A.; Ji, X.; Sun, Y.-K.; Amine, K.; Yushin, G.; Nazar, L. F.; Cho, J.; Bruce, P. G., Challenges Facing Lithium Batteries and Electrical Double-Layer Capacitors. *Angewandte Chemie International Edition* **2012,** *51* (40), 9994-10024.
38. Ohzuku, T.; Ueda, A.; Kouguchi, M., Synthesis and Characterization of LiAl1 / 4Ni3 / 4 O 2 (R 3̄m) for Lithium-Ion (Shuttlecock) Batteries. *Journal of The Electrochemical Society* **1995,** *142* (12), 4033-4039.
39. Kalyani, P.; Kalaiselvi, N., Various aspects of LiNiO2 chemistry: A review. *Science and Technology of Advanced Materials* **2005,** *6* (6), 689-703.
40. (a) Yonghyun, C.; Sanghan, L.; Yongseok, L.; Taeeun, H.; Jaephil, C., Spinel-Layered Core-Shell

Cathode Materials for Li-Ion Batteries. *Advanced Energy Materials* **2011,** *1*; (b) Shi, H.; Wang, X.; Hou, P.; Zhou, E.; Guo, J.; Zhang, J.; Wang, D.; Guo, F.; Song, D.; Shi, X.; Zhang, L., Core-shell structured Li[(Ni0.8Co0.1Mn 0.1)0.7(Ni0.45Co0.1Mn 0.45)0.3]O2 cathode material for high-energy lithium ion batteries. *Journal of Alloys and Compounds* **2014,** *587*, 710-716; (c) Liu, W.; Hu, G.; Du, K.; Peng, Z.; Cao, Y., Enhanced storage property of LiNi0.8Co0.15Al0.05O2 coated with LiCoO2. *Journal of Power Sources* **2013,** *230* (0), 201-206; (d) Cho, Y.; Oh, P.; Cho, J., A new type of protective surface layer for high-capacity Ni-based cathode materials: nanoscaled surface pillaring layer. *Nano letters* **2013,** *13* (3), 1145-1152; (e) Yu, Z.; Chen, H.; Li, Z.; Yang, Z.; Song, H.; Gao, Y.; Zhang, Y.; Jin, Y.; Jiao, Z.; Gong, M.; Zhu, J.; Sun, X., Synthesis of ZnGa2O4 nanowires with [beta]-Ga2O3 templates and its photoluminescence performance. *Mater. Lett.* **2009,** *63* (1), 37-40.

41. (a) Haifeng, W.; Young-Il, J.; Biying, H.; Donald, R. S.; Yet-Ming, C., Electron microscopic characterization of electrochemically cycled LiCoO2 and Li(Al,Co)O2 battery cathodes. *Journal of Power Sources* **1999,** *81-82*; (b) Makimura, Y.; Zheng, S. J.; Ikuhara, Y.; Ukyo, Y., Microstructural Observation of LiNi0.8Co0.15Al0.05O2 after Charge and Discharge by Scanning Transmission Electron Microscopy. *Journal of the Electrochemical Society* **2012,** *159* (7), A1070-A1073.
42. Lee, S.; Jeong, M.; Cho, J., Optimized 4-V Spinel Cathode Material with High Energy Density for Li-Ion Cells Operating at 60 ℃. *Advanced Energy Materials* **2013,** *3* (12), 1623-1629.
43. (a) Lee, S.; Yoon, G.; Jeong, M.; Lee, M. J., Hierarchical Surface Atomic Structure of a Manganese-Based Spinel Cathode for Lithium-Ion Batteries. *Angewandte Chemie ...* **2015**; (b) Lee, M.-J.; Lee, S.; Oh, P.; Kim, Y.; Cho, J., High performance $LiMn_2O_4$ cathode materials grown with epitaxial layered nanostructure for Li-ion batteries. *Nano letters* **2014**.
44. Kim, H.; Kim, M. G.; Jeong, H. Y.; Nam, H.; Cho, J., A New Coating Method for Alleviating Surface Degradation of LiNi0.6Co0.2Mn0.2O2 Cathode Material: Nanoscale Surface Treatment of Primary Particles. *Nano Letters* **2015,** *15* (3), 2111-2119.
45. Jo, M.; Noh, M.; Oh, P.; Kim, Y.; Cho, J., A New High Power LiNi0.81Co0.1Al0.09O2 Cathode Material for Lithium-Ion Batteries. *Advanced Energy Materials* **2014,** *4* (13), n/a-n/a.

46. Sayle, T. X. T.; Catlow, C. R. A.; Sayle; Parker; Harding, Computer simulation of thin film heteroepitaxial ceramic interfaces using a near-coincidence-site lattice theory. *Philosophical Magazine A* **1993,** *68* (3), 565-573.

47. (a) Noguera, C., Polar oxide surfaces. *Journal of Physics: Condensed Matter* **2000,** *12* (31); (b) Goniakowski, J.; Finocchi, F.; Noguera, C., Polarity of oxide surfaces and nanostructures. *Reports on Progress in Physics* **2008,** *71* (1), 16501; (c) Pojani, A.; Finocchi, F.; Noguera, C., Polarity on the SrTiO 3 (111) and (110) surfaces. *Surface science* **1999,** *442* (2), 179-198; (d) Wagner, M. R.; Bartel, T. P.; Kirste, R.; Hoffmann, A.; Sann, J.; Lautenschläger, S.; Meyer, B. K.; Kisielowski, C., Influence of substrate surface polarity on homoepitaxial growth of ZnO layers by chemical vapor deposition. *Physical Review B* **2009,** *79* (3), 035307.

48. Steve, P., Fast Parallel Algorithms for Short-Range Molecular Dynamics. *Journal of Computational Physics* **1995,** *117*.

49. Craig, A. J. F.; Veluz, M. H. P.; Islam, M. S., Lithium Battery Materials Li M PO 4 (M = Mn, Fe, Co, and Ni): Insights into Defect Association, Transport Mechanisms, and Doping Behavior. *Chemistry of Materials* **2008,** *20*.

50. Hockney, R.; Eastwood, J., Computer simulation using particles. *CRC Press* **1988**.

51. Deskins, A.; Kerisit, S.; Rosso, K.; Dupuis, M., Molecular dynamics characterization of rutile-anatase interfaces. *The Journal of Physical Chemistry C* **2007,** *111* (26), 9290-9298.

52. Tucker, M. C.; Reimer, J. A.; Cairns, E. J.; Choi, S.; Manthiram, A., 7Li NMR Studies of Chemically-Delithiated Li1-xCoO2. *The Journal of Physical Chemistry B* **2002,** *106* (15), 3842-3847.

53. Maiyalagan, T.; Jarvis, K.; Therese, S.; Ferreira, P.; Manthiram, A., Spinel-type lithium cobalt oxide as a bifunctional electrocatalyst for the oxygen evolution and oxygen reduction reactions. *Nature communications* **2014,** *5*, 3949.

54. Gummow, R. J.; Thackeray, M. M., CHARACTERIZATION OF LT-LIXCO1-YNIYO2 ELECTRODES FOR RECHARGEABLE LITHIUM CELLS. *Journal of the Electrochemical Society* **1993,** *140*, 3365-3368.

55. (a) Jouanneau, S.; Eberman, K. W.; Krause, L. J.; Dahn, J. R., Synthesis, Characterization, and Electrochemical Behavior of Improved Li[Ni[sub x]Co[sub 1−2x]Mn[sub x]]O[sub 2] (0.1≤x≤0.5). *Journal of The Electrochemical Society* **2003,** *150*; (b) Thomas, M.; Simon, T.; Smith, A. J.; Deijun, X.; Dahn, J. R., A Guide to Li-Ion Coin-Cell Electrode Making for Academic Researchers. *Journal of The Electrochemical Society* **2011,** *158*.

56. (a) Guilmard, M.; Rougier, A.; Grune, A.; Croguennec, L.; Delmas, C., Effects of aluminum on the structural and electrochemical properties of LiNiO2. *Journal of Power Sources* **2003,** *115*, 305-314; (b) Chen, Y.; Wang, G.; Tian, J.; Konstantinov, K.; Liu, H., Preparation and properties of spherical LiNi< sub> 0.75</sub> Co< sub> 0.25</sub> O< sub> 2</sub> as a cathode for lithium-ion batteries. *Electrochimica acta* **2004**.

57. Lee, D.-J.; Scrosati, B.; Sun, Y.-K., Ni3(PO4)2-coated Li[Ni0.8Co0.15Al0.05]O2 lithium battery electrode with improved cycling performance at 55 ℃. *Journal of Power Sources* **2011,** *196* (18), 7742-7746.

58. Bandhauer, T. M.; Garimella, S.; Fuller, T. F., A critical review of thermal issues in lithium-ion batteries. *Journal of the Electrochemical Society* **2011,** *158* (3).

59. Xiong, X. H.; Wang, Z. X.; Yue, P.; Guo, H. J.; Wu, F. X.; Wang, J. X.; Li, X. H., Washing effects on electrochemical performance and storage characteristics of LiNi0.8Co0.1Mn0.1O2 as cathode material for lithium-ion batteries. *Journal of Power Sources* **2013,** *222*, 318-325.

60. Zhou, Y.-N.; Ma, J.; Hu, E.; Yu, X.; Gu, L.; Nam, K.-W.; Chen, L.; Wang, Z.; Yang, X.-Q., Tuning charge–discharge induced unit cell breathing in layer-structured cathode materials for lithium-ion batteries. *Nat Commun* **2014**.

61. (a) Amatucci, G. G.; Tarascon, J. M.; Larcher, D.; Klein, L. C., Synthesis of electrochemically active LiCoO2 and LiNiO2 at 100 degrees C. *Solid State Ionics* **1996,** *84* (3-4), 169-180; (b) Hameed, A. S.; Reddy, M. V.; Sarkar, N.; Chowdari, B. V. R., Synthesis and electrochemical investigation of novel phosphite based layered cathodes for Li-ion batteries. *RSC Advances* **2015**.

62. Garcia, B.; Farcy, J.; Pereira-Ramos, J. P.; Baffier, N., Electrochemical Properties of Low Temperature Crystallized LiCoO2. *Journal of The Electrochemical Society* **1997,** *144* (4), 1179-1184.

63. Lee, S.; Cho, Y.; Song, H. K.; Lee, K. T.; Cho, J., Carbon-coated single-crystal LiMn2O4 nanoparticle clusters as cathode material for high-energy and high-power lithium-ion batteries. *Angew Chem Int Ed Engl* **2012,** *51* (35), 8748-52.

64. (a) Myounggu, P.; Xiangchun, Z.; Myoungdo, C.; Gregory, B. L.; Ann Marie, S., A review of conduction phenomena in Li-ion batteries. *Journal of Power Sources* **2010,** *195*; (b) Wang, L.; Zhao, J.; He, X.; Gao, J.; Li, J.; Wan, C.; Jiang, C., Electrochemical impedance spectroscopy (eis) study of lini1/3co1/3mn1/3o2 for li-ion batteries. *Int. J. Electrochem. Sci* **2012,** *7* (1), 345-353; (c) Dees, D.; Gallagher, K.; Abraham, D.; Jansen, A., Electrochemical Modeling the Impedance of a Lithium-Ion Positive Electrode Single Particle. *Journal of The Electrochemical Society* **2013,** *160* (3).

65. Ko, Y.; Cho, Y.-G.; Song, H.-K., Programming galvanostatic rates for fast-charging lithium ion batteries: a graphite case. *RSC Advances* **2014,** *4* (32), 16545-16550.

66. Robertson, J., High dielectric constant gate oxides for metal oxide Si transistors. *Reports on Progress in Physics* **2006,** *69* (2), 327.

Ⅴ. Acknowledgement

유니스트에서 학위과정을 시작한지 6년이 지난 지금 길고도 험난했지만 포기하지 않고 달려왔던 석·박사 통합과정을 마치게 되었습니다. 학위과정을 무사히 마칠 수 있도록 많은 조언과 가르침을 주신 조재필 교수님 감사드립니다. 부족한 저를 지도하시느라 힘드셨겠지만 그런 저를 믿고 지지해 주셔서 정말 감사합니다. 일도 좋지만 건강도 챙기시고 가끔은 조금씩 쉬어가셨으면 합니다. 그리고 항상 하시는 일 모두 잘 되시길 바랍니다.

꾸밈없이 존재만으로도 빛이 나셨던 전기화학의 대가 고 박수문 교수님, 교수님의 수업을 들을 수 있어 정말 영광이었습니다. 교수님께 직접 시험 결과지를 받으며 잘했다 라는 말을 들었을 때, 길을 걸으며 힘내라는 조언해주셨을 때를 잊을 수 없습니다. 진심으로 존경합니다.. 그리고 많은 관심과 응원을 해주신 최남순 교수님, 교수님의 전해액 수업을 통해 많은 것을 배웠습니다. 어려운 결정학을 쉽게 이해할 수 있도록 지도해주신 이규태 교수님, 교수님 덕분에 XRD에 흥미가 생겼었습니다. 경험에서 우러나온 진심 어린 충고와 조언을 해주신 김영식 교수님 감사드립니다. 전극물질에 대해 다양한 관점에서 바라볼 수 있게 해주신 정윤석 교수님, 교수님의 수업은 저의 연구에 큰 도움이 되었습니다. 감사합니다.

처음 학위과정을 시작하였을 때, 연구 생활에 대해 많은 것을 알려주고 도와주셨던 든든한 용현오빠, 푸근한 민호오빠, 고기마니아 상한오빠, 보헤미안 민기오빠, 세심한 미희언니, 츤데레 호춘오빠 그리고 준호오빠, 선혜언니, 혜선언니 감사드립니다. 대학원 생활을 시작하면서 선배들과 나이차이로 어려워할 때 그리고 학위과정 내내 때로는 친구처럼 때로는 선배로써 많은 조언을 해준 미희언니 정말 고마워요~. 그리고 연구에 있어 어려움을 겪을 때 많은 고민상담을 해준 용현오빠 감사합니다. 이제는 삼성인이 되셨지만 연구를 하면서 힘든 일들을 함께 이겨내 온 미정언니, 정말 든든한 버팀목이었습니다. 앞으로도 힘내세요!! 이제 곧 포닥을 마치고 한국으로 돌아올 장수오빠, 오빠의 연구에 대한 열정은 정말 멋있어요. 취업 후에도 좋은 실적 내시리라 믿어요. 실험실의 비타민 같았던 기수오빠, 앞으로도 잘해내리라 믿어요. 본인이 해야 할 일과 본인의 장·단점을 잘 알고 있는 박민오빠, 앞으로도 지금처럼 좋은 연구실적 많이 내고 후배들 잘 챙겨주길 바래요. 항상 밝은 류군과 장인턴도 사수를 넘어 우수한 연구 열심히 하렴. 초창기 옆자리에 앉아 많은 이야기를 나누었던 규태, 이제는 실험실을 이끌어갈 선배님이 되었구나. 앞으로도 잘 해낼거라 믿어. 그리고 랩장하느라 고생많은 영욱이, 지금처럼 열심히 하면 좋은 성과 있을거야. 항상 자신있게! 부끄럼 많지만 속깊은 주혁이와 승준이, 이젠 멋진 선배가 되었구나. 학위과정 무사히 마친 해솔이, 앞으로 좋은일 만 있을거야.

이제 니켈 계를 이끌어갈 현이, 멘탈 강하게 잡고 포기 말고 항상 자신감 있게 헤쳐나가렴. 뭐든 열심히 하는 준혁이와 여장군 지은이, 착한 재성이. 다들 좋은 성과와 함께 보람 있는 학위과정을 보내길 바래. 너희 덕분에 즐겁게 마무리하는 시간을 보냈어.

다 언급할 수는 없지만 실험실 선/후배님들 감사했습니다. 다들 좋은 일들만 가득하길 빌어

요. 후배님들, 힘든 시간일지라도 견뎌내고 이겨내길 바래요. 응원할게~!

끝으로 길고 긴 학위 과정 동안 무한한 사랑과 응원을 보내준 우리 가족, 정말 감사합니다. 오랜시간 공부만 하느라 제대로 못한 효도 앞으로 다 할게요~! 그리고 언제나 믿고 지지해준 오라버니 정말 너무나 고맙고 감사해요. 덕분에 힘든 시간들 견뎌낼 수 있었습니다. 항상 행복합시다!!^^.